

---

**Towards next-generation molecular  
fingerprinting**  
**Advancing mid-infrared spectroscopy for biomedical  
applications**

Theresa Buberl

---



München 2021



---

**Towards next-generation molecular  
fingerprinting**  
**Advancing mid-infrared spectroscopy for biomedical  
applications**

**Theresa Buberl**

---

Dissertation  
der Fakultät für Physik  
der Ludwig-Maximilians-Universität  
München

vorgelegt von  
Theresa Buberl  
aus Würzburg

München, den 19.01.2021

Erstgutachter: Prof. Dr. Ferenc Krausz

Zweitgutachterin: Prof. Dr. Regina de Vivie-Riedle

Tag der mündlichen Prüfung: 03.03.2021

# Contents

<b>List of Figures</b>	<b>v</b>
<b>List of Tables</b>	<b>vii</b>
<b>List of Acronyms</b>	<b>ix</b>
<b>Abstract</b>	<b>xiii</b>
<b>Zusammenfassung</b>	<b>xv</b>
<b>1 Introduction</b>	<b>1</b>
<b>2 Theoretical background</b>	<b>7</b>
2.1 Nonlinear optical processes . . . . .	7
2.1.1 Sum and difference frequency generation . . . . .	8
2.1.2 Intensity dependent refractive index . . . . .	11
2.1.3 Electro-optic sampling . . . . .	12
<b>3 Electric-field-resolving spectrometer</b>	<b>17</b>
3.1 Ultrashort driving pulses in the near-infrared . . . . .	17
3.1.1 Kerr-lens modelocked Yb:YAG thin-disk oscillator . . . . .	18
3.1.2 Self-phase-modulation-based spectral broadening and pulse compression . . . . .	21
3.2 Phase-stable mid-infrared waveforms . . . . .	25
3.2.1 Intrapulse difference frequency generation . . . . .	25
3.2.2 Active intensity noise stabilization . . . . .	27
3.3 Field-resolved detection with electro-optic sampling . . . . .	30
3.3.1 Minimization of detection noise . . . . .	32
3.3.2 Optimization of detection efficiency . . . . .	33
3.3.3 Interferometric delay tracking . . . . .	36
3.4 Background-free measurement of molecular vibrations . . . . .	38
3.4.1 Elimination of water vapor background . . . . .	39
3.4.2 Temporal confinement of the exciting light pulses . . . . .	41
3.5 Benchmarking of the spectrometer . . . . .	44

---

3.5.1	Determination of the limit of detection . . . . .	44
3.6	Towards a rapid-scanning instrument . . . . .	49
3.6.1	Delay axis calibration in rapid scanning . . . . .	51
3.6.2	First experimental rapid scanning traces in the mid infrared . . . . .	54
<b>4</b>	<b>Broadband interferometric subtraction of optical fields</b>	<b>61</b>
4.1	Advantages of differential spectroscopy . . . . .	61
4.2	Sensitivity improvement due to optical subtraction . . . . .	63
4.2.1	Differential vs. direct measurements in frequency-domain spectroscopy	63
4.2.2	Differential vs. direct measurements in field-resolved, time-domain spectroscopy . . . . .	66
4.3	Mach-Zehnder-type deep nulling interferometer . . . . .	72
4.3.1	Achromatic phase shift of $\pi$ . . . . .	72
4.3.2	Theoretical limitation of the extinction ratio . . . . .	75
4.3.3	Broadband optical subtraction in the near-infrared . . . . .	77
4.3.4	Broadband optical subtraction in the mid-infrared . . . . .	82
4.3.5	Dual-compartment liquid cuvette . . . . .	83
<b>5</b>	<b>Energy transfer between molecules and electric fields on a sub-cycle time scale</b>	<b>85</b>
5.1	Coherent emission of excited molecules . . . . .	85
5.1.1	Ab-initio simulation of the refractive index . . . . .	87
5.1.2	Energy balance formalism . . . . .	89
5.1.3	Ratio of absorbed and re-emitted energy . . . . .	91
5.2	Experimental energy balance of vibrationally excited DMSO <sub>2</sub> molecules . . . . .	94
5.2.1	Quasi-impulsive excitation . . . . .	94
5.2.2	Chirped excitation . . . . .	98
<b>6</b>	<b>Summary and outlook</b>	<b>103</b>
<b>A</b>	<b>Data archiving</b>	<b>107</b>
	<b>Acknowledgement</b>	<b>121</b>

# List of Figures

2.1	Photon energy diagram of the second order nonlinearities . . . . .	9
2.2	Evolution of sum frequency intensity inside a nonlinear crystal . . . . .	10
2.3	Self-phase modulation for a Gaussian and a super-Gaussian pulse . . . . .	11
2.4	Electro-optic sampling geometry . . . . .	13
3.1	Sketch of the oscillator and the extra-cavity broadening setup . . . . .	18
3.2	Intensity autocorrelation and spectrum of the modelocked oscillator . . . . .	20
3.3	Spot pattern on the Herriott cell mirrors . . . . .	22
3.4	Characterization of nonlinear broadening and pulse compression . . . . .	23
3.5	Parameters of intrapulse difference frequency generation . . . . .	26
3.6	Relative intensity noise and active suppression . . . . .	28
3.7	Characterization of the mid infrared stability . . . . .	29
3.8	Sketch of mid infrared generation and electro-optic sampling detection . . . . .	31
3.9	Shot-noise dominated electro-optic sampling detection . . . . .	33
3.10	Electro-optic sampling parameters . . . . .	34
3.11	Electro-optic sampling traces and spectra . . . . .	35
3.12	Sketch of the interferometric delay tracking setup . . . . .	37
3.13	Isolation of turbopump vibrations . . . . .	39
3.14	Pressure dependent molecular background . . . . .	40
3.15	Spectral phase and group delay of mid infrared waveforms . . . . .	42
3.16	Compression of the mid infrared waveform and its exponential roll-off . . . . .	43
3.17	Field resolved measurements of DMSO <sub>2</sub> solved in water . . . . .	45
3.18	Measurement settings for benchmarking with DMSO <sub>2</sub> . . . . .	46
3.19	Evaluation of limit of detection for DMSO <sub>2</sub> solved in water . . . . .	48
3.20	Timing noise of Yb:YAG and Er:fiber oscillator . . . . .	52
3.21	Sketch of electro-optic delay tracking for dual oscillator scan . . . . .	53
3.22	Sketch of rapid scanning with a sonotrode . . . . .	54
3.23	EOS measurements with sonotrode . . . . .	55
3.24	Comparison of fast and slow differential referencing . . . . .	56
3.25	Schematic layout of the dual oscillator rapid scan . . . . .	57
3.26	EOS measurements with dual oscillator fast scan . . . . .	59
4.1	Illustration of direct and differential configuration . . . . .	63

---

4.2	Comparison of the limit of detection in the direct and the differential case .	65
4.3	Simulation of electric-field-resolved direct and differential measurement . .	68
4.4	Simulation of electric-field-resolved direct and differential signal-to-noise ratio	70
4.5	Broadband interferometric subtraction in a Mach-Zehnder-type interferometer	73
4.6	Broadband interferometric subtraction for isolation of nonlinear response .	74
4.7	Influence of substrate thickness mismatch on the extinction ratio . . . . .	75
4.8	Influence of alignment sensitivity on the extinction ratio . . . . .	76
4.9	Laser source characterization and interferometric setup . . . . .	78
4.10	Characterization of the extinction ratio in the near-infrared . . . . .	79
4.11	Frequency-resolved extinction ratio in the near-infrared . . . . .	80
4.12	Spatially isolated methane resonance features . . . . .	81
4.13	Broadband optical subtraction in the mid-infrared . . . . .	82
4.14	Dual compartment liquid cuvette for optical subtraction in the mid-infrared	84
5.1	Energy relaxation channels of vibrationally excited molecules in a liquid . .	86
5.2	Real and imaginary part of the refractive index of DMSO <sub>2</sub> from ab-initio model . . . . .	88
5.3	Connection between time-resolved energy balance and frequency-resolved measurement . . . . .	90
5.4	Comparison $\delta$ -pulse and a quasi-impulsive excitation . . . . .	93
5.5	Energy balance of DMSO <sub>2</sub> upon quasi-impulsive excitation . . . . .	95
5.6	Measured and calculated absorption of DMSO <sub>2</sub> . . . . .	97
5.7	Dispersive excitation of DMSO <sub>2</sub> molecules . . . . .	99
5.8	Energy balance of DMSO <sub>2</sub> upon dispersive excitation . . . . .	100
5.9	Comparison of quasi-impulsive and dispersive excitation . . . . .	101

# List of Tables

- 5.1 Measured and calculated parameters for the two major resonances of DMSO<sub>2</sub> 97



# List of Acronyms

AOI	angle of incidence
AOM	acousto-optic modulator
AOPDF	acousto-optic programmable dispersive filter
AR	anti-reflection
ASOPS	asynchronous optical sampling
BOM-PD	balanced optical-to-microwave phase detection
CEO	carrier-envelope offset
CW	continuous wave
DFG	difference frequency generation
ECOPS	electronically controlled optical sampling
EFL	effective focal length
EODT	electro-optic delay tracking
EOS	electro-optic sampling
FROG	frequency-resolved optical gating
FRS	field-resolved spectroscopy
FS	fused silica
FTIR	Fourier-transform infrared
FTL	Fourier transform limit
FWHM	full width at half maximum
GDD	group delay dispersion
HR	highly reflective
HWP	half waveplate
IDT	interferometric delay tracking
IR	infrared

KLM	Kerr-lens modelocking
LPF	long pass filter
MCT	mercury cadmium telluride
MIR	mid infrared
MPC	multi-pass cell
NIR	near infrared
OPA	optical parametric amplification
OSA	optical spectrum analyzer
PCF	photonic-crystal fiber
PD	photo diode
PZT	piezoelectric transducer
QWP	quarter waveplate
RIN	relative intensity noise
ROC	radius of curvature
SFG	sum frequency generation
SHG	second-harmonic generation
SNR	signal-to-noise ratio
SPM	self-phase modulation
TOD	third order dispersion
WP	Wollaston prism

# List of Publications

## Journal publications:

- A. Weigel, P. Jacob, D. Gröters, **T. Buberl**, M. Huber, J. Heberle, M. Trubetskov, and I. Pupeza, "*Ultra-rapid electro-optic sampling of octave-spanning mid-infrared waveforms.*", submitted.
- M. Peschel, M. Högner, **T. Buberl**, R. de Vivie-Riedle, and I. Pupeza, "*Sub-optical-cycle light-matter energy transfer in molecular vibrational spectroscopy.*", in preparation.
- **T. Buberl**, P. Sulzer, F. Krausz, and I. Pupeza, "*Broadband interferometric subtraction of optical fields.*", **Optics express** 27 (3), 2432–2443, (2019).

## Patent applications:

- A. Weigel, **T. Buberl**, F. Krausz, I. Pupeza, "*Method and apparatus for measuring a time delay between pairs of pulses from laser pulse sequences, and applications thereof*", Patent Application No. PCT/EP2020/087657, (2020).
- I. Pupeza, F. Krausz, **T. Buberl**, "*Interferometry with an achromatic interferometric superposition of electromagnetic fields*", Patent Application No. PCT/EP2018/069229, (2018).

## Conference contributions:

- **T. Buberl**, M. Peschel, M. Högner, R. de Vivie-Riedle, and I. Pupeza, "*Sub-optical-cycle light-matter energy transfer dynamics in molecular vibrational spectroscopy.*", Conference on Lasers and Electro-Optics Europe & European Quantum Electronics Conference, Munich (Germany), 2021, submitted.
- **T. Buberl**, P. Sulzer, F. Krausz, I. Pupeza, "*Achromatic interferometric subtraction of optical fields.*", Conference on Lasers and Electro-Optics Europe & European Quantum Electronics Conference, Munich (Germany), 2019.
- **T. Buberl**, P. Sulzer, F. Krausz, I. Pupeza, "*Broadband interferometric subtraction of ultrashort pulses.*", Conference on Ultrafast Optics, Bol (Croatia), 2019.



# Abstract

The unique molecular fingerprint of human biofluids, recorded in vibrational spectroscopy, carries rich information on the health status of a person. Abnormalities in the molecular composition thus induce specific changes in this molecular fingerprint which can indicate the presence of several diseases. The ability to detect these abnormalities in a fast, reliable, and marker-free manner renders vibrational spectroscopy a potential candidate for liquid biopsy. However, it remains a question of ongoing research whether the linear molecular response of vibrational fingerprinting carries sufficient information for disease-specific diagnosis.

Thanks to recent progress in laser technology, new types of vibrational spectrometers have emerged pushing the limits of linear spectroscopy. Laser-based mid-infrared (MIR) sources offer higher brightness than the most commonly used thermal emitters, as well as nonlinear, time-gated detection schemes avoiding the use of noisy infrared detectors.

The present thesis describes the design, construction, optimization, and application of an electric-field-resolving MIR spectrometer and introduces two concepts to further boost its performance towards higher sensitivity, dynamic range, and throughput. The developed spectrometer is based on the nonlinear down-conversion of the output of a high peak and average power Yb:YAG thin-disk oscillator, generating broadband, phase-stable MIR pulses whose radiation is temporally confined to a few cycles of the optical field. The 28-MHz-repetition-rate MIR pulses cover a spectral range from 5  $\mu\text{m}$  to 12  $\mu\text{m}$  with an average power of 52 mW. Electro-optic sampling (EOS) facilitates the time-resolved detection of the electric field of the generated MIR pulses after interaction with vibrationally active molecules. Temporal separation of the molecular response from the short MIR excitation pulses renders detection sensitivity robust against technical noise and enables gate-pulse-shot-noise-dominated detection of the pure resonant molecular response. At an operating pressure of  $10^{-3}$  mbar, the completely background-free molecular response can be recorded starting 600 fs after the peak of the excitation pulse with a dynamic range of  $5 \times 10^5$  in electric field.

Low-frequency source intensity fluctuations, which are present in the molecular background following the few-cycle excitation, can obscure weak molecular signals of important constituents restricting the applicability of the instrument to liquid biopsy. To address these shortcomings, two different strategies were investigated in this thesis.

Firstly, two different concepts to replace the rather slow mechanical delay stage required

for EOS detection by rapid scanning were implemented. The rapidly oscillating surface of a sonotrode can be utilized to modulate the path length of the EOS sampling pulse and introduce a geometric delay. A more flexible approach is to generate the EOS sampling pulse by a second modelocked laser oscillator with a detuned and periodically modulated repetition rate. Rapidly scanning spectrometers promise the acquisition of full EOS scans at multi-kHz rates which is faster than the dominant contributions of technical noise. Therefore, technical noise remains 'frozen' within single waveform scans. While the final implementation of these techniques in the instrument is ongoing, the preliminary results presented here show that both techniques are highly promising.

Secondly, the concept of achromatic, interferometric subtraction of the fingerprints of two samples generated by copies of the same MIR excitation pulse was investigated. Placing a sample in one arm and a reference in the other arm of an achromatic interferometer yields the isolated difference signal between the two in the destructive port of the interferometer. In the difference signal, common intensity fluctuations are suppressed and the requirements to the (linear) detection dynamic range are relaxed. A novel concept for an achromatic, Mach-Zehnder-type interferometer, relying on the combination of Fresnel reflections off the first and second surface of a beam splitter and beam combiner, respectively, was designed, constructed, and evaluated in the near and mid-infrared spectral ranges. In the near-infrared, an extinction ratio of  $6 \times 10^{-4}$  was achieved for a super-octave spectrum enabling a proof of principle of differential molecular fingerprinting with methane. In the MIR, the extinction ratio was limited to  $4 \times 10^{-3}$  due to the poorer quality of available transmissive substrates. The combination of interferometric subtraction and EOS detection was studied with a numerical model and is the subject of further experimental investigations.

Finally, the spectrometer developed in the frame of this thesis enabled the first time-domain study of the energy transfer between a broadband MIR excitation field and resonant molecules, with sub-optical-cycle temporal resolution. In the regime of quasi-impulsive excitation, the time-resolved energy balance reveals the total amount of energy which is first absorbed and then coherently re-emitted by the molecules. For a chirped excitation pulse, coherent transients consisting of a sequence of absorption and stimulated emission are observed. These temporal sequences of absorption and emission in the different regimes remain hidden to time-integrating frequency-domain spectroscopies. Collaborative efforts with theorists proved that quantum-chemistry ab-initio modelling including the counter-rotating terms of the electric field reproduces our experimental observations well and explains the sub-cycle dynamics.

The evaluation of the novel technical approaches presented in this thesis together with the findings on the energy transfer study lay the foundations for advanced field-resolved spectroscopy. This new generation of field resolved spectrometers will benefit the further investigation of broadband vibrational spectroscopy as tool for medical diagnosis.

# Zusammenfassung

Der einzigartige molekulare Fingerabdruck, der mittels Vibrationsspektroskopie von menschlichen Bioflüssigkeiten gemessen wird, enthält viele Informationen über den Gesundheitszustand einer Person. Anomalien in der molekularen Zusammensetzung rufen spezifische Veränderungen dieses molekularen Fingerabdrucks hervor, die auf das Vorhandensein verschiedener Krankheiten hinweisen können. Vibrationsspektroskopie erlaubt es, diese Anomalien schnell, verlässlich und markerfrei zu detektieren und ist daher ein möglicher Kandidat für Flüssigbiopsie. Ob die lineare Antwort der Moleküle, die in der Vibrationsspektroskopie gemessen wird, ausreichende Informationen für krankheitsspezifische Diagnosen liefert, bleibt eine offene Forschungsfrage. Dank jüngster Fortschritte im Bereich der Lasertechnologie entstanden neuartige Vibrationsspektrometer, um die Möglichkeiten der Linearspektroskopie auszureizen. Laserbasierte Strahlungsquellen im mittleren Infraroten (MIR) ermöglichen größere Leuchtdichten als herkömmliche thermische Strahlungsquellen, sowie nichtlineare, zeitlich filternde Detektionsmethoden, die rauschintensive Infrarotdetektoren vermeiden.

Die vorliegende Dissertation beschreibt die Konstruktion, Optimierung und Anwendung eines Spektrometers, welches das elektrische Feld von MIR Strahlung zeitlich auflöst. Zwei Ansätze zur Steigerung der Sensitivität, des Dynamikbereichs und der Durchsatzleistung werden vorgestellt. Das entwickelte Spektrometer basiert auf der nichtlinearen Abwärtskonvertierung eines Yb:YAG Dünnscheibenoszillators mit hoher Spitzen- und Durchschnittsleistung. Dadurch werden breitbandige, phasenstabile MIR Pulse erzeugt, deren zeitliche Dauer auf wenige Oszillationen des optischen Feldes beschränkt ist. Die MIR-Pulse mit einer Repetitionsrate von 28 MHz decken den Spektralbereich von 5  $\mu\text{m}$  bis 12  $\mu\text{m}$  mit einer Durchschnittsleistung von 52 mW ab. Elektrooptisches Abtasten (EOS) des erzeugten MIR Pulses nach Interaktion mit vibronisch aktiven Molekülen ermöglicht die zeitaufgelöste Detektion des resultierenden elektrischen Feldes. Durch zeitliches Filtern des kurzen Anregungspulses ist diese Methode größtenteils unempfindlich gegenüber technischem Rauschen und ermöglicht das schrotrauschenlimitierte Messen der hintergrundfreien Molekülantwort. Bei einem Druck von  $10^{-3}$  mbar kann diese 600 fs nach dem Maximum des Anregungspulses mit einem Dynamikbereich von  $5.5 \times 10^5$  im elektrischen Feld gemessen werden.

Durch niederfrequentes Intensitätsrauschen der Laserquelle, das sich auf das molekulare Hintergrundsignal überträgt, können schwache Signale wichtiger Probenbestandteile überdeckt werden. Um dieses Defizit in der diagnostischen Anwendung zu überwinden, wurden im Rahmen dieser Dissertation zwei verschiedene Strategien untersucht.

Zum einen wurde der geschwindigkeitslimitierte mechanische Verzögerungstisch, der für die EOS-Detektion notwendig ist, durch zwei verschiedene Konzepte zum schnellen Abtasten ersetzt. Die oszillierende Oberfläche einer Sonotrode kann verwendet werden um die Weglänge des EOS-Abtastpulses zu modulieren und eine geometrische Verzögerung zu erzeugen. In einem flexibleren Ansatz wird der Abtastpuls von einem zweiten modengekoppelten Oszillator generiert, dessen Repetitionsrate gegenüber dem Yb:YAG Oszillator periodisch verstimmt wird. Schnelles Abtasten macht das Aufnehmen eines vollständigen EOS-Scans in weniger als einer Millisekunde möglich. Dadurch werden einzelne Scans nahezu unempfindlich gegenüber technischem Rauschen, welches vor allem bis in den niederen kHz-Bereich dominiert. Obwohl die endgültige Umsetzung beider Konzepte noch aussteht, zeigen die vorläufigen Ergebnisse, dass beide Konzepte sehr vielversprechend sind.

Zum anderen wurde die Idee der interferometrischen Subtraktion von Fingerabdrücken zweier Proben, die von Kopien eines einzigen Anregungspulses erzeugt wurden, untersucht. Wenn man eine Probe in einem Arm und eine Referenz im anderen Arm eines achromatischen Interferometers platziert, erhält man das isolierte Differenzsignal von beiden im destruktiven Ausgang des Interferometers. Im Differenzsignal werden gemeinsame Intensitätsfluktuationen unterdrückt und die Anforderungen an den (linearen) Dynamikbereich der Detektion reduziert. Dafür wurde ein achromatisches, Mach-Zehnder-ähnliches Interferometer, das auf der Kombination von Fresnel-Reflektionen von der ersten und zweiten Oberfläche eines Strahlteilers bzw. Strahlkombinierers beruht, entworfen, aufgebaut und charakterisiert. Im nahen Infraroten wurde ein Auslöschungsverhältnis von  $6 \times 10^{-4}$  innerhalb des Spektralbereichs von 900 nm und 2100 nm erreicht, was einen Machbarkeitsnachweis für differenzielle Fingerabdruckspektroskopie mit Methan erlaubte. Im MIR war das Auslöschungsverhältnis durch die minderwertige Qualität der transmissiven Substrate auf  $4 \times 10^{-3}$  beschränkt. Die Kombination von interferometrischer Subtraktion und EOS-Detektion wurde mit einem numerischen Modell analysiert und wird in weiteren Experimenten untersucht werden.

Abschließend konnte mittels des entwickelten Spektrometers eine Studie zum Energietransfer zwischen einem breitbandigen MIR Anregungsfeld und resonanten Molekülen durchgeführt werden. Im Regime der impulsiven Anregung ergibt die zeitaufgelöste Energiebilanz den Gesamtanteil der Energie, die zuerst von den Molekülen absorbiert und danach kohärent reemittiert wird. Für einen gechirpten Anregungspuls wurden kohärente Transienten beobachtet, die eine Folge von Absorption und stimulierter Emission darstellen. Diese zeitlichen Abfolgen von Absorption und Emission in den verschiedenen Regimen sind für frequenz aufgelöste Messmethoden nicht zugänglich. In Zusammenarbeit mit dem Lehrstuhl für theoretische Femtosekundenchemie wurde gezeigt, dass man mit einem ab-initio Quantenchemiemodell die experimentellen Ergebnisse reproduzieren und insbesondere durch Einbeziehen der kontrarotierenden Komponenten des elektrischen Feldes die beobachtete Subzyklusdynamik erklären kann.

Die Auswertung der technologischen Neuerungen zusammen mit den Erkenntnissen der Energietransferstudie schaffen die Voraussetzungen für ein optimiertes feldaufgelöstes Spektrometer. Diese neue Generation von feldaufgelösten Spektrometern wird der weiteren Erforschung von Vibrationsspektroskopie als medizinische Diagnostik zugutekommen.

# Chapter 1

## Introduction

What drives science is the curiosity to understand the world we are living in, ranging from a microscopic level to the whole universe. What drives me is to utilize the curiosity-driven findings on the fundamental correlations of our world to the best of human kind, and connect basic science to applications relevant for our society. Both basic science and application crucially depend on technological development facilitating ever more precise insight into the world and opening new routes for applications. This thesis combines all three aspects, and describes the development of a novel spectroscopic instrument motivated by its benefit to medical diagnoses and presents deeper insight into molecular energy transfer dynamics enabled by this instrument.

### Vibrational spectroscopy for disease diagnosis

Pre-symptomatic disease diagnosis is highly desirable to detect physiological disorders like cancer in an early state and increases the success rates in therapy. A cost-effective diagnostic tool based on non-invasive specimens could enable a vast screening of the population and decrease the mortality and morbidity caused by the disease. The exact molecular composition of diagnostic liquids like human blood or urine mirrors the health state of a person, and incremental changes thereof can indicate the presence of a disease [1]. Disease-specific molecular markers can be identified and quantitatively determined in complex biofluids with mass spectroscopy [2, 3] or an antibody microarray [4] to distinguish between the samples of healthy and diseased individuals. When based on a single marker-molecule however, these methods cannot provide a satisfying level of specificity and sensitivity for clinical applications [5].

In contrast to marker-based approaches, vibrational spectroscopy captures information on the *global* biomolecular composition of the diagnostic liquid in a single measurement and is therefore a promising candidate for liquid biopsy [1]. Nearly all biomolecules like proteins, amino acids, and lipids are vibrationally active in the infrared (IR) spectral region between 2  $\mu\text{m}$  and 20  $\mu\text{m}$  which makes vibrational spectroscopy a powerful tool to investigate complex compositions of biomolecules in a fast, reliable, and marker-free

manner [6]. Each interrogated molecule exhibits a set of specific vibrational resonances depending on the polarity, the masses, and the inter- and intramolecular environment of the chemical bonds within the molecule [7]. Due to the vast occurrence of similar or identical chemical bonds and molecular substructures within different biomolecules their detected vibrational resonances tend to overlap hindering the identification and quantification of single macromolecules within a complex composition of molecules. However, the recorded vibrational spectra provide a unique *molecular fingerprint* of the investigated specimen which resembles its exact molecular composition and is sensitive to miniscule changes thereof [8].

The most established and reliable technique to measure molecular fingerprints is Fourier-transform infrared (FTIR) spectroscopy. Molecular fingerprints of blood specimen recorded with an FTIR spectrometer were successfully applied to detect bladder cancer, ovarian cancer, and brain tumors [9, 10, 11]. Despite these successful demonstrations and the undeniable potential of the method, vibrational spectroscopy is still far away from being a routine examination in clinical diagnostics. To promote liquid biopsy based on vibrational spectroscopy large, standardized databases of molecular fingerprints from diseased and healthy individuals, as well as technological advances in detecting incremental changes in molecular fingerprints are necessary [9].

These challenges are currently tackled in an interdisciplinary team of scientists at the Max-Planck Institute for Quantum Optics and the Chair for Experimental Physics - Laser Physics at the Ludwig Maximilians University Munich and set the framework for this thesis. The presented development of novel technological concepts for a laser-based, electric-field-resolved spectrometer were motivated by the diagnostic demand to increase the sensitivity of vibrational spectroscopy.

## State-of-the-art spectroscopies and their limitations

Since the first demonstration of an FTIR spectrometer based on computational fast Fourier transformation in 1956 [12] this technology was commercialized and optimized over decades to become the gold standard of vibrational spectroscopy. In comparison to dispersive spectrometers, the interferograms recorded with FTIR spectrometers benefit from the multiplex and the throughput advantage [13]. The multiplex advantage describes the ability of an FTIR spectrometer to record information from all spectral elements simultaneously, resulting in a reduced measurement time for identical signal-to-noise ratio (SNR) [14]. The throughput advantage refers to the increase in irradiance on the detector as compared to a dispersive instrument with identical spectral resolution [15]. This is particularly crucial since most commercial FTIR spectrometers employ spatially and temporally incoherent thermal emitters to generate broadband IR radiation. Despite their Watt-level average powers, thermal emitters suffer from low brightness due to the lack of spatial coherence. Besides the low brightness of the radiation source, the inferior noise performance of detectors available for the IR spectral region [13] currently limits the sensitivity of FTIR spectroscopy.

---

Large-scale facilities like synchrotrons [16] and free electron lasers [17] can provide a broadband source of IR radiation with high brightness to increase the sensitivity of FTIR spectroscopy. However, large-scale facilities are no viable solution for day-to-day measurements.

Due to their unparalleled coherence properties combined with their small footprint, lasers provide an interesting alternative to large-scale facilities. However, the development of laser-based table-top sources of broadband radiation in the molecular fingerprint region between 2  $\mu\text{m}$  and 20  $\mu\text{m}$  was retarded due to the lack of laser gain media directly emitting in this spectral range.

This shortcoming was mitigated by the advent of the quantum cascade laser (QCL) in 1994 which allowed for flexible engineering of the laser emission wavelength [18]. In a QCL, well-established semiconductor materials are utilized to manufacture multiple-quantum-well structures acting as laser gain media. The resulting quantum confinement defines the laser emission frequency and can be designed according to the needs of the application [19]. Nowadays, compact, high-brightness MIR sources tunable over more than one spectral octave can be realized by combining up to four single QCLs [20]. This possibility enabled the application of QCL-based MIR spectrometers to several sensing measurements in human biofluids [21, 22, 20].

Another path towards powerful, laser-based MIR sources opened up due to the availability of high average and high peak power femtosecond-oscillators at 1  $\mu\text{m}$  [23] providing the basis for nonlinear frequency down-conversion to the MIR [24]. With the advent of new gain materials, the emission wavelength of Watt-level oscillators was pushed beyond 2  $\mu\text{m}$  [25, 26, 27] further enhancing the efficiency of nonlinear frequency conversion. Today, table-top sources of high power femtosecond-oscillators can outperform the brilliance of a synchrotron across the entire molecular fingerprint region [28].

Enabled by this technological progress, our research group developed a conceptually different approach for vibrational spectroscopy aiming at exploiting the high brightness and temporal coherence of lasers to increase sensitivity. In this approach, the 1- $\mu\text{m}$ -output pulses of a Yb:YAG thin disk oscillator are further temporally compressed and frequency-upconverted in a nonlinear crystal to yield broadband, waveform-stable mid infrared (MIR) pulses temporally confined to less than 100 fs [24]. After interaction of the MIR pulses with vibrationally active molecules inside a liquid cuvette, the emerging MIR electric field is detected via electro-optic sampling (EOS) [29, 30]. This process can be understood in a two-step picture: A delayed copy of the near infrared (NIR) driving pulse co-propagates with the MIR pulse in the nonlinear detection crystal where their sum-frequency is generated. The interference of the NIR sampling pulse with the orthogonally polarized sum-frequency wave results in a modified polarization state in the frequency range of their spectral overlap. An ellipsometer detects the polarization modulation as a function of the mutual delay between MIR and sampling pulse which yields a signal linearly proportional to the amplitude and sign of the electric field of the MIR radiation [31].

The field-resolving nature of this technique implies a few fundamental differences compared to conventional FTIR spectrometers. The measured quantity directly reveals the complete amplitude and phase information of the sampled radiation. Due to the scaling of

the signal with the amplitude of the electric field instead of the intensity, the optimum sample thickness defined by the absorption of the surrounding matrix substance (mostly liquid water for biofluids) can be twice as thick as in detector-noise-limited FTIR spectroscopy [32].

Detection with EOS mitigates the need for noisy MIR detectors because the detection happens in the NIR spectral region, where detectors with lower noise equivalent power are available [13]. The nonlinear upconversion process involved in EOS detection also provides another advantage: For every delay step, the NIR pulse gates the MIR wave such that only the intensity noise of the MIR wave within the brief temporal overlap of both is transferred to the EOS signal. Together with the temporal confinement of the MIR excitation pulse to less than 100 fs and the temporal resolution of the method, this enables the observation of the free induction decay of vibrationally excited molecules with decay times in the picosecond range [33] in a quasi-background-free manner [34]. Temporal separation of the resonant molecular response from the short excitation pulse renders the SNR of field-resolved spectroscopy (FRS) gate pulse shot-noise-limited and robust against technical source noise [35].

This conceptual difference of FRS to time-integrating vibrational spectroscopies accomplishes to turn the higher brightness of laser-based MIR sources into a higher SNR for MIR spectrometers. Previously, the SNR of laser-based spectrometers was limited by their increased technical source noise as compared to thermal emitters. An experimental comparison of a commercial, state-of-the-art FTIR spectrometer with the novel FRS instrument proved the higher sensitivity of the FRS instrument by measuring a 40 times lower limit of detection for DMSO<sub>2</sub> solved in water than with the conventional FTIR instrument [36].

Currently, the sensitivity to small changes in the molecular composition of a biofluid is limited by the intensity noise carried by the global molecular fingerprint. In addition, the comparability of molecular fingerprints measured over the time period of several months or years is particularly challenging. To provide a source-independent molecular fingerprint of a biofluidic sample spectroscopic referencing is required. At the moment, the rather long time of a few minutes to sequentially record sample and reference measurement leads to distortions in the molecular fingerprints. In close collaboration with medical facilities, a part of our team focuses on the further development of the novel FRS technology to overcome these limitations and satisfy the high demands of biofluid-based disease diagnosis.

## Outline of the thesis

This thesis describes the construction of an FRS instrument and presents two concepts to further improve its performance by implementing rapid scanning and interferometric reference subtraction. In addition, the technological advances are harnessed to investigate the temporally resolved energy transfer between a broadband excitation field and vibrationally excited molecules. The content of the thesis is structured as follows:

To provide a theoretical framework for the construction of the FRS instrument, the

---

major underlying nonlinear optical effects are explained in the second chapter. Included are: sum and difference frequency generation, self-focusing and self-phase modulation, as well as electro-optic sampling.

The third chapter is dedicated to the design, construction and characterization of the FRS instrument. All-solid-state spectral broadening in a two-stage multipass cell and subsequent compression driven by a Yb:YAG thin-disk oscillator serves as a high peak and average power source of sub 20 fs-pulses centered at 1  $\mu\text{m}$ . Via intrapulse difference frequency generation (IPDFG) the pulses are converted into broadband, phase-stable MIR waveforms. Their electric field is detected with gate pulse shot-noise-dominated EOS aided by interferometric delay tracking. Customized dispersive mirrors are utilized to compress the MIR pulses and the molecular background due to water vapor molecules is eliminated by operating the system in vacuum. In a benchmarking experiment, the new FRS instrument is compared to the first-generation FRS instrument within our group and to a commercial, research-grade FTIR spectrometer. Finally, different options for a rapid-scanning FRS instrument are discussed and first experimental results based on a sonotrode and a second detuned oscillator, respectively, are presented.

In the fourth chapter, an achromatic interferometer is introduced which enables the optical subtraction of laser pulses with superoctave spectral coverage. The interferometer allows to experimentally isolate small optical differences between the response of a reference and a sample substance. The concept is first demonstrated with NIR pulses and then transferred to the MIR spectral range. A discussion based on simulations identifies different regimes of noise contributions for which the application of the interferometric method is beneficial.

The spectroscopic application of the developed FRS instrument described in the fifth chapter provides insight into the time-resolved energy exchange between resonant molecules and exciting electric fields on a sub-cycle time scale. The sequence of absorption and coherent emission of radiation by  $\text{DMSO}_2$  molecules solved in water upon excitation with a temporally compressed and a chirped MIR pulse is studied. All experimental results are compared to calculations based on an ab-initio quantum chemistry model developed by our collaborators.

Finally, the sixth chapter summarizes the results and their implications for FRS. Based on rapid scanning, an advanced FRS instrument is proposed which mitigates the problem of long-term comparability and intensity noise of the global molecular fingerprint.



# Chapter 2

## Theoretical background

The interconnecting physical phenomenon in this thesis is the interaction between the electro-magnetic radiation emitted by lasers and matter. In the first part of the thesis, *nonlinear interactions* of intense laser pulses and matter are utilized to create a unique spectroscopic instrument, whereas in the second part the *linear interaction* between the electric field and resonant molecules is investigated with this spectrometer. This chapter provides the theoretical framework for the nonlinear interactions and the resulting nonlinear optical effects.

### 2.1 Nonlinear optical processes

When light interacts with matter its oscillating electric field  $E(t)$  affects the motion of the bound electrons inside the material and introduces oscillating dipoles. The oscillating dipoles themselves start to emit radiation. If the intensity of the electric field is moderate the displacement of the electrons from their equilibrium position is small and the system can be described as a driven harmonic oscillator, i.e. the potential well seen by the electrons can be approximated by a parabola. In this regime, the strength of the dipole moment per unit volume or polarization  $P(t)$  of the material is proportional to the electric field [37]:

$$P(t) = \epsilon_0 \chi^{(1)} E(t), \quad (2.1)$$

where  $\epsilon_0$  is the permittivity of free space and  $\chi^{(1)}$  is the linear susceptibility. However, for high optical intensities as commonly generated by lasers, the displacement of the electrons from their equilibrium position is so large that the harmonic approximation is no longer an adequate description. To account for the actual anharmonic potential well seen by electrons inside a material Eqn.((2.1)) can be generalized by expanding the polarization  $P(t)$  in a Taylor series of the electric field  $E(t)$  [37]:

$$P(t) = \epsilon_0 [\chi^{(1)} E(t) + \chi^{(2)} E(t)^2 + \chi^{(3)} E(t)^3 + \dots], \quad (2.2)$$

where  $\chi^{(2)}$  and  $\chi^{(3)}$  etc. denote the second, third, and higher order nonlinear susceptibilities. For the remainder of this thesis, the higher order terms of the expansion in

Eqn.(2.2) are not relevant. In general, the susceptibility  $\chi^{(n)}$  is a frequency dependent tensor of order  $n + 1$  but will in the following be treated like a scalar for simplicity. For common dielectrics the nonlinear susceptibility is orders of magnitude smaller than the linear susceptibility ( $\chi^{(1)} \simeq 1$  m/V,  $\chi^{(2)} \simeq 2 \times 10^{-12}$  m/V,  $\chi^{(3)} \simeq 4 \times 10^{-24}$  m/V, typical values for  $\chi^{(n)}$  in a dielectric [38]).

### 2.1.1 Sum and difference frequency generation

Amongst other effects, the second order nonlinear polarization causes the generation of a combination of new frequency components from incident radiation with two different frequencies. An intense light field  $E(t)$  oscillating at two frequencies  $\omega_1$  and  $\omega_2$  can be described as the superposition of two oscillations with amplitudes  $E_1$  and  $E_2$ :

$$E(t) = E_1 e^{-i\omega_1 t} + E_2 e^{-i\omega_2 t} + cc. \quad (2.3)$$

If this light field interacts with a medium lacking inversion symmetry the second order susceptibility is nonzero and the second order contribution of the nonlinear polarization  $P^{(2)}(t)$  has the following form:

$$\begin{aligned} P^{(2)}(t) &= \epsilon_0 \chi^{(2)} [E_1 e^{-i\omega_1 t} + E_2 e^{-i\omega_2 t}]^2 \\ &= \epsilon_0 \chi^{(2)} [E_1^2 e^{-i2\omega_1 t} + E_2^2 e^{-i2\omega_2 t} + 2E_1 E_2 e^{-i(\omega_1 + \omega_2)t} \\ &\quad + 2E_1 E_2^* e^{-i(\omega_1 - \omega_2)t} + cc.] + 2\epsilon_0 \chi^{(2)} [E_1 E_1^* + E_2 E_2^*], \end{aligned} \quad (2.4)$$

where  $E_n^*$  denotes the complex conjugate of  $E_n$ . Eqn.(2.4) indicates that the second order nonlinear polarization oscillates at four different frequencies, i.e. light with four new frequencies is generated:

- $2\omega_1$ : the second harmonic of the frequency  $\omega_1$
- $2\omega_2$ : the second harmonic of the frequency  $\omega_2$
- $\omega_1 + \omega_2$ : the sum frequency of the incident frequencies
- $|\omega_1 - \omega_2|$ : the difference frequency of the incident frequencies

The constant term of Eqn.(2.4) is referred to as optical rectification and describes a non-vanishing electric field in the temporal average caused by the displacement of the electrons in the anharmonic potential.

The photon energy diagram in Fig.(2.1) illustrates the main difference between sum and difference frequency generation. For the sum frequency, one photon with frequency  $\omega_1$  and one photon with frequency  $\omega_2$  must be destroyed to create one photon with frequency  $\omega_3$ , whereas for the difference frequency each photon with  $\omega_1$  (for  $\omega_1 > \omega_2$ ) creates one photon with frequency  $\omega_2$  and on one photon with frequency  $\omega_3$ . This consequence of energy conservation leads to the amplification of  $\omega_2$  and is known as optical parametric amplification (OPA).

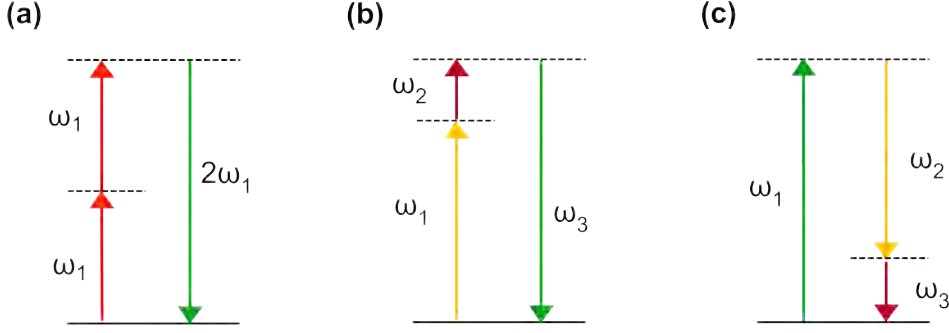


**Figure 2.1:** Photon energy diagram of the second order nonlinear frequency conversion processes: **a)** second harmonic generation, **b)** sum frequency generation, **c)** difference frequency generation.

The efficiency of the described frequency conversion processes is not only determined by the second order nonlinear susceptibility  $\chi^{(2)}$ , which is a material and frequency dependent quantity. The propagation of the different waves inside the material also critically affects the efficiency and leads to the dominance of one process under certain conditions.

### Phase matching

The following considerations describe the case of sum frequency generation (SFG), where  $\omega_3 = \omega_1 + \omega_2$ , but can analogously be applied to second-harmonic generation (SHG) and difference frequency generation (DFG). To calculate the evolution of the SFG-amplitude  $A_3(z)$  upon propagation of the incident light field  $E(t)$  along the  $z$ -axis within a nonlinear medium with negligible losses one has to solve the coupled-amplitude equation [37]:

$$\frac{dA_3}{dz} = \frac{2id_{eff}\omega_3^2}{k_3c^2}A_1A_2e^{i\Delta kz}, \quad (2.5)$$

where  $E_i = A_i e^{ik_i z}$ ,  $d_{eff}$  is the relevant element of the  $d$ -matrix derived from the second order nonlinear susceptibility tensor,  $k_i = \frac{n_i \omega_i}{c}$  is the respective wavevector with  $n_i$  being the refractive index at  $\omega_i$ ,  $c$  is the speed of light, and  $\Delta k = k_1 + k_2 - k_3$  is the wavevector mismatch. Eqn.(2.5) is derived from the nonlinear wave equation using the slowly varying amplitude approximation.

Under the assumption of a small conversion efficiency to the sum frequency  $\omega_3$ , the amplitudes  $A_1$  and  $A_2$  can be approximated by constants and one can integrate Eqn.(2.5) along the  $z$ -axis from 0 to the length of the medium  $L$  [37] to calculate the intensity of the sum frequency  $I_3$ :

$$I_3 = \frac{8d_{eff}^2\omega_3^2 I_1 I_2}{n_1 n_2 n_3 \epsilon_0 c^2} L^2 \text{sinc}^2(\Delta k L / 2), \quad (2.6)$$

with the respective intensity  $I_i = 2n_i\epsilon_0c|A_i|^2$ . The term  $\text{sinc}^2(\Delta kL/2)$  is called phase matching factor and causes an oscillatory behavior of the intensity  $I_3$  for increasing crystal length for a finite  $\Delta k$ . Fig.(2.2) illustrates the evolution of the sum frequency intensity upon propagation inside a nonlinear crystal for a finite  $\Delta k$  and  $\Delta k = 0$ .

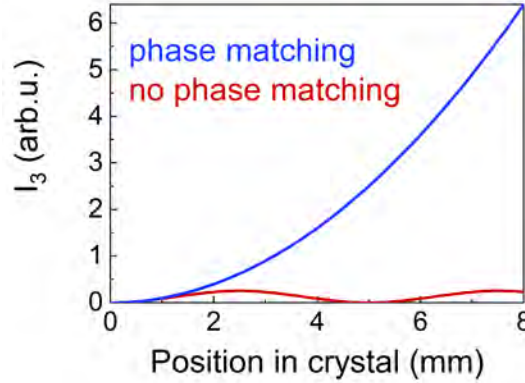


**Figure 2.2:** Evolution of the sum frequency intensity  $I_3$  upon propagation inside a nonlinear crystal for the phase matched (blue) and the phase mismatched (red) case.

This behavior can be explained by the phase relation between the incident and the generated waves. In a microscopic picture, this means only if the dipoles along the medium are excited such that they oscillate in phase the emitted radiation adds up constructively and the conversion to the sum frequency works efficiently. To fulfill this condition, the wavevector mismatch  $\Delta k$  has to be zero which means for collinear beams:

$$\frac{n_3\omega_3}{c} = \frac{n_1\omega_1}{c} + \frac{n_2\omega_2}{c}. \quad (2.7)$$

In the normal dispersion regime, where the refractive index  $n(\omega)$  increases monotonically with increasing frequency  $\omega$  Eqn.(2.7) can usually not be solved and therefore phase matching is achieved with the help of birefringent media. Birefringence means that the refractive index of the medium depends not only on the frequency but also on the orientation of the polarization with respect to the optical axis of the crystal. For sum frequency generation in type I phase matching configuration, the two incident waves have the same polarization and the generated wave is polarized perpendicularly, whereas in type II phase matching the two incident waves are perpendicularly polarized. By adjusting the orientation of the birefringent medium such that the wavevector mismatch vanishes, one can achieve the highest conversion efficiency for SFG.

Also, for perfect phase matching the conversion efficiency does not necessarily increase with the length of the medium  $L$  because of spatial and temporal walk-off effects. On the one hand, for type II phase matching the different propagation directions of the Poynting vector and the electric field for the extraordinary ray limits the spatial overlap of the interacting waves. On the other hand, the mismatch in group velocity between the interacting

laser pulses leads to a temporal walk-off which renders the phase matching bandwidth inversely proportional to the length of the medium  $L$ . Broadband phase matching is crucial when the interaction of ultrashort laser pulses is considered.

### 2.1.2 Intensity dependent refractive index

One consequence of the third order nonlinear polarization is the intensity dependence of the refractive index

$$n = n_0 + n_2 I, \quad (2.8)$$

where  $n_0^2 = 1 + \chi^{(1)}$  is the linear refractive index and  $n_2 = \frac{3}{4n_0^2 \epsilon_0 c} \chi^{(3)}$  [37] is the nonlinear refractive index. As the intensity of a laser pulse varies in space and time Eqn.(2.8) implies two major effects: self-focusing and self-phase modulation (SPM).

#### Self-focusing

For a laser beam with a nonuniform transverse intensity profile, i.e. a Gaussian beam the intensity varies across the beam cross-section. In the case of a Gaussian beam, the intensity decays with increasing distance from the beam axis and thus the center of the beam sees a higher refractive index than the lower-intensity outer region of the beam (for  $n_2 > 0$ ). Consequently, the intensity dependent refractive index causes a Gaussian refractive index profile which acts like a focusing lens.

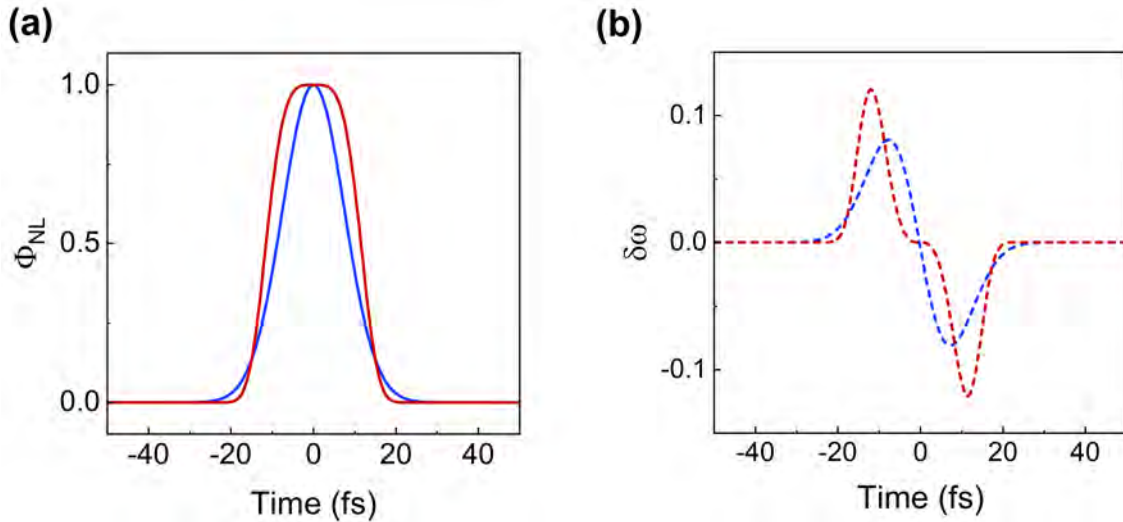


**Figure 2.3:** **a)** The time dependent intensity profile of a Gaussian pulse and a super-Gaussian pulse causes a proportional nonlinear phase shift  $\Phi_{NL}$  in a medium with  $n_2 > 0$  (solid blue line: Gaussian pulse, solid red line: super-Gaussian pulse). **c)** This gives rise to a time dependent frequency shift  $\delta\omega$  (dashed blue line: Gaussian pulse, dashed red line: super-Gaussian pulse) across the pulse.

### Self-phase modulation

Another consequence of the intensity dependent refractive index is the generation of new frequencies due to the temporal variation of the intensity over the duration of a laser pulse. If an intense Gaussian pulse propagates through a nonlinear medium its temporal intensity profile gives rise to a time-dependent nonlinear phase  $\Phi_{NL}(t)$  [39]

$$\Phi_{NL}(t) = \frac{\omega_0 n_2 z}{c} I(t). \quad (2.9)$$

A temporally varying phase implies that the instantaneous frequency deviates from the central frequency  $\omega_0$  across the pulse. The change in instantaneous frequency  $\delta\omega$  is determined by the temporal derivative of the nonlinear phase:

$$\delta\omega = -\frac{d}{dt}\Phi_{NL}(t). \quad (2.10)$$

As can be seen from Eqn.(2.9), the magnitude of  $\delta\omega$  grows with the propagation distance  $z$  and leads to an increase in spectral bandwidth for initially unchirped pulses.

Fig.(2.3) shows the nonlinear phase shift and the change in instantaneous frequency for the propagation of a Gaussian pulse (blue) and super-Gaussian pulse (red) in a nonlinear medium with  $n_2 > 0$ . For the Gaussian pulse, the change in instantaneous frequency increases linearly over a large central region of the pulse which means a positive linear chirp is introduced. For the super-Gaussian pulse, the instantaneous frequency change is zero in the center of the pulse but reaches higher values than for the Gaussian pulse at the edge of the pulse. For both input pulses the same change in instantaneous frequency is reached at two different points in time which explains the typical oscillatory behavior observed for SPM-broadened spectra caused by the interference of identical spectral components with different phase. Fig.(2.3) illustrates that the shape of SPM-broadened spectra critically depends on the input pulse shape. Of course, the finite initial chirp of a pulse can also affect the resulting spectral shape and coverage.

### 2.1.3 Electro-optic sampling

Another consequence of the second order nonlinear polarization is the (linear) electro-optic or Pockels' effect. This effect describes the modification of the refractive index of a non-centrosymmetric medium proportional to the field strength of an applied electric field. In combination with ultrashort pulses, this effect can be exploited to measure electric field transients with carrier frequency  $\Omega$  whose half cycle duration  $\pi/\Omega$  can be as short as the duration of the ultrashort pulse [40]. If the electric field transient and the ultrashort pulse co-propagate in a nonlinear medium, the refractive index change proportional to the instantaneous electric field of the transient introduces a birefringence affecting the polarization of the ultrashort pulse [41]. By analyzing the polarization change of the ultrashort pulse and delaying it with respect to the transient one can gain access to the temporally resolved electric field of the transient [42].

This intuitive time-domain picture of an introduced birefringence was established in the context of the detection of far infrared radiation where the detected frequency  $\Omega$  is much smaller than the carrier frequency of the NIR sampling pulse. In this case, one can assume the detected electric field to be constant for the duration of the sampling pulse. If MIR radiation is detected, its frequency  $\Omega$  is much closer to the carrier frequency of the sampling pulse and it is more appropriate to explain the process of electro-optic sampling (EOS) in a frequency domain picture [43].

In the frequency domain, EOS can be understood in a two-step model: The co-propagation of NIR and MIR pulse in a nonlinear medium lacking inversion symmetry leads to the generation of their sum and difference frequency. The interference of the NIR pulse with the orthogonally polarized sum-frequency wave results in a modified polarization state in the frequency range of their spectral overlap which is detected with an ellipsometer. Recording the resulting signal as a function of the mutual delay between NIR and MIR pulse yields a signal linearly proportional to the amplitude of the electric field of the MIR radiation preserving its sign [31]. In the following, equations for the magnitude of the EOS signal will be derived.

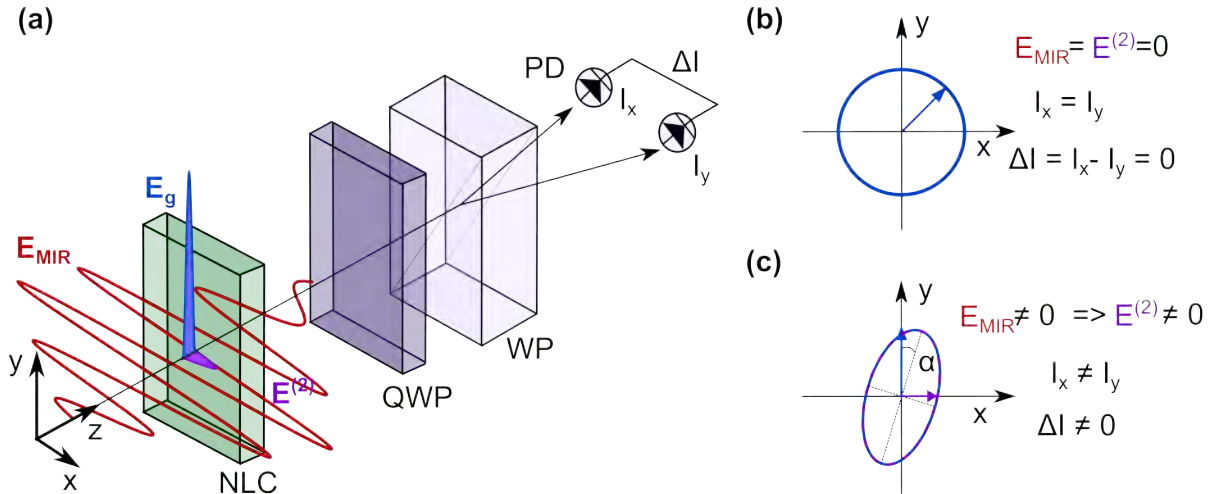


**Figure 2.4:** Electro-optic sampling geometry: **a)** Nonlinear mixing within the nonlinear crystal (NLC) of the mid-infrared pulse  $E_{MIR}$  (linearly polarized along the  $x$ -axis) and the gate pulse  $E_g$  (linearly polarized along the  $y$ -axis) generates sum-frequency components  $E^{(2)}$  linearly polarized along the  $y$ -axis. A quarter waveplate (QWP) combined with a Wollaston prism (WP) analyzes the polarization state of the interference between  $E_g$  and  $E^{(2)}$  which is detected with a differential photo diode (PD). **b)** If no mid-infrared pulse is present the polarization after the QWP is circular and the differential current  $\Delta I$  is balanced to zero. **a)** If a mid-infrared pulse is present the polarization after the QWP is elliptical with  $\alpha$  depending on the phase shift between  $E_g$  and  $E^{(2)}$  which results in a finite  $\Delta I$ .

According to Eqn.(2.4), the nonlinear polarization  $P^{(2)}$  caused by the mixing of the

electric fields of the MIR pulse  $E_{MIR}(\Omega)$  and the NIR pulse  $E_g(\omega_2)$  is given by:

$$P^{(2)}(\omega_3) = \epsilon_0 \chi^{(2)}(\omega_3) E_{MIR}(\Omega) E_g(\omega_2), \quad (2.11)$$

for the sum frequency  $\omega_3 = \omega_2 + \Omega$  and

$$P^{(2)}(\omega_4) = \epsilon_0 \chi^{(2)}(\omega_4) E_{MIR}(\Omega) E_g^*(\omega_2), \quad (2.12)$$

for the difference frequency  $\omega_4 = \omega_2 - \Omega$ . For a frequency  $\omega$  within the spectral coverage of the gate pulse a sum and a difference frequency contribution at the same frequency  $\omega$  can be found for  $\omega_2 = \omega - \Omega$  and  $\omega_2 = \omega + \Omega$ , respectively. After propagation through a nonlinear medium these contributions are given by [44]:

$$E^{(2)}(\omega) = -i \int_{-\infty}^{\infty} R(\Omega) E_{MIR}(\Omega) E_g(\omega - \Omega) d\Omega, \quad (2.13)$$

where  $R(\Omega)$  is a response function which contains the frequency dependence of the nonlinear susceptibility and the phase matching factor as described in the previous section. The interference between the newly generated components  $E^{(2)}(\omega)$  and the gate pulse  $E_g(\omega)$  constitutes the EOS signal.

In the typical geometry of EOS detection, the mid-infrared waveform  $\mathbf{E}_{MIR}$  and the gate pulse  $\mathbf{E}_g$  are polarized linearly and perpendicularly to each other such that the newly generated components  $\mathbf{E}^{(2)}$  spectrally overlap with the gate pulse but have perpendicular polarization as illustrated in Fig.(2.4a). To enable interference between the gate pulse and the newly generated components, their polarizations have to be combined by projecting them onto a new axis. This can be achieved with a phase retarder, i.e. a quarter- or a half-wave plate. The resulting polarization state of the combined electric field  $\mathbf{E}_g + \mathbf{E}^{(2)}$  is analyzed using a Wollaston prism whose outputs are sent onto the photo diodes of a differential detector. By carefully adjusting the angle of the fast axis of the phase retarder with respect to the Wollaston prism the recorded signal at the detector vanishes if the mid-infrared field is zero as illustrated in Fig.(2.4b).

The polarization state of the combined electric field is determined by the magnitude of the gate pulse  $\mathbf{E}_g$  and the newly generated components  $\mathbf{E}^{(2)}$  and their respective phase shift. The phase shift is given by [45]

$$\Delta\phi = \pi/2 + \phi_0 + \Omega\tau, \quad (2.14)$$

where  $\tau$  is the relative delay between the sampling pulse and the mid-infrared waveform and  $\phi_0$  is a delay independent phase shift occurring for example due to birefringence in the nonlinear medium. For a non-zero mid-infrared field, the combined polarization is elliptical with a rotated main axis for  $\Delta\phi \neq \pi/2$  (see Fig. (2.4c)). This results in the detection of a finite differential current  $\Delta I$  at the balanced photodiode [44]:

$$\Delta I(\tau) \propto \int_{-\infty}^{\infty} \int_{-\infty}^{\infty} R(\Omega) E_{MIR}(\Omega) E_g^*(\omega - \Omega) E_g(\omega) e^{i\Omega\tau} d\Omega d\omega. \quad (2.15)$$

Eqn.(2.15) shows that the EOS-signal scales with the electric field of the MIR waveform and the intensity autocorrelation of the sampling pulse  $I_{AC,g} = \int_{-\infty}^{\infty} E_g^*(\omega - \Omega)E_g(\omega)d\omega$ . The dependence of the differential current on the response function  $R(\Omega)$  indicates that to reconstruct the actual electric field of the MIR waveform from the measured EOS-signal one needs to calculate the frequency-dependent response function of the specific EOS detection setup.



# Chapter 3

## Electric-field-resolving spectrometer

To gain access to the interaction of molecules and light on the level of the electric field with a sensitivity outperforming common techniques like FTIR spectroscopy, we developed a spectroscopic instrument we call *Infrasampler*. The main part of the experimental work of this thesis consisted in the design and construction of the field-resolving spectrometer. Its working principles and exact implementation in the laboratory are explained in the following. The first two sections of this chapter are dedicated to the broadband light source employed in the *Infrasampler*. It is based on the nonlinear down-conversion of pulsed NIR radiation to gain phase-stable, superoctave MIR waveforms. The electric-field-resolved detection thereof is enabled by electro-optic sampling. Its realization and its advantages over common spectroscopic techniques are described in the third and fourth section of this chapter. To evaluate the performance of the developed instrument it is benchmarked against state-of-the-art spectrometers in the fifth section. Finally, the last section of this chapter presents different approaches towards a rapid scanning *Infrasampler* including first experimental results.

### 3.1 Ultrashort driving pulses in the near-infrared

Due to the comparably small magnitude of the nonlinear susceptibility, it is necessary to generate very high laser intensities to efficiently exploit the nonlinear phenomena described in Chapter 2. The laser intensity scales inversely with the spatial and temporal extent to which its radiation is confined. By modelocking a laser resonator we can produce a train of short laser pulses instead of continuously emitted radiation. The pulse energy delivered by a modelocked oscillator is sufficient to generate new frequency components via self-phase modulation in a nonlinear medium and subsequently decrease the pulse duration and, thus increase the intensity.

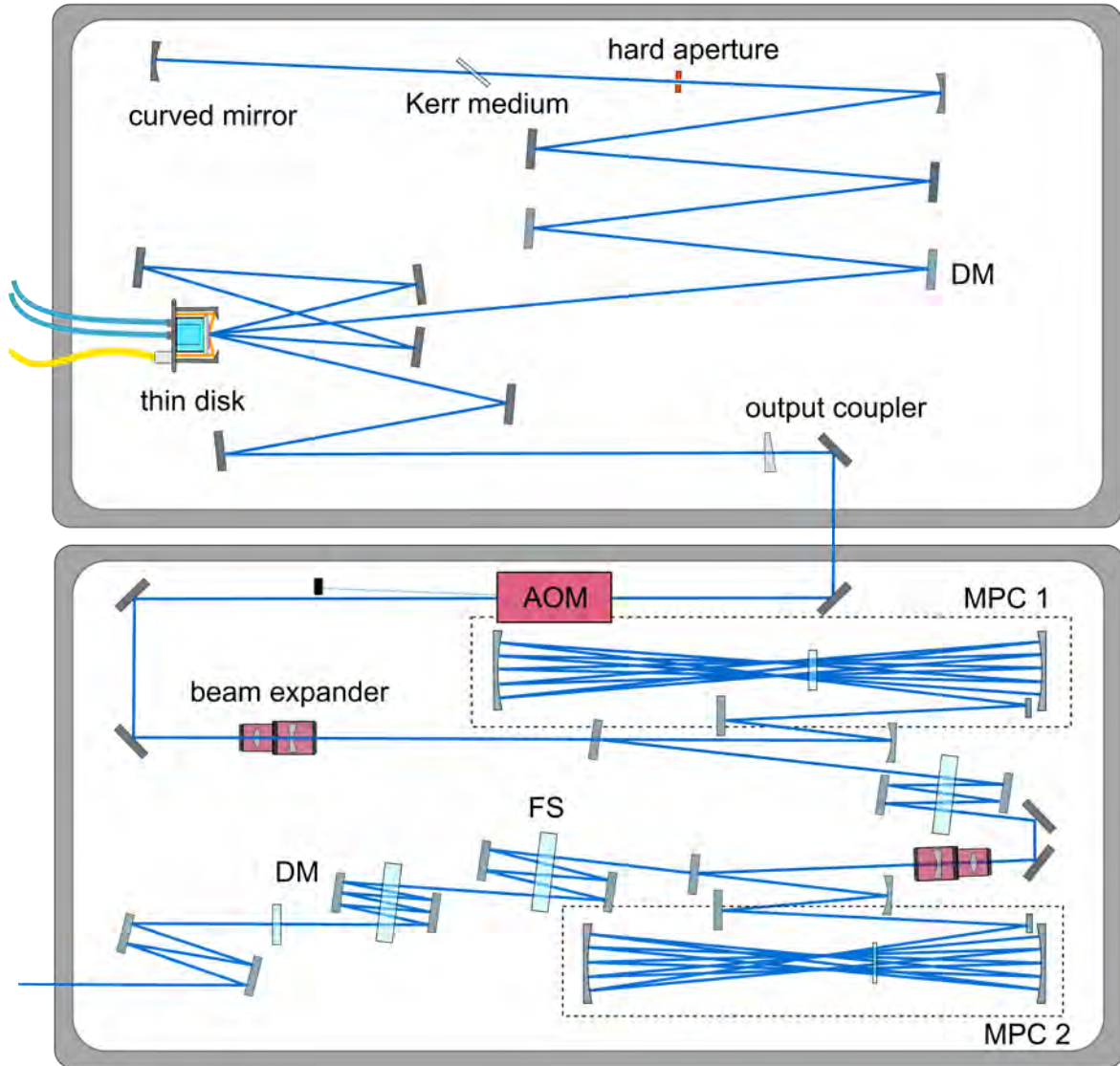


**Figure 3.1:** Sketch of the Kerr-lens modelocked Yb:YAG thin disk oscillator and the extra-cavity broadening setup consisting of two multi pass cells for spectral broadening and a combination of fused silica (FS) and dispersive mirrors (DM) for compression. AOM: acousto-optic modulator.

### 3.1.1 Kerr-lens modelocked Yb:YAG thin-disk oscillator

Besides the high intensity of a laser system to drive nonlinear conversion processes, its average power is critical for spectroscopic applications demanding a high signal-to-noise ratio within short measurement times. Compared to Ti:Sa oscillators, Yb-doped thin-disk oscillators deliver more than two orders of magnitude higher average powers, routinely reaching more than 100 Watts of output power at MHz repetitions rates [46, 23]. Since

the first demonstration of a Kerr-lens modelocked Yb:YAG thin-disk oscillator in 2011 [47] this technology has evolved and now delivers compact, user-friendly, and reliable laser sources for spectroscopic applications without the need for extra-cavity amplifiers.

In a modelocked laser resonator, the phase-coherent interference of the longitudinal cavity modes leads to the formation of an ultrashort laser pulse circulating inside the cavity [48]. Each time the circulating laser pulse hits the output coupler of the cavity a small portion of its power leaves the oscillator. Thus, a train of laser pulses emerges with the temporal separation of one round trip time  $T_{rep}$ . In the frequency domain this train of pulses corresponds to a spectrum of evenly spaced frequency modes separated by the inverse round trip time  $f_{rep} = 1/T_{rep}$  referred to as repetition rate.

To achieve a stable phase relation between the longitudinal cavity modes, the resonator has to be operated in a regime where the modelocked state is more favorable than continuous wave (CW) operation. In the case of hard aperture Kerr-lens modelocking (KLM), this is achieved by introducing an aperture inside the resonator. Due to self-focusing inside a transmissive element the laser beam experiences an intensity-dependent Kerr lens which leads to a smaller beam size at the aperture and therefore smaller losses for the modelocked state [49].

The Kerr-lens modelocked Yb:YAG thin-disk oscillator employed in this thesis was designed and constructed by my co-worker Kilian Fritsch. A sketch of the resonator is shown in Fig.(3.1). In this type of oscillator, the active medium is a thin layer ( $> 200 \mu\text{m}$ ) of ytterbium-doped yttrium aluminium garnet (Yb:YAG) firmly connected to a water-cooled heat sink. The large contact surface between the active medium and the heat sink guarantee efficient cooling and enable kW-scale pump powers. The contacted surface of the thin disk has a highly reflective (HR) coating for the pump and the laser wavelength whereas the other surface is anti-reflection (AR) coated. The gain medium is pumped with a fiber coupled diode laser delivering 420 W at 940 nm.

The resonator design features a double pass over the thin disk resulting in an eightfold transmission through the active medium per round trip. Unlike in bulk solid-state lasers, the thickness of the active medium is not sufficient to act as a Kerr lens. Therefore a 1-mm thick fused silica (FS) plate at Brewster's angle was introduced in the focus of two curved mirrors with radius of curvature (ROC) of 500 mm. The selection of Brewster's angle provides linearly, p-polarized laser output. The water-cooled hard aperture made of copper was placed at a position where the difference in beam size between modelocked and CW operation is large, in order to achieve a strong loss modulation. Two dispersive mirrors with a total group delay dispersion (GDD) of  $-6000 \text{ fs}^2$  were integrated in the cavity for dispersion management.

The resonator length of 5.35 m resulted in a repetition rate of 28 MHz in a compact housing with a foot print of  $0.6 \text{ m}^2$ . With a 18 % output coupler, 105 W of average power with a pulse duration of 261 fs were achieved. To minimize the influence of environmental conditions on pulse duration and long-term stability, the oscillator housing was continuously flushed with humidity-stabilized air (Relative Humidity Generator RH-200, L&C Science and Technology, Inc.). At a flow of  $\approx 4 \text{ l/min}$  a constant relative humidity of 28

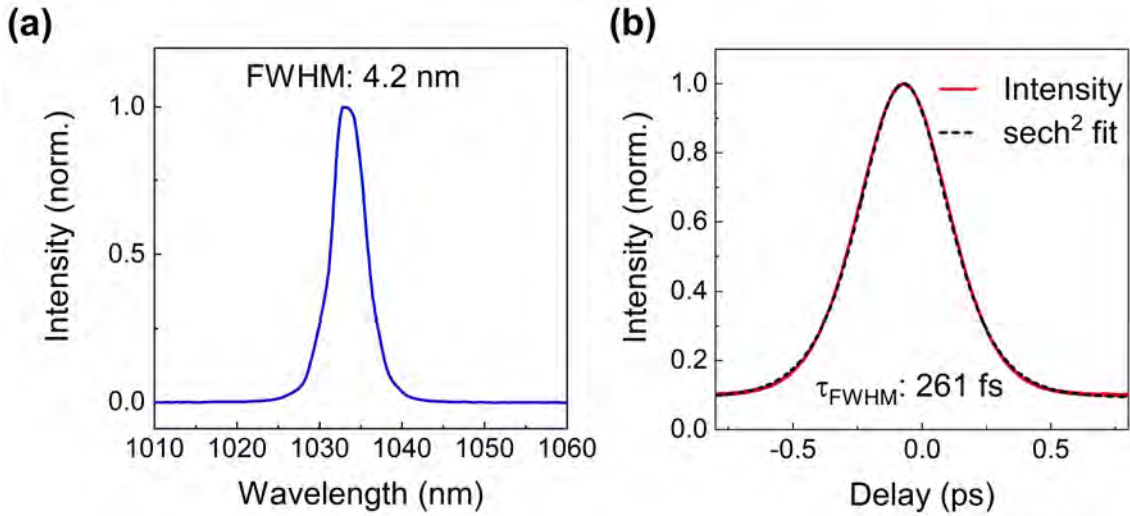


**Figure 3.2:** Parameters of the Yb:YAG thin-disk oscillator with a repetition rate of 28 MHz and an average power of 105 W: **a)** spectrum and **b)** intensity autocorrelation of the modelocked oscillator.

% at room temperature was achieved.

Fig.(3.2) shows the spectrum of the output pulses centered at 1033 nm and their intensity autocorrelation. The ideal pulse shape expected from a soliton modelocked oscillator is a  $\text{sech}^2$ -pulse. The good agreement between the intensity autocorrelation of the output pulses and the fitted autocorrelation of a  $\text{sech}^2$ -pulse in Fig.(3.2b) is an indicator for the high pulse quality. The full width at half maximum (FWHM) of 403 fs of the autocorrelation corresponds to a  $\text{sech}^2$ -pulse duration of 261 fs.

For subsequent frequency down-conversion of the NIR radiation to the MIR region the 1- $\mu\text{m}$  emission wavelength of Yb-based lasers is not the most efficient starting point. A longer driving wavelength enables the use of nonlinear crystals with a smaller bandgap and therefore higher nonlinear coefficients [50]. At the same time, the reduced group velocity mismatch between driving and generated wave allows for a broader phase matching bandwidth [51]. Over the last years, laser sources with an emission wavelength around 2  $\mu\text{m}$  based on new active media like thulium-doped fibers [52], holmium-doped thin disks [26] and chromium-doped bulk crystals [27] have emerged. Despite the impressive progress in this field and the advantages of a longer driving wavelength, the lack of commercial optics and diagnostics as well as the not fully mature development state of 2 $\mu\text{m}$ -based systems when this project was started justify the choice of the well-established 1- $\mu\text{m}$  technology as driving source.

### 3.1.2 Self-phase-modulation-based spectral broadening and pulse compression

Compared to Ti:Sa lasers where pulse durations below 10 fs are commonly generated directly in the oscillator [53], the narrow emission bandwidth of Yb:YAG of around 8 nm limits the oscillator pulse duration to  $>100$  fs [54]. This is neither sufficient for broadband MIR generation nor for the electro-optic sampling of radiation down to 5  $\mu\text{m}$ .

The minimum pulse duration for a certain spectral bandwidth is given by the pulse-shape-dependent time-bandwidth product. As a consequence of the properties of the Fourier transformation which connects the time and the frequency domains, the duration of a pulse is inversely proportional to its frequency bandwidth. Thus, the bandwidth of the oscillator pulses must be increased via extra-cavity spectral broadening to enable shorter pulse durations.

Depending on the exact combination of laser parameters, a variety of extra-cavity spectral broadening schemes has evolved which all depend on SPM in  $\chi^{(3)}$ -nonlinear media. Due to their long interaction length and their wave-guiding properties circumventing self-focusing, fiber-based approaches are often the method of choice. However, for solid-core photonic-crystal fiber (PCF) the threshold for self-focusing in FS limits the input peak power to below 4 MW. To circumvent this peak power limitation, hollow-core capillaries or PCFs filled with noble gases are used. In this case, the onset of plasma-formation for repetition rates above 20 MHz is the limiting factor. In addition, nonlinear fibers are prone to damage and very alignment-sensitive which turns beam-pointing fluctuations into intensity fluctuations.

A cheap and robust alternative to nonlinear fibers is SPM in bulk media. However, due to the lack of wave-guiding mechanisms in bulk material, spatio-temporal coupling leads to a degradation of the beam profile and spatially inhomogeneous spectral broadening [55]. By distributing the spectral broadening over several passes through a thin nonlinear medium inside a multi-pass cell (MPC) the beam quality can be preserved [56]. If the nonlinear spatial phase shift acquired upon a single pass through the thin medium is small compared to the spatial phase shift introduced by propagating over one round trip inside the MPC spatial effects are homogenized and spectral broadening can be decoupled from self-focusing [57]. This quasi-waveguide approach combines the advantages of fiber and bulk spectral broadening.

Similar to the layout described in [58], my former colleague Kilian Fritsch designed and constructed a two-stage spectral broadening unit based on distributed SPM in a MPC to compress the 260-fs output pulses of the Kerr-lens modelocked Yb:YAG thin-disk oscillator to 14 fs. A sketch of the setup is shown in Fig.(3.1). In the broadening unit, each MPC is followed by a set of tailored dispersive mirrors for pulse compression. The Herriottcell-type multi-pass geometry is realized by two concave mirrors facing each other and a scraper mirror in front of one of the cell mirrors for off-axis in- and out-coupling. Depending on the distance between the cell mirrors the beam completes a certain number of round trips before it hits the scraper mirror again and leaves the MPC under a slightly different vertical angle.

During each round trip the beam passes twice through the broadening medium which is AR coated on both surfaces to minimize losses.

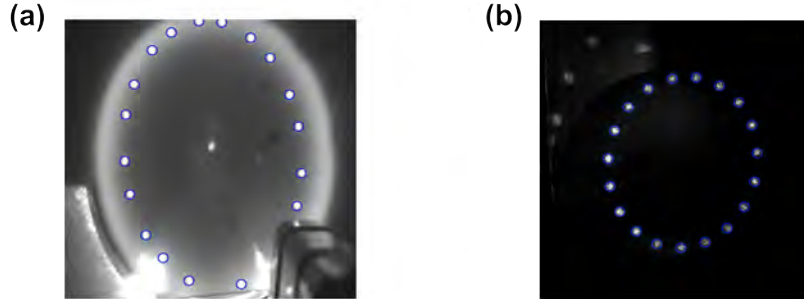


**Figure 3.3:** Spot pattern on the Herriott cell mirrors for **a)** 21 round trips in the first broadening stage and **b)** 19 round trips in the second broadening stage.

To compensate for the material dispersion of the broadening medium, each cell mirror has a dispersive coating. Due to the large number of round trips, a slight dispersion mismatch between cell mirrors and broadening medium leads to a huge positive or negative net dispersion. In the negative dispersion regime, self-compression upon propagation through the MPC occurs which can cause strong self-focusing and intensity-induced damages in the nonlinear medium. It also results in worse compressibility of the output spectrum. Therefore, the positive dispersion regime is preferred. The thickness of the nonlinear medium and its distance from the center of the MPC, i.e. from the focus, determine the nonlinear phase shift per pass for given laser pulse parameters. A phase shift of 0.6 rad was identified to be the threshold for operation in the quasi-waveguide regime [58].

The first MPC of the setup consists of two concave mirrors with a ROC of 200 mm and a diameter of 50.4 mm. To compensate for the dispersion of the 6.35 mm thick FS plate which acts as nonlinear medium each mirror has a dispersion of  $-120 \text{ fs}^2$  GDD and  $-260 \text{ fs}^3$  third order dispersion (TOD). A distance of 576 mm between the cell mirrors resulted in 21 round trips, i.e. 42 passes through the nonlinear medium and the elliptical spot pattern on the mirrors shown in Fig.(3.3a). For transverse mode matching, two concave mirrors with ROC 1000 mm and a commercial beam expander (Eksma Optics, 165-1181) were used. Before the beam enters the second MPC, four reflections on dispersive mirrors with  $-120 \text{ fs}^2$  GDD were implemented to compress the dispersion introduced by the nonlinear interaction.

The output pulses were characterized with the technique of frequency-resolved optical gating (FROG) employing a 10  $\mu\text{m}$  thick BBO crystal for SHG. Fig.(3.4a) shows the resulting FROG trace and its retrieval. The good agreement between measurement and retrieval is also represented by the FROG error of 0.002 and indicates the convergence of the retrieval algorithm. Another indicator for the plausibility of the FROG results is the agreement of the retrieved spectrum and the pulse spectrum measured with an

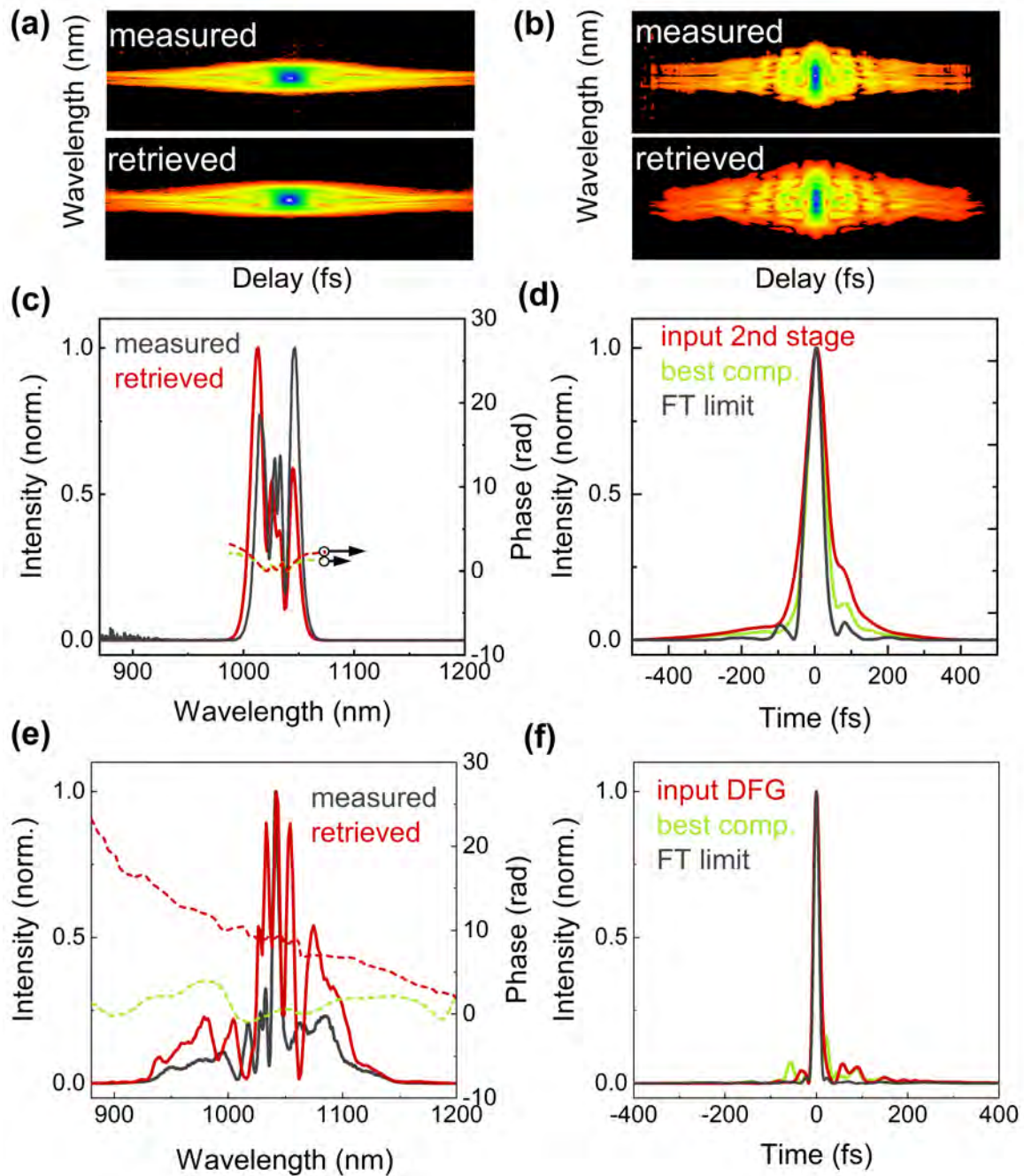


**Figure 3.4:** Measured and retrieved SHG-FROG trace of the NIR pulse after the first MPC and the compression set (a) and after the second MPC and compression set (b). Spectrum of the NIR pulses after the first MPC and the compression set (c) and after the second MPC and compression set (e) measured with an optical spectrum analyzer (OSA) and retrieved from the FROG trace. The dashed lines denote the spectral phase. Temporal intensity profile of the NIR pulses after the first MPC and the compression set (d) and the second MPC and compression set (f) retrieved from the FROG measurement for different amounts of FS (see main text). For comparison, the FTL is shown.

optical spectrum analyzer (OSA) shown in Fig.(3.4c). The according spectral phases are depicted for two different configurations of the compression set. When 31 mm FS were removed from the compression set, the shortest pulse duration of 52 fs FWHM was achieved. For comparison, Fig.(3.4d) shows the retrieved intensity profile of the pulses and the Fourier transform limit (FTL) of 51 fs calculated from the measured spectrum assuming a flat spectral phase. When the removed FS was inserted again, the measured pulse duration increased to 64 fs and the according spectral phase exhibited higher positive GDD (stronger curvature). Despite the longer pulse duration, this configuration was preferred as input for the second MPC because it does not have a pronounced side pulse feature.

The second rise of the pulse intensity after the main peak causes higher-order dispersion contributions during SPM which are difficult to compensate for. The broadening factor, i.e. the ratio of Fourier-transform-limited input and output pulse duration for the first compression stage is 5.

The main difference between the first and the second MPC is the thickness of the nonlinear medium. The second MPC consists of a 3-mm thick AR coated FS plate and two concave mirrors with ROC 300 mm. Compared to the first MPC the dispersion of the cell mirrors is reduced to  $-60 \text{ fs}^2$  GDD and  $-130 \text{ fs}^3$  TOD. With a MPC length of 382 mm, 19 round trips were realized generating the spot patten shown in Fig.(3.3b). In total,  $-1680 \text{ fs}^2$  of GDD and 62 mm of FS were used for compression.

The comparison of the measured and the retrieved FROG trace in Fig.(3.4b), the FROG error of 0.004, and the agreement between the independently measured and retrieved spectrum in Fig.(3.4e) document the credibility of the FROG measurement. Again, two different compression configurations are shown in Fig.(3.4f). The shortest pulse duration of 15 fs was achieved by adding 3 mm FS. However, for subsequent frequency down-conversion a slightly down-chirped pulse was preferred. Without the additional FS, the pulse duration was 16 fs with 78 % of the pulse energy in the main peak. Although the FWHM pulse duration of the compressed pulse is very close to the calculated FT limit of 14 fs, the measured pulses exhibit more distinct side pulse features. This is caused by dispersion contributions of higher than third order which are not considered in the dispersive mirror design. Additionally, residual TOD from overcompensation and accumulating GDD oscillations from the high number of reflections on the dispersive cell mirrors are difficult to compensate for.

The overall broadening factor of the two-stage setup is 18 and the overall output power is 66 W corresponding to a pulse energy of 2.4  $\mu\text{J}$  at a pulse duration of 15 fs and a throughput efficiency of 73 %, at 90 W input power.

Since the MPC approach includes rather long beam paths in air ( $> 40 \text{ m}$ ), small changes in the relative humidity can noticeably affect the dispersion of the pulses. To optimize the day-by-day reproducibility of the output pulse shape, the broadening chamber was continuously flushed with dry air to achieve a constant relative humidity of 2 % at room temperature.

## 3.2 Phase-stable mid-infrared waveforms

The molecular fingerprint region between 2 and 20  $\mu\text{m}$  where most organic molecules have vibrational resonances is not entirely accessible via active laser media. In recent years, there has been tremendous progress in the development of laser sources emitting around 2  $\mu\text{m}$  [52, 26, 27]. Also quantum cascade lasers offer coherent radiation between 3 and 25  $\mu\text{m}$  [19] but they emit tunable narrow bandwidth spectra and are therefore not suitable for time-resolved measurements. For many spectroscopies in the molecular fingerprint region either non-coherent white light sources or - if affordable - large-scale facilities like synchrotrons with high brightness are the method of choice. By nonlinear down-conversion of 1  $\mu\text{m}$  lasers it is possible to create a low-noise, coherent table-top source of broadband MIR radiation temporally confined to a few oscillations of the electric field [24].

### 3.2.1 Intrapulse difference frequency generation

Compared to other nonlinear down-conversion processes, DFG allows for the generation of inherently phase-stable MIR waveforms if implemented in an intrapulse scheme. Nonlinear mixing of the different frequency components of a single broadband NIR driver inside a nonlinear crystal is a very simple and compact approach superseding the necessity of temporal and spatial overlapping of two distinct pulses as for example in OPA.

The spectrum of a modelocked oscillators consists of a comb of frequency modes with an equal spacing  $f_{rep}$  and a common frequency offset  $f_{CEO}$  from zero. In the time-domain, the carrier-envelope offset (CEO) frequency  $f_{CEO}$  causes a pulse-to-pulse phase shift  $\Delta\phi = 2\pi f_{CEO}/f_{rep}$  of the electric field of the carrier wave with respect to the envelope of each laser pulse emitted by the oscillator [59]. Within a single laser pulse all frequency modes  $\nu_n = n f_{rep} + f_{CEO}$  have the same CEO frequency  $f_{CEO}$ . Thus, by generating their difference frequency  $\nu_{n,m} = |\nu_n - \nu_m| = |n - m| f_{rep}$  the CEO frequency cancels and the resulting intrapulse difference frequency waveform is CEO phase-stable [60]. Phase-stability is a crucial prerequisite for the subsequent detection of the MIR waveforms with EOS. In our group, it was shown that the phase fluctuations of IPDFG waveforms are as low as 0.18 mrad at a center wavelength of 8  $\mu\text{m}$  measured in the frequency band between 10 kHz and 0.625 MHz [61].

For efficient broadband IPDFG, the choice of the nonlinear crystal is essential. LiGaS<sub>2</sub> (LGS) cut at  $\phi = 0^\circ$  and  $\theta = 48^\circ$  offers good conditions for broadband type I phase matching, a transparency up to 12  $\mu\text{m}$ , and a high laser-induced damage threshold of 1 TW/cm<sup>2</sup> due to the comparably high band gap preventing multiphoton absorption. The crystal thickness of 1 mm is a trade-off between phase matching bandwidth and conversion efficiency. It is possible to AR coat the crystal surfaces for the NIR, however the AR coating was observed to reduce the damage threshold and is therefore not favorable.

To achieve the shortest driving pulse duration in the center of the LGS crystal, the pulses were slightly down-chirped by removing 3 mm of FS compared to the compression configuration for the shortest pulses. This 3 mm of FS have a similar GDD as 0.5 mm

LGS. A sketch of the IPDFG setup is shown in Fig.(3.8) The resulting 16-fs long pulses were focused to a 190- $\mu\text{m}$  spot (diameter at FWHM, see Fig.(3.5a)) using an AR coated plano-convex N-BK7 lens with a focal length of 750 mm. The choice of the lens coating and material is crucial to avoid beam degradation due to thermal effects. The crystal was placed 10 mm in front of the focus where the spot size is 200  $\mu\text{m}$  to avoid self-focusing and to guarantee long-term operation without crystal degradation well below the damage threshold. The peak intensity on the crystal surface was calculated to 320  $\text{GW}/\text{cm}^2$ .

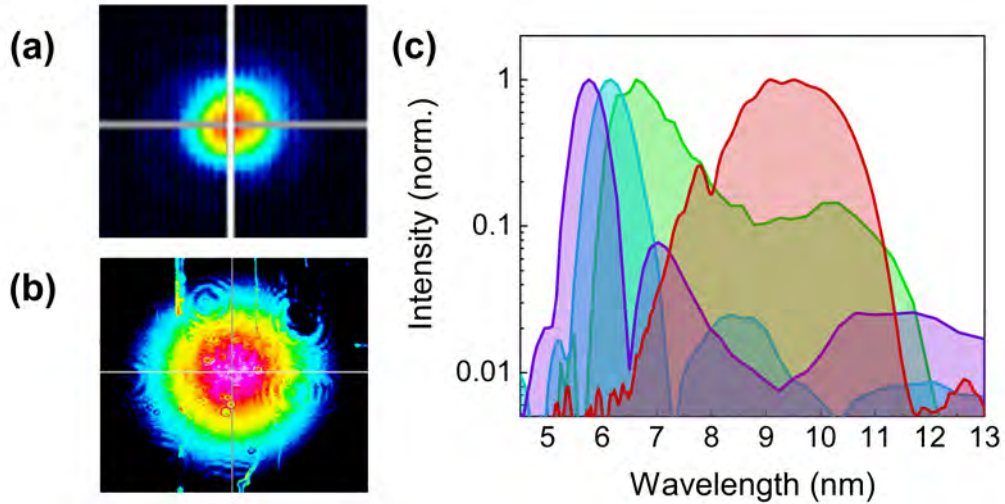


**Figure 3.5:** a) Beam profile of the driving NIR pulses in the focus of a lens with 750 mm focal length. b) Beam profile of the generated MIR radiation after collimation with a parabolic mirror with effective focal length (EFL) length of 101.6 mm. c) Spectra of the generated MIR radiation for different phase matching configurations of the nonlinear crystal measured with a FTIR spectrometer.

The crystal is mounted in such a way that the orientation of  $\theta$  and  $\phi$  as well as the crystal tilt with respect to the vertical axis can be controlled externally with a stepper motor. In type I phase matching, the polarization of the incident beam with respect to the crystal orientation is chosen such that the frequency components are projected evenly onto the ordinary and extraordinary axis of the crystal. By increasing the number of blue photons projected to the extraordinary axis compared to the red photons, the efficiency of the down-conversion process can be increased [62]. To achieve this favorable condition, the fast axes of a combination of a QWP and a half waveplate (HWP) were adjusted until the MIR output power was maximized. The newly generated frequencies were polarized along the ordinary crystal axis. To achieve linearly p-polarized MIR radiation, the crystal angle  $\theta$  had to be oriented accordingly.

After IPDFG, the newly generated MIR radiation was separated from the NIR radiation using a 1-mm thick ZnSe plate which has a reflective coating for the NIR on the first surface and an AR coating for the MIR on the second surface. The MIR radiation was collimated using a bare gold parabolic mirror with an EFL of 101.6 mm to a spot size of

6.1 mm (diameter at FWHM, see Fig.(3.5b)). To characterize the spectral coverage of the generated MIR radiation it was coupled into a FTIR spectrometer which compared to EOS detection offers a flat frequency response. Fig.(3.5c) shows the normalized spectra recorded for different orientations of the LGS crystal. Depending on phase matching, frequencies below 5  $\mu\text{m}$  and above 12  $\mu\text{m}$  were generated. The average MIR power measured for the different spectra varied: 13 mW for the purple spectrum, 27 mW for blue spectrum, 52 mW for the green spectrum, and 87 mW for the red spectrum. This can be explained by the shape of the generating spectrum and the efficiency of the DFG process. For the further experiments, the most broadband spectrum (green line in Fig.(3.5c)) was chosen, which spans from 5 to 12  $\mu\text{m}$  at -20 dB. With a wire-grid polarizer, the MIR radiation was characterized to be 98 % p-polarized.

### 3.2.2 Active intensity noise stabilization

The fundamental sensitivity limit in classical spectroscopy is given by the photon shot noise owing to the particle nature of light. However, it is technically challenging to reach this fundamental limit in the presence of detector noise and intensity source noise. Especially in the MIR spectral region for most applications, detectors are the dominating source of noise. This is caused by the combination of very low brightness thermal light sources and the poor noise performance of available IR detectors. In the *Infrasampler* concept, we mitigate these limitations by employing a coherent light source with sufficiently high average powers and frequency up-conversion to the NIR during EOS detection where more sensitive detectors are available. Compared to incoherent thermal light sources however, laser-based sources exhibit an increased intensity noise especially in the frequency band below 100 kHz. During nonlinear broadening and down-conversion, the intensity noise is additionally amplified.

Fig.(3.6a) shows the RIN of the Kerr-lens modelocked Yb:YAG oscillator (black) up to 100 kHz. For this measurement, a small portion of the oscillator output power was sent to an amplified InGaAs-photodetector and the recorded voltage noise spectrum  $S(f)$  (in  $V/\text{Hz}^{1/2}$ ) was normalized to the DC voltage. The integrated root mean square RIN in a frequency band between  $f_0$  and  $f_1$  is given by:

$$RIN_{rms} = \sqrt{\int_{f_0}^{f_1} \frac{S(f)^2}{V_{DC}} df}. \quad (3.1)$$

For the oscillator the integrated RIN between 1 Hz and 100 kHz amounted to 0.03 % which is in good agreement with previously published values for comparable systems [63]. The oscillator RIN exhibited the typical 1/f-behaviour because the main contributions stem from excess noise of the pump diode, mechanical vibrations, and thermal fluctuations in the thin disk which all decay with increasing frequency. The dominant peaks at 50 Hz and 100 Hz correspond to the alternating frequency of the electricity network and common

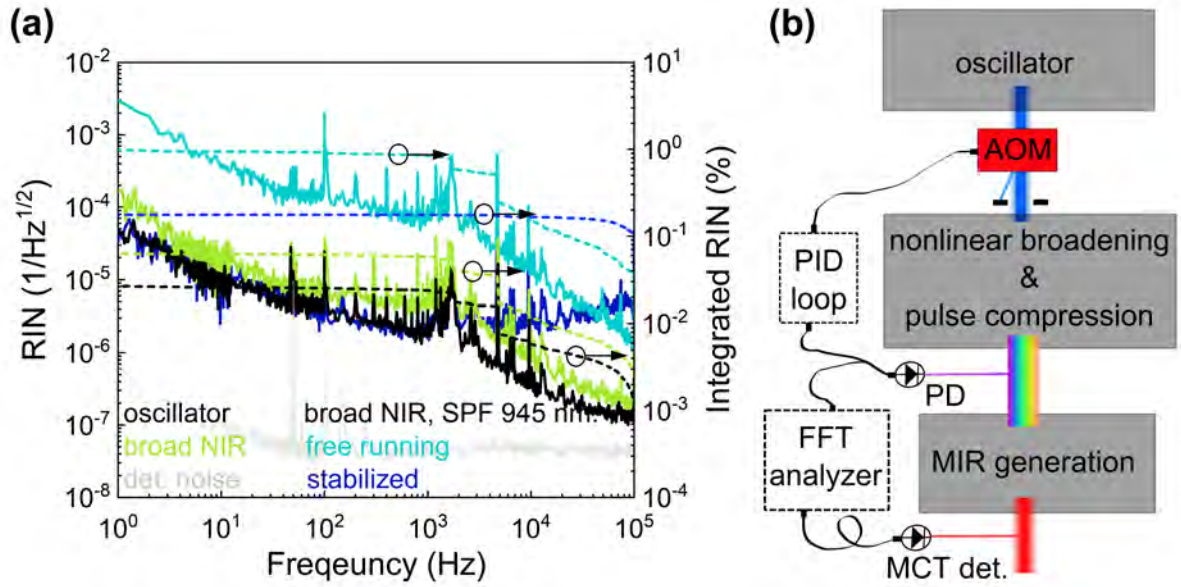


**Figure 3.6:** **a)** Measurement of the relative intensity noise (RIN) of the oscillator, the full broadened NIR spectrum, and the 945 nm short pass filtered (SPF) broadened NIR spectrum in the free running and the stabilized case. The dashed lines denote the integrated RIN correspondingly. **b)** Sketch of the active intensity noise suppression scheme: An acousto-optic modulator (AOM) in front of the nonlinear broadening stage modulates the input laser power. The RF power to the AOM is regulated with a PI<sup>2</sup>D controller. The signal of the blue part of the broadened NIR spectrum on a photodetector acts as error signal for the PI<sup>2</sup>D controller as well as for the in-loop diagnostic of the RIN.

mechanical resonances, respectively. The contributions between 1 kHz and 10 kHz could be traced back to the power supply of the pump diode.

The RIN after the nonlinear broadening stage (green) was analyzed accordingly by recording the transmission loss of the last dispersive mirror in the compression set with an amplified InGaAs-photodetector. The results were comparable to the oscillator RIN and the integrated RIN between 1 Hz and 100 kHz of 0.06 % was slightly increased owing to the long propagation length in the two MPCs. By inserting a 945 nm short pass filter (SPF) in front of the photodetector we characterized the RIN of the blue part of the broadened spectrum (cyan), i.e. the newly generated frequencies during SPM. Compared to the full broadened spectrum, the integrated RIN between 1 Hz and 100 kHz of 0.99 % was increased by a factor of 16.5. This wavelength dependent RIN can be explained by the amplification of amplitude noise upon nonlinear spectral broadening [64].

Because the generated MIR radiation originates mainly from nonlinear mixing between the wings of the broadened NIR spectrum, actively suppressing the fluctuations of the blue part of the broadened NIR spectrum can reduce the MIR RIN [65]. Fig.(3.6b) illustrates the concept applied for active noise suppression. An acousto-optic modulator (AOM) in front of the nonlinear broadening stage modulate the input laser power by diffracting up to

2 % of the power into higher orders. The diffraction efficiency of the AOM is proportional to the applied RF power which is regulated with a PI<sup>2</sup>D controller. The intensity fluctuations of the blue part of the broadened NIR spectrum measured with a photodetector act as error signal for the PI<sup>2</sup>D controller as well as for the in-loop diagnostic of the RIN. When this feed-back-loop was activated, the integrated RIN between 1 Hz and 100 kHz of the blue wing of the driving pulse reduced to 0.17 % which corresponds to a suppression factor of 6. As shown in Fig.(3.6a), the bandwidth of the active-feedback loop is limited to 50 kHz which is mainly attributed to the response time of the AOM.

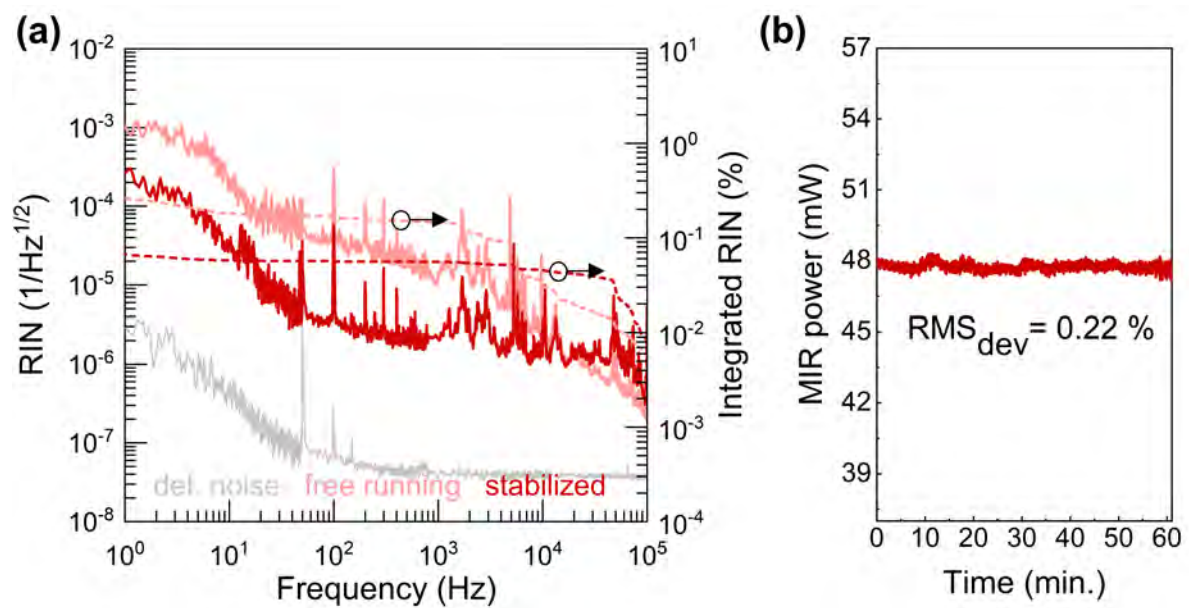


**Figure 3.7:** Characterization of the MIR stability. **a)** MIR RIN with and without active intensity stabilization of the generating NIR pulses. **b)** MIR power over one hour.

To prove that the described feedback-loop can reduce the MIR RIN, we measured the out-of loop MIR fluctuations with a liquid-nitrogen-cooled mercury cadmium telluride (MCT) photodetector. Fig.(3.7a) shows the results for the MIR RIN in the stabilized (red) and the free running (light red) case. When the active noise suppression was activated, the integrated RIN between 1 Hz and 100 kHz reduced from 0.36 % by a factor of 5 to 0.07%. This result shows that active intensity noise suppression in the MIR is possible without direct feedback and error signal in this spectral region. The long-term stability of the MIR radiation was observed with a thermal power meter by recording the full MIR power every 0.1 s over 1 hour. Fig.(3.7b) depicts the measured data with a root mean square deviation of 0.22 %.

### 3.3 Field-resolved detection with electro-optic sampling

In the field of broadband vibrational spectroscopy, the standard method of detection is FTIR spectrometry. In FTIR spectrometers, the broadband light source is coupled into an interferometer (mostly Michelson-type geometry). By delaying one interferometer arm with respect to the other, a delay-dependent interferogram is generated [13]. The Fourier transformation of this interferogram represents the power spectrum of the broadband light source and resolves the absorption features of a sample within the spectral coverage of the light source. When the sample is placed in only of the interferometer arms, an asymmetric interferogram is generated. This method allows to implement field-sensitive detection and record the absolute phase and amplitude of the sample response to the vibrational excitation [66, 67, 68]. However, this method has two major drawbacks. Firstly, it requires detection in the MIR spectral region where detectors have inferior noise figures. Secondly, its sensitivity and detector dynamic range is limited by the delay-independent, constant contribution of the incident light source to the interferogram (baseline). Electro-optic sampling mitigates both of these drawbacks by frequency up-conversion during nonlinear mixing with an ultrashort sampling pulse which simultaneously acts as temporal gating [36].

In the experiment, the EOS gate (i.e. sampling) pulses were split off the main beam before DFG using a 6-mm thick uncoated FS plate at a small angle of incidence (AOI). This permits independent adjustments on the DFG driving pulse and the EOS sampling pulse and avoids depolarization and pulse stretching in the LGS crystal. A sketch of the EOS setup is shown in Fig.(3.8). The divergent sampling beam was collimated with a plano-convex lens with 250 mm focal length to a 1.2 mm spot. To adjust the sampling power and clean the polarization, a combination of an achromatic HWP and a wire grid polarizer oriented along the vertical axis were employed. Two reflections off dispersive mirrors with  $-120 \text{ fs}^2$  GDD compensate for the transmissive elements in the sampling beam path. After travelling across a retroreflector mounted on a motorized translation stage the sampling pulses were recombined with the MIR waveforms utilising a 1-mm thick ZnSe plate which has a reflective coating for the NIR on the first surface and an AR coating for the MIR on the second surface.

The MIR waveforms passed through two additional foci after generation and recollimation. In the first focus, a mechanical chopper was placed to enable lock-in detection at up to 10 kHz. In the second focus, a sample cell can be introduced. As focusing and recollimating elements bare gold  $90^\circ$ -off-axis parabolas were used. Beam folding on six interchangeable mirrors was implemented to adjust the path length of the sampling pulse and the MIR waveform, i.e. to enable temporal overlap in the EOS crystal and to compress the MIR waveforms with dispersive mirrors. Before recombination in the ZnSe plate, the MIR waveforms passed through a  $3\text{-}\mu\text{m}$  long pass filter (LPF) to eliminate any residual radiation at  $1 \mu\text{m}$ .

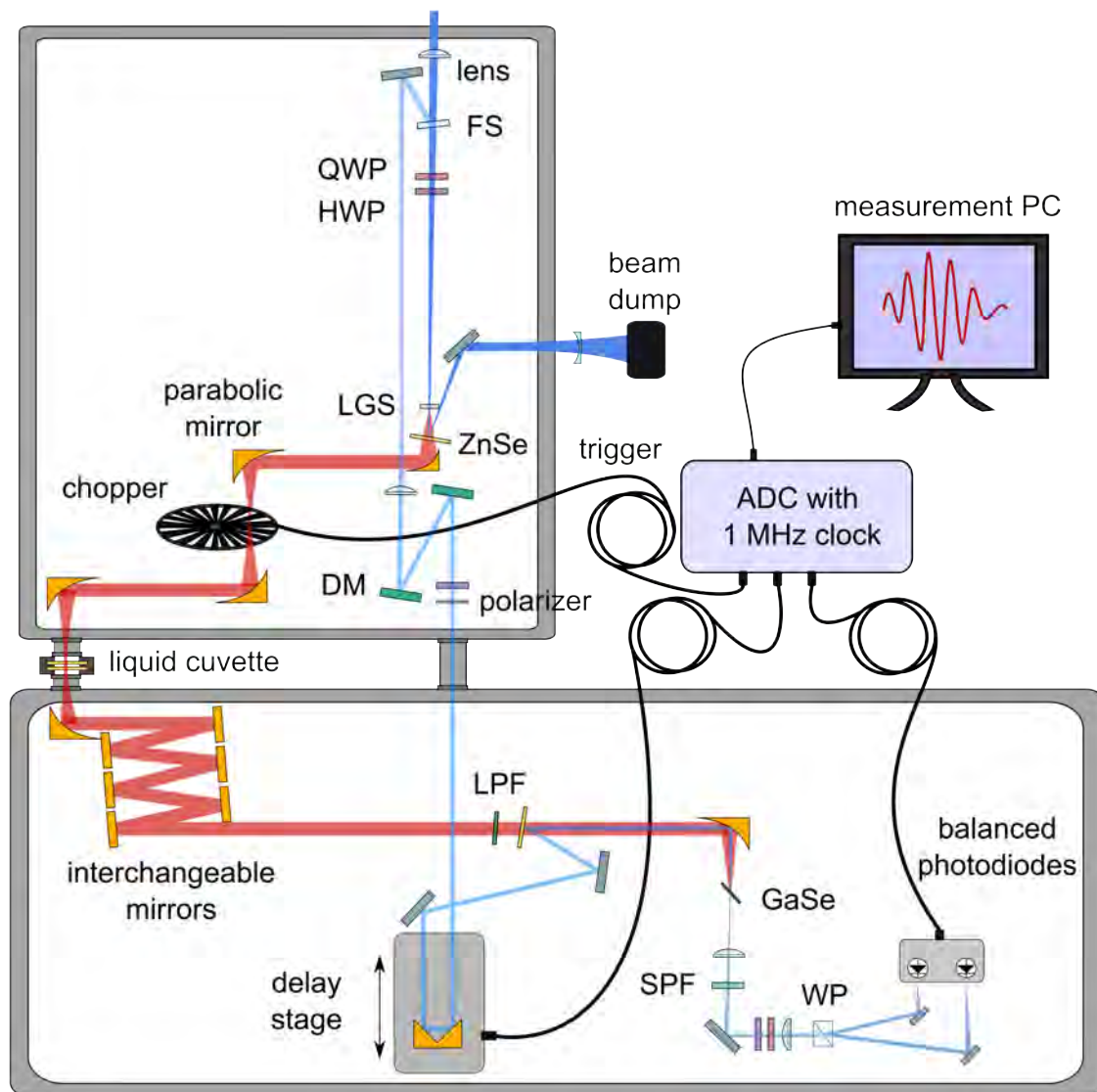


**Figure 3.8:** Sketch of MIR generation and electro-optic sampling detection. FS: fused silica, HWP: half waveplate, QWP: quarter waveplate, LGS:  $LiGaS_2$  crystal, ZnSe: dichroic mirror to split and recombine the MIR and the NIR beams, respectively, DM: dispersive mirror, ADC: analog-to-digital converter, LPF:  $3\ \mu\text{m}$  long pass filter, SPF:  $950\ \text{nm}$  short pass filter, GaSe: GaSe crystal, WP: Wollaston prism.

The collinear MIR and NIR beams were focused to a  $55\ \mu\text{m}$  or  $85\ \mu\text{m}$  thick GaSe crystal using a bare gold parabola with EFL of  $50.8\ \text{mm}$  where the nonlinear mixing takes place. The GaSe crystal was mounted in such a way that its  $z$ -position and its  $\theta$  and  $\phi$  angles can be controlled externally. After the EOS crystal the beam passed through a  $950\ \text{nm}$  SPF and a combination of QWP and HWP. A Wollaston prism split the power according to its polarization. The two outputs were focused onto a self-built balanced detector, consisting of two photodiodes followed by a low-noise current amplifier. The amplified signal was

recorded synchronously with a 24-bit analog-to-digital converter triggered by the chopping frequency for numerical lock-in detection. This combination of photodiodes, amplifier, and digitizer guarantees sufficient detection dynamic range to avoid limitations from detector noise and electronic noise.

### 3.3.1 Minimization of detection noise

The balanced nature of the EOS detection in theory allows to cancel any correlated technical noise in the sampling pulse up to the shot-noise limit [69]. However, it is experimentally increasingly challenging to reach the shot-noise limited regime for increasing sampling pulse power  $P_g$  because the shot noise scales with  $\sqrt{P_g}$  whereas the technical noise scales linearly with  $P_g$ . By selective spectral filtering after the nonlinear mixing process the power impinging on the detector and thus the technical noise is reduced stronger than the up-converted signal amplitude. Even in the shot-noise limited regime spectral filtering can improve the signal-to-noise ratio (SNR) [31]. Spectral filtering also allows to scale the sampling pulse power beyond the saturation threshold of the photodiodes, increasing the conversion quantum efficiency from the MIR to the NIR.

Fig.(3.9a) illustrates the idea of spectral filtering in the case of a phase matching configuration favoring SFG. The sum frequency spectrum generated by nonlinear mixing of the MIR radiation and the NIR sampling pulse in the EOS crystal is slightly blue-shifted with respect to the sampling pulse spectrum. However, only the region of spectral overlap between the sum frequency and the sampling pulse can contribute to the EOS signal. Therefore, a suitable short pass filter suppresses those frequency components of the sampling pulse which carry more technical noise than EOS signal.

In the experiment, a cut-off wavelength of 950 nm was found to maximize the SNR and to enable shot-noise dominated detection. In the absence of MIR radiation, the intensity on the two photodiodes of the differential detector was balanced by adjusting the orientation of the fast axis of a combination of QWP and HWP in front of the Wollaston prism.

Fig.(3.9b) shows the frequency-resolved noise of the balanced photodiode signal up to 12 kHz with and without active noise suppression. Also the noise of the balanced signal reduced with active noise suppression because the intensity noise of the sampling pulse was not perfectly cancelled. With the 950 nm SPF the average power on each diode was 280  $\mu$ W. The relative shot noise power  $S_q$  is given by [65]

$$S_q = \sqrt{\frac{2hc}{P\lambda}}, \quad (3.2)$$

where  $\lambda$  is the wavelength and  $P$  the average power of the impinging light source. At a chopping frequency of 7.5 kHz, the balanced noise was a factor of 1.9 above the relative shot noise when the active intensity noise suppression is activated. The performance of the balanced detection can in the future be improved by additional means to achieve a cleaner sampling pulse polarization. However, previous experiments in our group showed that the

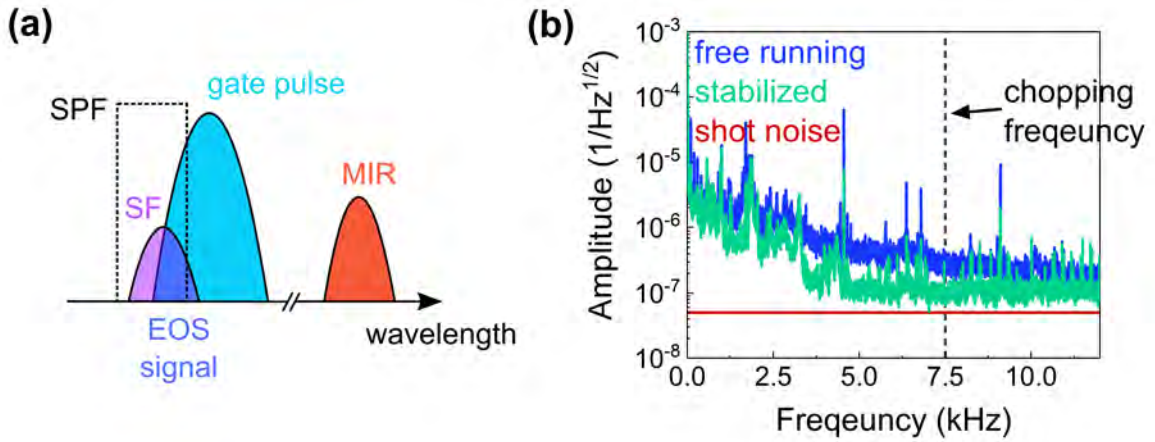


**Figure 3.9:** a) Schematic representation of spectral filtering after nonlinear up-conversion in EOS. Nonlinear mixing of the mid infrared (MIR) spectrum and the sampling pulse results in the sum frequency spectrum (SF). A short pass filter (SPF) suppresses the sampling pulse frequencies which do not contribute to the EOS signal. b) Frequency-resolved noise of the balanced sampling pulse signal with and without active intensity noise suppression and relative shot noise level corresponding to the average power on the detector.

RIN suppression for broadband balanced detection is limited to two to three orders of magnitude. Therefore, another strategy to reach the shot noise limit is to further reduce technical source noise.

### 3.3.2 Optimization of detection efficiency

As Eqn.(2.15) shows, the EOS signal scales with the MIR field strength and the sampling pulse intensity. The former is maximized by driving the MIR generation most efficiently and by minimizing losses in the MIR beam path. The latter is rather limited by the laser induced damage threshold of the GaSe crystal than by the available average power. Above 5 GW/cm<sup>2</sup> peak intensity, undesired nonlinear effects were observed which resulted in degradation of the crystal. Another limitation for boosting the sampling pulse average power is the imperfect cancellation of intensity noise at the balanced photodiode. Only in the regime where the EOS signal amplitude rises faster than the absolute noise, increasing the sampling pulse power enhances the SNR.

At constant sampling pulse power, the peak intensity can be increased by shrinking the beam size on the crystal and minimizing the pulse duration. With the 50.8 mm EFL parabolic mirror focusing onto the GaSe crystal we measured a sampling pulse focus spot size of 51  $\mu\text{m}$  (diameter at FWHM, see Fig.(3.10a)). To enable efficient SFG between the MIR and the sampling pulse, the spatial overlap of their foci should be maximized. Due to their large difference in wavelength and the resulting difference in diffraction limit, additional adjustments of the beam size on the focusing element are required for a good transverse mode matching. A magnifying telescope consisting of two 90°-off-axis parabolic

mirrors with 76.3 mm and 127 mm EFL, respectively was implemented to increase the MIR beam size and achieve a focal spot size of  $90\ \mu\text{m}$  instead of  $125\ \mu\text{m}$  (diameter at FWHM, see Fig.(3.10b), compared to the NIR beam profiler used for Fig.(3.10a) the MIR beam profiler has a lower resolution thus the MIR beam size seems smaller). Despite this improvement, there was still a significant discrepancy between the focal size of the MIR and the that of the sampling pulse. Further magnification of the MIR beam size however, was impractical because of the limited clear aperture of the optics which, in the extreme case, turns beam pointing fluctuations into intensity fluctuations.

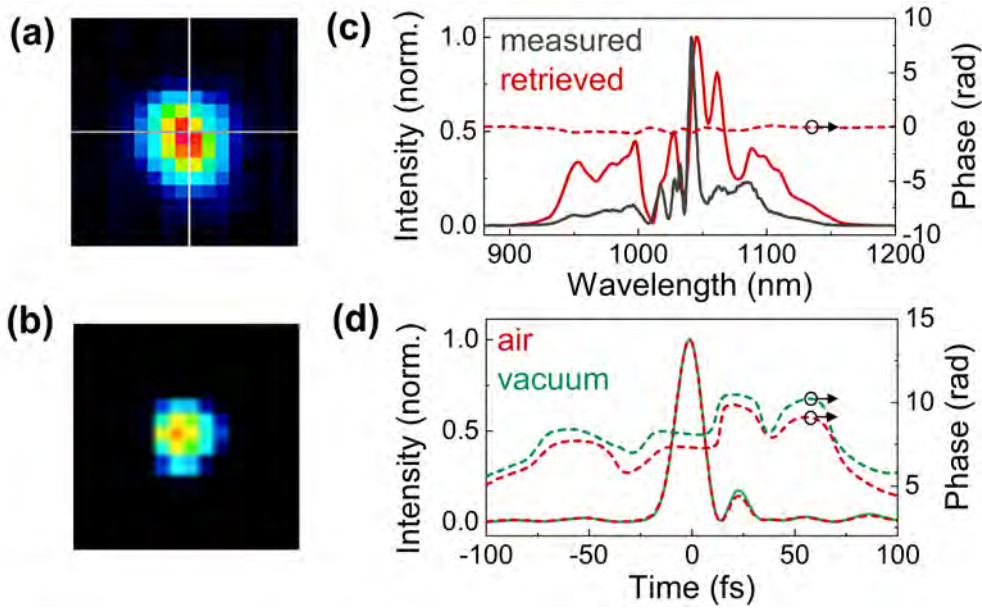


**Figure 3.10:** Beam profile of the sampling pulse focus (a) and the MIR focus (b). The reduced resolution of the MIR beam profiler makes the  $90\ \mu\text{m}$  MIR focus appear smaller than the  $51\ \mu\text{m}$  sampling pulse focus in this illustration. SHG-FROG measurement of the sampling pulse before EOS: c) Measured and retrieved spectrum and spectral phase. d) Retrieved temporal intensity profile of the sampling pulse in air and in vacuum. To compensate the missing dispersion in vacuum 2 mm FS were added.

The other option, to build a demagnifying telescope for the sampling pulse, has so far not been realized because of the limited sampling pulse power. In the current configuration, the sampling pulse power can be continuously increased with an attenuator up to 750 mW. To keep the peak intensity constant for decreasing focus spot size, the power has to rise with the square of the demagnification factor which is only possible for up to 240 mW of initial power. This is far below the damage threshold of the GaSe crystal. Another consideration is the imperfect balanced detection which complicates reaching the shot-noise dominated regime for increased sampling pulse powers.

Ideally, in an EOS setup the focal spot size of the sampling pulse would be larger than the MIR focal spot size to avoid transformation of uncorrelated beam pointing fluctuations into intensity fluctuations whereas the sampling pulse power would be scaled accordingly

up to the damage threshold of the EOS crystal. However, this optimization requires Watt-range power scalability of the sampling pulse and therefore goes beyond the scope of this thesis.

The sampling pulse duration is not only critical for increasing the peak intensity and, thus, maximizing the efficiency of SFG, but determines the lower wavelength limit for EOS detection. To guarantee the shortest achievable pulse duration we performed a SHG-FROG measurement of the sampling pulse after the recombining ZnSe plate. The results are shown in Fig.(3.10c) and (d). The measured and retrieved spectra agree well with the spectrum of the driving pulse. In ambient air, a FWHM pulse duration of 15 fs was measured which is very close to the FT limited pulse duration of 14 fs calculated for the driving pulse spectrum, see Section 3.1.2. As the EOS detection and the IPDFG are operated under vacuum conditions during experiments, the FROG measurement was repeated at  $7 \times 10^{-3}$  mbar. The dispersion change due to the reduced pressure was compensated by adding 2 mm of FS in the sampling pulse beam path resulting in a very similar temporal pulse shape as compared to the measurement in ambient air, see Fig.(3.10d).

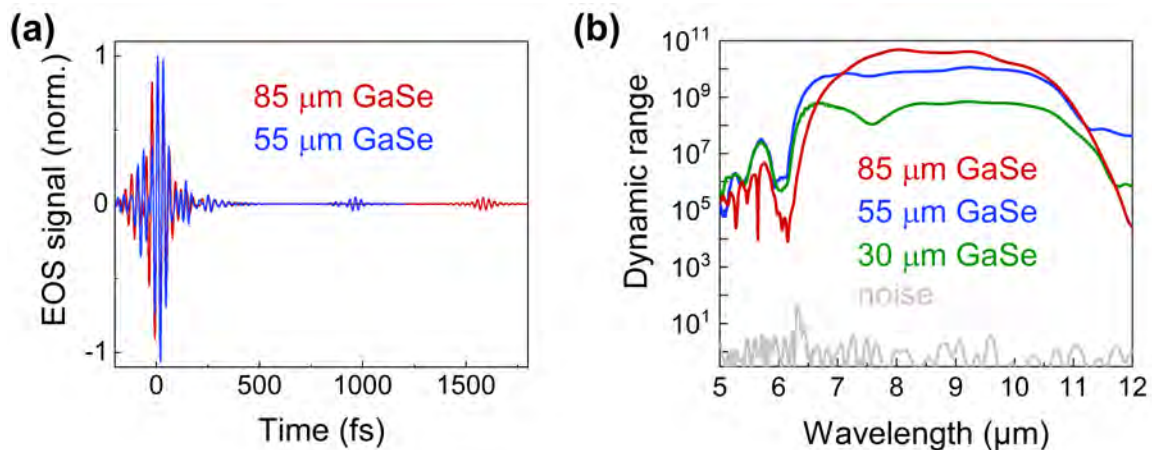


**Figure 3.11:** **a)** Measured EOS traces for two different detection crystals averaged over 10 scans. **b)** Fourier transformation of the EOS traces reveals the intensity spectra for three different detection crystals. The spectra are normalized to the respective detection noise floor resulting in the spectrally resolved dynamic range.

With a sampling pulse power of 350 mW and a scan speed of 0.25 mm/s we recorded EOS traces for three different GaSe crystals. Fig.(3.11a) shows the measured signals for a 85  $\mu$ , a 55  $\mu$ , and 30  $\mu$  thick GaSe crystal averaged over ten consecutive scans. For better comparability, the EOS traces were normalized. The FWHM pulse duration was 50 fs for the 55  $\mu$  thick GaSe crystal and 65 fs for the 85  $\mu$  thick GaSe crystal. To obtain the intensity spectra depicted in Fig.(3.11b) the EOS traces were Fourier transformed. For each crystal configuration ten noise traces outside the temporal overlap of the MIR and the sampling pulse were recorded and averaged to define the detection noise floor. The spectrally resolved dynamic range (DR) for each configuration is the intensity spectrum

divided by the measurement noise floor. For the thickest crystal, a peak DR of almost 11 orders of magnitude was achieved within a measurement time of 45 s and a nominal resolution of  $4 \text{ cm}^{-1}$  which is compatible with previous results [36].

All measurements included a  $30 \text{ }\mu\text{m}$  thick liquid cell filled with water which reduced the DR by one order of magnitude due to the strong absorption of liquid water within the spectral coverage of the instrument. Fig.(3.11b) illustrates the trade-off between spectral bandwidth and efficiency for the nonlinear mixing process involved in the EOS detection. A thicker GaSe crystal increased the SFG efficiency but reduced the phase matching bandwidth. At first glance, only the DR for the  $30 \text{ }\mu\text{m}$  thick GaSe crystal reduced. However, the spectral components below  $6 \text{ }\mu\text{m}$  were increased relatively compared to the  $55 \text{ }\mu\text{m}$  thick crystal. In comparison to the green spectrum in Fig.(3.5c) measured with the FTIR spectrometer, the spectrum detected with EOS was flat which is a consequence of phase matching and spectral filtering.

In order to decide for one detection configuration, the actual application has to be considered. For certain samples, a broader spectral coverage at short wavelengths might reveal more information than a higher sensitivity at the central wavelength. Another aspect is the post pulse shown in Fig.(3.11a) after 950 fs and 1590 fs, respectively stemming from the internal reflection of the MIR pulse inside the GaSe crystal. It can hinder from reaching the detection noise floor in a potentially interesting temporal window. In this regard, several approaches like contacting the GaSe crystal to a thicker medium with equal refractive index or using a different type of detection crystal have been proposed but not successfully implemented up to now.

### 3.3.3 Interferometric delay tracking

Besides the optical DR of a spectroscopic instrument, which is determined by the detection efficiency and the detection noise floor, in time-domain spectroscopy the precision of the delay read-out is crucial for the performance [70]. The precision of the internal linear encoder of commercial mechanical delay stages is typically limited to  $\sim 20 \text{ nm}$ . With the help of Michelson-type interferometers the movement of the delay stage can be tracked with higher accuracy [71]. However, air flow turbulences especially introduced by the mechanical chopper and acoustic vibrations of optomechanic elements including the delay stage itself can lead to additional fluctuations of the optical delay between the MIR and the sampling pulse. The interference pattern of a copropagating frequency stabilized CW laser can be utilized for real-time correction of these fluctuations as well as for the precise measurement of the stage movement [72].

To this end, we used a commercial system for interferometric position measurements (Smaract, Picoscale) which was adapted for the use in a Mach-Zehnder-type setup by my colleagues Wolfgang Schweinberger and Lenard Vamos in collaboration with the manufacturer [72]. The commercial system is equipped with a distributed-feedback laser diode emitting a  $1.55\text{-}\mu\text{m}$  wavelength CW beam with  $140 \text{ }\mu\text{W}$  of output power. By interfering the emitted CW beam with the reflected beam from a mirror fixed to a moving object in a

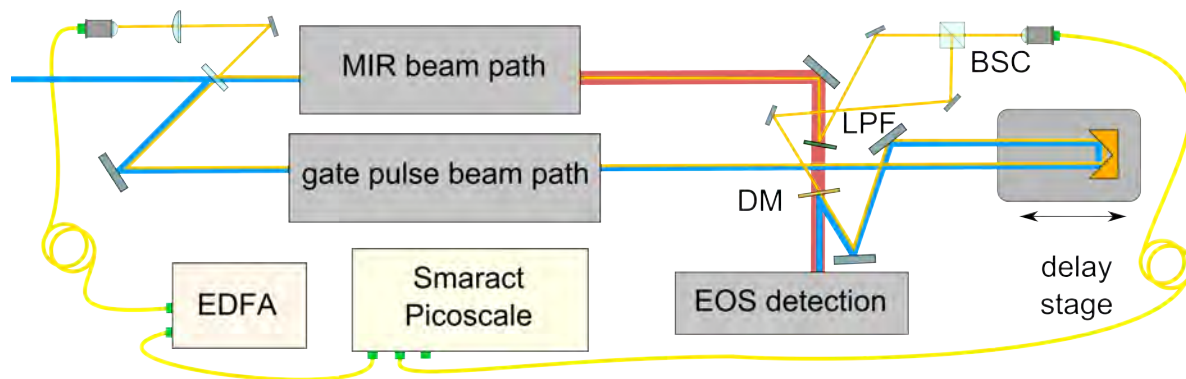


**Figure 3.12:** Sketch of the interferometer utilized for delay tracking. The CW laser output of a commercial interferometric position sensor (Smaract Picoscale) is amplified in an erbium-doped fiber amplifier (EDFA) and copropagates with the MIR waveform and the sampling pulse. After recombination the interference signal is decoded in the Picoscale device for delay tracking. DM: dichroic beam combiner, LPF: 3  $\mu\text{m}$  long pass filter, BSC: beam splitter cube.

Michelson-type sensor head, a phase sensitive signal was generated. To detect the direction of the movement and increase the position sensitivity, the wavelength of the laser diode was modulated at 30 MHz and the interference signal was demodulated at the fundamental and the second harmonic of the modulation frequency.

The interferometric configuration used in this work is shown in Fig.(3.12). For application in a Mach-Zehnder-type, few meter long interferometer, the fiber-coupled laser output was boosted to up to 120 mW using a commercial Erbium-doped fiber amplifier. With a single-mode fiber, the amplifier output was guided to the Infrsampler setup where it was collimated for free-space use. From the backside, the CW beam was sent to the FS plate used for splitting off the EOS sampling pulse such that the transmitted part co-propagated with the sampling pulse and the reflected part with the MIR waveforms. A plano-convex lens with 500 mm focal length was used to compensate for the focusing elements in the sampling pulse and MIR beam path and to obtain a collimated CW beam thereafter. At the ZnSe plate used for recombining the sampling pulse and the MIR waveform, the CW beam from the sampling pulse arm was transmitted. The CW beam from the MIR arm however, was reflected by the LPF in front of the ZnSe plate. With a beam splitter cube both parts of the CW beam were overlapped and their interfering light was coupled into a single-mode fiber. The other end of the fiber was connected to the commercial device where the interference signal was demodulated and the position information was decoded.

The chopper in the MIR beam path periodically interrupted the position signal. Therefore the acquisition of the position signal was triggered with the chopping frequency and the chopper phase was adjusted to maximize the recorded signal. Both the position signal and the EOS signal were digitized with an ADC whose channels are internally synchronized to a 1-MHz reference clock. In this way, the interferometric method allows to precisely track the actual delay between sampling pulse and MIR waveform and to record EOS

traces which are inherently corrected for delay variations introduced by air fluctuations or mechanical instabilities.

In the future, the performance of interferometric delay tracking (IDT) will be further improved by a beam splitter and combiner designed for the operating wavelength of 1.55  $\mu\text{m}$ . A better balanced splitting ratio will increase the SNR of the position signal. Ideally, the recombination of the CW beams will happen at the same optic as the recombination of sampling pulse and MIR waveform to minimize uncorrelated interferometer length fluctuations.

### 3.4 Background-free measurement of molecular vibrations

Besides accessing the absolute phase and amplitude information of the electric field of light, the main advantage of electro-optic-sampling-based detection is its ability to record radiation emitted by resonantly excited molecules in a quasi background-free manner. When a broadband MIR waveform hits the molecules inside a sample, it excites resonant vibrational modes. The induced ensemble of coherently oscillating dipoles in the sample emits radiation in the same spatial mode as the excitation. In the intensity spectrum recorded by conventional time-integrating, frequency-domain spectroscopies, the destructive interference of the exciting electric field with the phase-shifted, coherent electric field emitted by the molecules is detected as an absorption dip at the resonance frequency [33].

In field-resolved spectroscopy employing few-cycle excitation, this resonant response of the molecules appears in the wake of the excitation. Due to the narrow bandwidth of the excited resonances, the coherent emission lasts much longer compared to the duration of the MIR excitation - for samples in the liquid phase up to several picoseconds and for samples in the gas phase up to a few nanoseconds. This difference in decay time between the excitation pulse and the interrogated sample opens up a time window of background-free resonant molecular response. The nonlinear gating involved in the EOS process also enables the detection of the resonant molecular response in this time window in a quasi background-free manner by filtering any contribution outside the temporal overlap of the sampling pulse and the MIR radiation. The detection sensitivity is thus in principle limited by the up-conversion efficiency and the shot noise of the sampling pulse.

In a real world measurement however, not only molecules inside the sample give rise to a resonant response but almost any kind of molecule the MIR waveform encounters on its way to the EOS crystal constitutes a molecular background signal - most prominently water vapor. To eliminate the molecular background signal, we evacuated the system from the MIR generation downstream and run our measurements at a pressures of  $1 \times 10^{-3}$  mbar.

In order to extend the window of background-free resonant sample response, we designed dispersive mirrors for the MIR waveform to compress the excitation pulse to its FTL and optimized its temporal roll-off.

### 3.4.1 Elimination of water vapor background

The design of an evacuated experiment requires a considerable amount of engineering. To control all critical parameters like crystal angles, crystal positions, and fast axis orientation of wave plates under vacuum conditions, the corresponding mounts were equipped with mechanical feed-throughs or step motors. The vacuum chambers were designed such that the optical breadboard inside the chamber is decoupled from the chamber housing using mechanical bellows. This renders the optical components largely immune to vibrations outside the vacuum chamber and avoids distortions upon evacuation leading to misalignment. Additionally, two motorized mirror mounts were included in the MIR and the NIR beam path, respectively to optimize the spatial overlap in the EOS crystal at the end pressure.

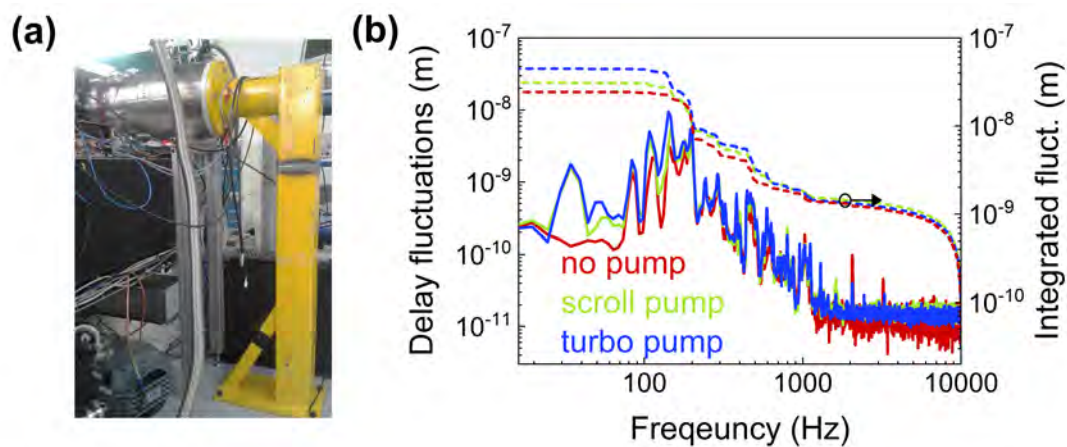


**Figure 3.13:** Isolation of turbopump vibrations. **a)** The turbopump is connected to the vacuum chamber using a dampening bellow and a supporting arm. **b)** Frequency resolved delay fluctuations between MIR and sampling pulse measured with IDT.

Despite the described measures, operation of a turbo molecular pump connected to a side wall of the vacuum chambers resulted in increased mechanical vibrations of the optical components. Inserting a dampening bellow between the chamber wall and the turbo pump in combination with a L-shaped supporting arm as shown in the picture in Fig.(3.13a) reduced the influence of the turbo pump. A scroll pump was connected to the turbo pump to reach the initial operation pressure of the turbo pump of 1 mbar and to suck off its exhaust. At the maximum rotation speed of 630 Hz a minimal pressure of  $8 \times 10^{-4}$  mbar was reached after five hours of constant operation. In day-to-day operation, the pressure was  $1 \times 10^{-3}$  mbar. Fig.(3.13b) shows a frequency resolved measurement of the delay fluctuations between the MIR and the sampling pulse recorded with IDT. Above 1 kHz the delay fluctuations were constant given by the IDT-precision of a few pm. When no pump was running the root mean square value of the integrated delay fluctuations between 1 Hz and 10 kHz was 24 nm. When only the scroll pump was running this value increased to 32 nm due to a dominant fluctuation peak at 30 Hz caused by mechanical resonances. Additional operation of the turbo pump led to a very similar delay fluctua-

tion spectrum and a slight increase of the root mean square value of the integrated delay fluctuations to 44 nm. Delay fluctuations of this order of magnitude can still be well corrected for by IDT. Thus, a stable operation at pressures as low as  $1 \times 10^{-3}$  mbar is possible.

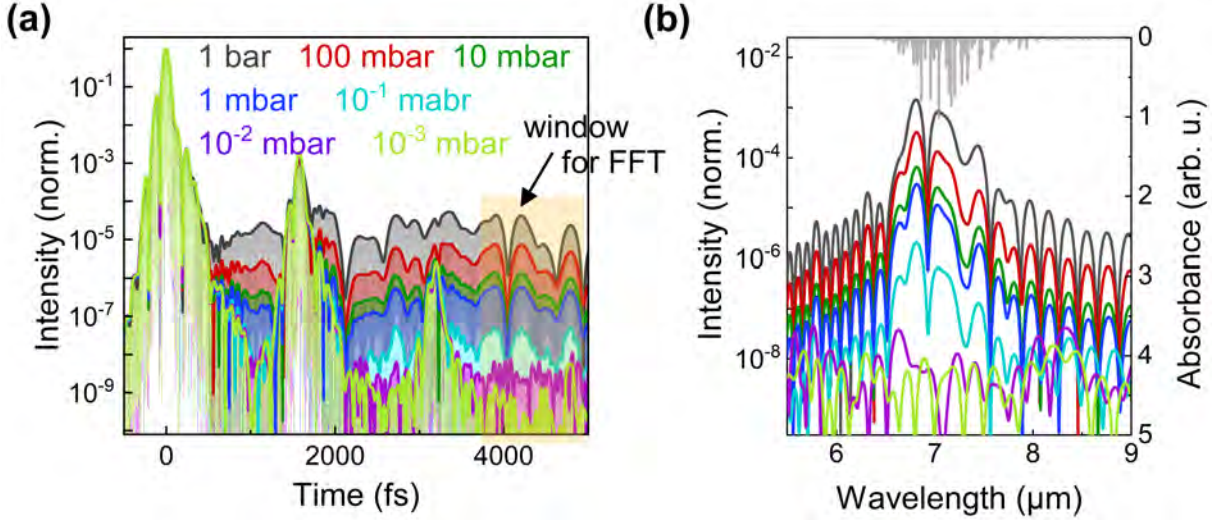


**Figure 3.14:** Molecular background caused by water vapor absorptions for decreasing pressure in the time domain (a) and the frequency domain (b). The orange area indicates the time window for which the Fourier transformation is shown in (b). For comparison the absorbance spectrum of water vapor multiplied with the spectral coverage of the excitation pulse is depicted in grey.

To prove that a working pressure of  $1 \times 10^{-3}$  mbar is sufficient to eliminate the molecular background, we studied the pressure dependence of the coherent emission of molecules in the laboratory air. First, we measured an EOS trace of the MIR excitation pulse at ambient pressure. After reducing the pressure by one order of magnitude, we repeatedly recorded the same measurement until the working pressure of  $1 \times 10^{-3}$  was reached. Fig.(3.14a) shows the normalized intensity calculated from the seven EOS traces at different pressure for a time window of 5 ps after the excitation pulse. The peaks after 1.6 ps and 3.2 ps are copies of the excitation pulse caused by the first and the second internal reflection from the detection crystal, respectively. At pressures above 0.1 mbar the second internal reflection drowns in the molecular background. Over the shown time period of 5 ps the intensity of the radiation which is coherently re-emitted by the background molecules was at a constant level for each pressure, in accordance the expected slow temporal decay on the nanosecond time scale typical for gas phase molecules. For decreasing pressure, the exponential decay of the excitation pulse was gradually revealed. However, the trailing edge of the main pulse coincided with the leading edge of the first internal reflection before the noise floor was reached for the given detection crystal thickness (55  $\mu\text{m}$ ).

To allocate the coherently re-emitted radiation to specific absorbance features of certain molecules it is instructive to study the signal in the frequency domain. By choosing the

time window between 3.8 ps and 5 ps for the Fourier transformation, any contribution of the excitation pulse was filtered out and Fig.(3.14b) directly reveals the spectrum of the coherently oscillating molecular dipoles. The narrow time window chosen for the Fourier transformation however, limited the spectral resolution such that only broad absorption features instead of distinct absorption lines - as expected for molecules in the gas phase - appear. For comparison, the absorbance spectrum of water vapor multiplied by the spectral coverage of the excitation pulse in vacuum is depicted in grey. The shape and the frequency of the molecular background spectrum agree with the absorbance of water vapor which indicates that the molecular background mainly comprises water molecules in the gas phase. The intensity of the molecular background signal does not scale linearly with the pressure, implying that the concentration of water molecules is not proportional to the absolute number of molecules. For pressures above 1 mbar, the concentration of water molecules decreases slower than the pressure whereas for pressures below 1 mbar the concentration of water molecules decreases faster. At the working pressure of  $10^{-3}$  mbar no distinct absorption features can be distinguished from the measurement noise floor, indicating that at this pressure all molecular background was eliminated down to the sampling pulse shot-noise-dominated detection noise floor.

### 3.4.2 Temporal confinement of the exciting light pulses

The ability of a time-domain spectrometer to detect small concentrations of molecules increases with the window of background-free detection opening up closer to the excitation peak. A quantitative description of the minimum detectable absorbance  $MDA$  can be derived from time-domain modelling of a molecular system with a single isolated Lorentzian oscillator with dephasing time  $T_L$  [36]:

$$MDA = \frac{2}{DR} \exp\left(\frac{t_B}{T_L}\right). \quad (3.3)$$

The dynamic range  $DR$  is defined as the ratio of maximum spectral amplitude of the electric field at the center frequency of the Lorentzian oscillator and the detection noise floor. For a given excitation pulse,  $t_B$  is the time after the peak of the excitation pulse where the difference of two consecutive EOS traces reaches the detection noise floor. Eqn.(3.3) illustrates that especially for short decay times on the picosecond time scale, as encountered in the liquid phase,  $t_B$  strongly influences the minimum detectable absorbance.

To minimize  $t_B$  and therefore to optimize the minimum detectable absorbance, we designed specific dispersive mirrors aiming at compensating the dispersion carried by the MIR waveforms. The EOS detection directly reveals the absolute phase information of the latter. However, it also convolutes its electric field with a frequency-dependent response function. At this point, it is important to note that we do not intend to compress the electric field of the MIR waveform but the measured quantity, i.e. the EOS signal. Thus, it is justified to derive the relevant phase information directly from the EOS signal without calculating the actual electric field.

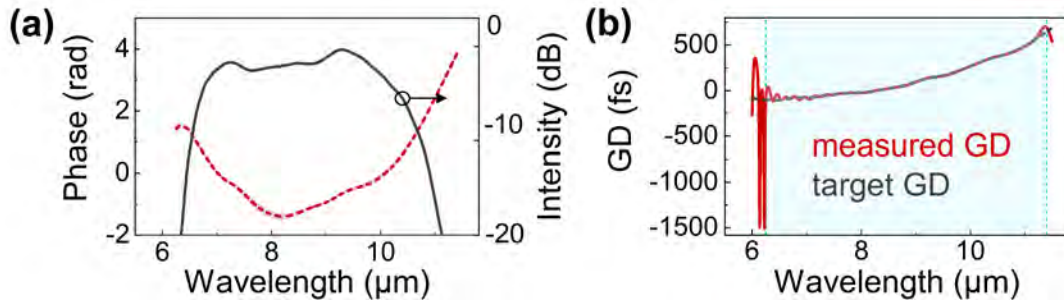


**Figure 3.15:** **a)** Mean value of the spectral phase of the MIR waveform for four different EOS measurements distributed over two weeks. The shaded grey area denotes the standard deviation. For comparison, the spectrum of the MIR waveform is shown in black. **b)** Group delay and fitted target curve for dispersive mirror design. The shaded blue area denotes the spectral coverage at a -20 dB level.

Fig.(3.15a) shows the mean value of the spectral phase for four different measurements distributed over two weeks. The shaded grey area denotes the standard deviation of the four measurements which is on average 3%. For comparison, the spectral coverage up to a -20 dB level is shown in black. The bandwidth of the dispersive mirrors was restricted to the spectral coverage at a -20 dB level from 6.2  $\mu\text{m}$  to 11.4  $\mu\text{m}$ . The first derivative of the spectral phase with respect to the angular frequency reveals the group delay in Fig.(3.15b). Outside the defined spectral coverage (blue shaded area) the GD exhibits strong variations. To calculate a design target for the dispersive mirrors the experimental curve was smoothed using a polynomial fit of 6th order (black dashed line). For the actual design target GD, the sign was flipped such that the spectral phase after reflection off the dispersive mirrors is flat. The target curve shows a GD variation of 750 fs within the defined spectral region which amounts to the dispersion accumulated in the generating LGS crystal and 4 mm ZnSe.

It is technically challenging to produce mirror coatings compensating for a GD variation as large as 750 fs over almost one spectral octave in the MIR range. To avoid very thin and very thick coating layers which could lead to mechanical stress or peeling of the multi-layer coating, the necessary GD was distributed over 6 reflections off identical dispersive mirrors. Comparable to the coating design discussed in [73], a stack of 11 alternating layers of Ge and  $\text{YbF}_3$  was calculated to achieve the best compromise between reflectivity and agreement with the target GD. The required layer sequence could successfully be coated onto 1-mm thick ZnSe substrates.<sup>1</sup>

Six gold mirrors under small AOI in the MIR beam path were substituted by dispersive mirrors. The AOI on the dispersive mirrors was kept below  $15^\circ$ . The wave front of the MIR beam was affected by the dispersive mirrors leading to an elliptical beam profile and a shift of the focal plane in the EOS crystal. This finding indicates a curvature of the mirror

<sup>1</sup>The mirror coating design and fabrication was performed by Tatiana Amotchkina from the LMU internal coating facilities, led by Vladimir Pervak.

substrates induced by mechanical stress. To compensate for the unwanted curvature of the dispersive mirrors the position and the alignment of the parabolic mirror in front of the MIR compressor was adjusted. Future coatings will be deposited on thicker substrates to avoid bending.

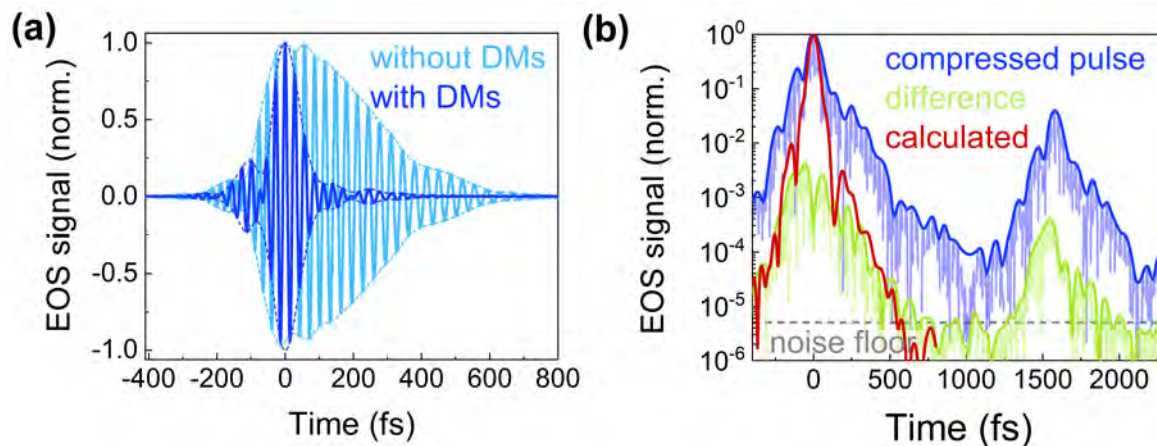


**Figure 3.16:** Compression of the mid infrared waveform. **a)** EOS trace of the MIR pulse with and without 6 reflections off dispersive mirrors. **b)** EOS trace of the compressed MIR pulse on a logarithmic scale. The difference of two EOS measurements reaches the noise floor 600 fs after the excitation peak. For comparison, the calculated exponential roll-off is shown in red.

Fig.(3.16a) shows the EOS trace measured before and after inserting the dispersive mirrors. The FWHM of the electric field envelope of the MIR waveform was compressed from 350 fs to 65 fs. At a central wavelength of 8  $\mu\text{m}$  this pulse duration corresponds to less than three cycles of the electric field. However, the considerable post pulse hinders a fast roll-off as illustrated in Fig.(3.16b). By subtracting the target GD curve from the measured GD curve, we calculated the expected spectral phase of the MIR pulse after six reflections off the dispersive mirrors. Together with the measured MIR spectrum this allows to estimate the expected MIR field in the time-domain. The calculated FWHM duration of 59 fs is close to the measured 65 fs but the calculated field envelope decays much faster than the measured one as Fig.(3.16b) shows. To estimate  $t_B$  we subtracted two consecutive EOS measurements. The difference trace reaches the measurement noise floor 600 fs after the peak of the MIR waveform. Assuming the same suppression factor between subsequent measurements, the calculated field envelope promises a  $t_B$  of 250 fs.

The discrepancy between the measured and calculated temporal roll-off can have manifold reasons. The restriction of the spectral bandwidth of the dispersive mirrors to the spectral coverage at a -20 dB level and the suppression of wavelength components outside this spectral region by a reduced reflectivity might be an insufficient approach to achieve a fast temporal roll-off on a logarithmic scale. Flattening of the measured GD curve in order to obtain a less complicated target design might cause artefacts visible on a logarithmic scale.

Despite the deviation from the calculated temporal roll-off, the compression of the MIR waveforms with the dispersive mirrors opens up the possibility for background-free measurements starting 600 fs after the peak of the waveform. In the future, several coating iterations and a thorough investigation of the described factors will lead to a roll-off optimized mirror design.

## 3.5 Benchmarking of the spectrometer

As discussed in the previous section, electric-field-resolved spectroscopy enables the quasi-background free detection of molecular signals harnessing temporal separation and nonlinear gating. To evaluate this conceptual advantage towards the workhorse in the field of MIR spectroscopy, i.e. a commercial, state-of-the-art FTIR spectrometer, we conducted a benchmarking measurement campaign. The figure of merit for this comparison is the smallest detectable concentration of methylsulfonylmethane ( $\text{DMSO}_2$ ) solved in water, permitting direct comparison with the previous record-sensitivity achieved within our group [36]. The study followed the measurement protocol established in [36] to allow comparability to the state-of-the-art electric-field resolving spectrometer as well as to a research-grade FTIR spectrometer presented therein. After optimizing the dynamic range of the EOS detection and the compression of the MIR excitation pulse the measurement campaign was repeated.

### 3.5.1 Determination of the limit of detection

Due to the temporal confinement of the excitation pulse and the comparably slow decay of the molecular ring-down, FRS can directly measure the coherent electric field emitted by resonantly oscillating dipoles. An exemplary FRS measurement of 1 mg/ml  $\text{DMSO}_2$  molecules solved in water is shown in Fig.(3.17a). To this end, the MIR excitation pulse propagates through a 30  $\mu\text{m}$  thick liquid cuvette filled with  $\text{DMSO}_2$  solution and the instantaneous as well as the resonant response of the sample is detected with EOS. Afterwards, the liquid cuvette is flushed with water and a reference EOS trace of pure water is recorded. At full scale, the EOS trace of sample and reference look identical but a close-up of the time window between 600 fs and 1200 fs reveals the differences between the two measurements. In this time window, the reference measurement has decayed and the coherent electric field of the resonantly oscillating dipoles of the  $\text{DMSO}_2$  molecules only present in the sample measurement dominates.

The numerical difference between the sample and the reference EOS traces shown in Fig.(3.17b) isolates the resonant response of the  $\text{DMSO}_2$  molecules. However, depending on the amplitude of the resonant response, i.e. the concentration of the specific molecule, the imperfect suppression of the excitation pulse due to intensity and phase fluctuations covers the molecular signal. The exponential decay of the molecular signal originates from the dephasing time of vibrational excitations in the liquid phase on the order of a few ps. The periodic

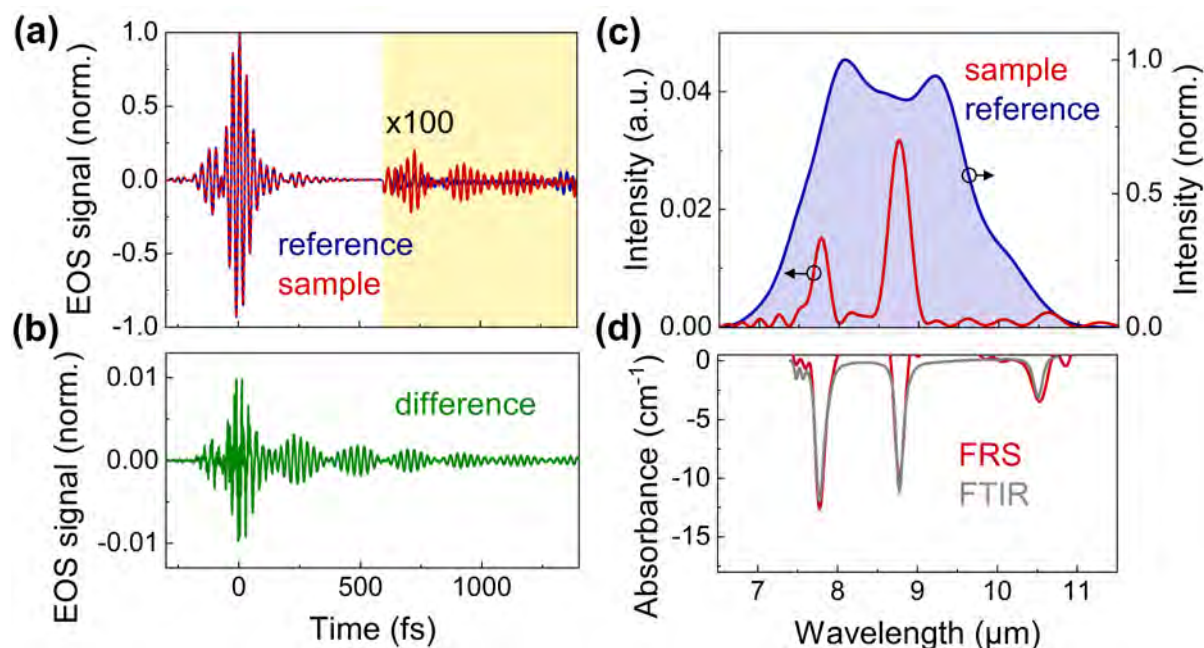


**Figure 3.17:** Field resolved measurements of 1 mg/ml DMSO<sub>2</sub> solved in water. **a)** Comparison of the EOS trace of the MIR waveform after transmission through water (blue line) and DMSO<sub>2</sub> solved in water (red line). The time window (600 fs - 1200 fs) where the resonant response of the DMSO<sub>2</sub> molecules dominates is scaled in amplitude by a factor of 100. **b)** Difference of the two EOS traces shown in (a). The numerically isolated resonant response of the DMSO<sub>2</sub> molecules decays exponentially. The beating indicates a superposition of the two dominant resonant features of the molecule. **c)** Fourier transformation of the MIR pulse transmitted through DMSO<sub>2</sub> solved in water for the temporal window indicated in (a). For reference the spectral coverage of the excitation pulse, i.e. the Fourier transformation of the MIR pulse transmitted through water is shown. **d)** Absorbance of DMSO<sub>2</sub> calculated from the Fourier transformation of the entire EOS traces shown in (a). The grey line depicts a reference based on measurements with a commercial FTIR spectrometer.

amplitude modulation indicates the beating of two dominant vibrational resonances within the spectral coverage of the excitation pulse. This assumption is corroborated by the Fourier transformation of the sample EOS trace depicted in Fig.(3.17c). To isolate the resonant molecular response, the time trace was truncated at 600 fs and 1200 fs before the Fourier transformation. The spectrum of the resonant response of the DMSO<sub>2</sub> molecules has two major peaks at 7.78  $\mu\text{m}$  and 8.75  $\mu\text{m}$ . As a reference for the spectral coverage of the excitation pulse the Fourier transformation of the reference EOS trace is shown in blue.

Fig.(3.17d) depicts the absorption coefficient calculated according to Beer's law based on the spectra of sample and reference without time domain filtering. The absorption coefficient measured with a commercial FTIR spectrometer with identical spectral resolution

is in good agreement with the absorption coefficient determined with the FRS method and verifies the quantitative conformity of the two methods.

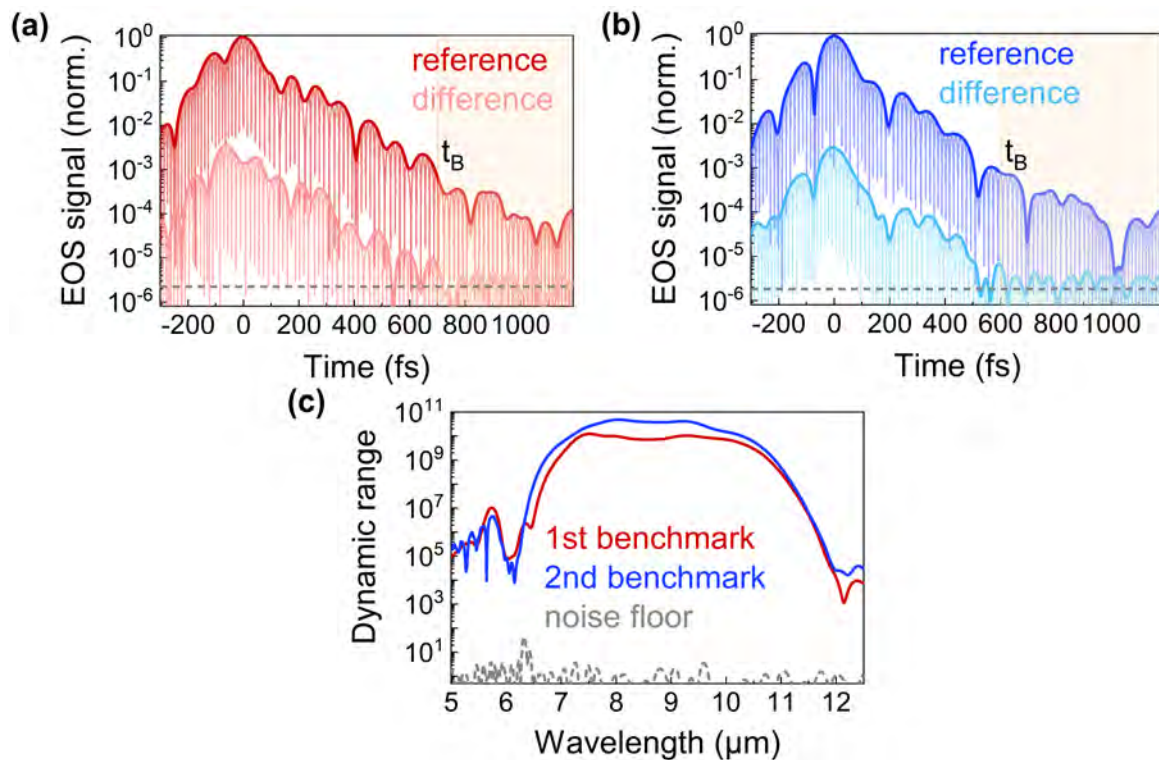


**Figure 3.18:** Measurement settings for benchmarking with  $\text{DMSO}_2$ . Reference measurement and difference of two reference measurements indicating that the time window for background free detection opens up at  $t_B = 700$  fs in the first measurement series (a) and at  $t_B = 600$  fs in the second measurement series (b). The dashed grey line denotes the measurement noise floor. c) Spectrally resolved dynamic range for the first and the second benchmarking measurement.

To determine the limit of detection of the developed FRS instrument we repeatedly measured a dilution series of 0.1, 1, 3, 10, 30, 100, 300, and 1000  $\mu\text{g}/\text{ml}$   $\text{DMSO}_2$  solved in pure water. The nominal spectral resolution was  $4 \text{ cm}^{-1}$  and the measurement time was 45 s, over which 12 scans were averaged for each measurement. For every concentration at least six measurements were taken, each followed by a reference measurement of pure water. These parameters grant comparability of the results to the study presented in [36]. The liquid cuvette employed for sample handling is adapted from a commercial microfluidic system (Microbiolytics GmbH) for automated sample exchange and intermediate cleaning. The cuvette consists of two 1-mm thick ZnSe windows enclosing a  $30 \mu\text{m}$  thick liquid layer, attached to vacuum tubes.

The measurement series was repeated for two different configurations of the FRS instrument. After the first run of the measurement series, the performance of the spectrometer was enhanced with regard to the temporal compression of the MIR excitation pulse and the

detection dynamic range. Due to the implementation of six customized dispersive mirrors instead of four dispersive mirrors with insufficient GD variation, the temporal roll-off of the excitation pulse improved. The parameter  $t_B$  defined as the time after the maximum of the excitation pulse when the difference of two reference measurements reaches the noise floor, decreased from 700 fs in the first measurement series to 600 fs in the second measurement series as shown in Fig.(3.18a) and Fig.(3.18b). By inserting a magnifying telescope into the MIR beam path as described in Sec.(3.3.2), the overlap of the MIR beam and the sampling pulse beam on the EOS detection crystal was optimized. This improvement resulted in a 4 times better peak dynamic range as illustrated in Fig.(3.18c). How these upgrades influenced the instrument performance will be discussed in the following.

To extract the concentration of DMSO<sub>2</sub> molecules from the recorded EOS traces, the measurement of the highest concentration acted as calibration standard well above the noise floor of the FRS device. A calibration concentration of 1 mg/ml ensured linear scaling of the molecular signal with the concentration. To isolate the molecular response of the DMSO<sub>2</sub> molecules, the numerical difference of sample and reference traces was considered. The difference traces were truncated in the time domain at a varying start point  $T_1$  and at a fixed end point  $T_2$  of 1.4 ps after the maximum of the excitation pulse. Then the truncated difference traces were transferred to the frequency domain where a spectral window between 6.5  $\mu\text{m}$  and 11.8  $\mu\text{m}$  was analyzed. A 1-parameter fit of the resulting spectra to the reference spectrum at 1 mg/ml yielded the respective concentration.

Limiting the spectral window for the fit to the actual spectral coverage of the excitation pulse, excludes measurement noise which would be present in a direct time domain fit. For each nominal concentration, the mean value and the standard deviation of the concentration retrieved from the different measurements was calculated.

Fig.(3.19a-f) shows the mean values of the retrieved concentrations for increasing start point  $T_1$  for the first and the second measurement series, respectively. The error bars denote the absolute standard deviation and illustrate that the sensitivity of the FRS device depends on the temporal window which is considered for the concentration retrieval. If the temporal window starts too early after the excitation pulse as in Fig(3.19a-c), excess source noise deteriorates the detection limit. The optimum start point for the temporal window is defined by the parameter  $t_B$  when the difference of two reference traces coincides with the measurement noise floor. As the excitation pulse for the second measurement series decayed about 100 fs faster than the excitation pulse for the first measurement series, the optimum start point for time domain filtering decreased from 700 fs in Fig.(3.19e) to 600 fs in Fig.(3.19d).

In Fig.(3.19g) and Fig.(3.19h) the relative standard deviations for the nominal concentrations are depicted for the two measurement series and their optimum start point  $T_1$ , respectively. The limit of detection is defined as the concentration with a relative standard deviation of 100 % resulting in 800 ng/ml for the first measurement series and 300 ng/ml for the

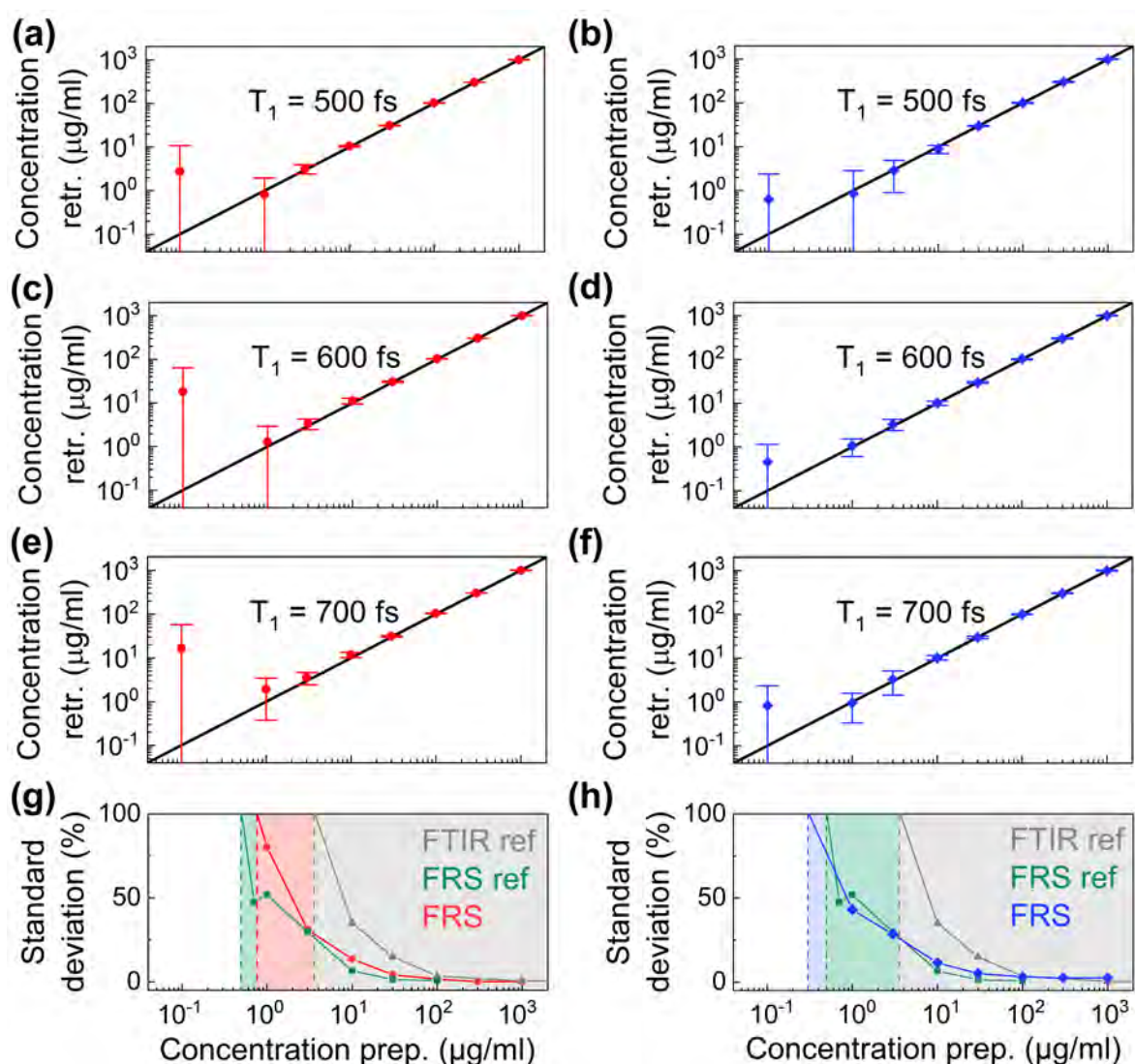


**Figure 3.19:** Evaluation of limit of detection for DMSO<sub>2</sub> solved in water. DMSO<sub>2</sub> Retrieved concentration for the first and b) the second DMSO<sub>2</sub> dilution series considering a temporal window between 500 fs and 1200 fs. c) Retrieved concentration for the first and d) the second DMSO<sub>2</sub> dilution series considering a temporal window between 600 fs and 1200 fs. e) Retrieved concentration for the first and f) the second DMSO<sub>2</sub> dilution series considering a temporal window between 700 fs and 1200 fs. The dots and diamonds denote the mean value and the error bars the absolute standard deviation of six measurements, respectively. g) Relative standard deviation of the retrieved concentrations for six measurements in the temporal window between 700 fs and 1200 fs for the first DMSO<sub>2</sub> dilution series and h) between 600 fs and 1200 fs for the second DMSO<sub>2</sub> dilution series. The dashed lines denote the limit of detection, respectively. For comparison, the same values are shown for a state of the art field-resolving spectrometer (FRS ref) and a commercial FTIR spectrometer (FTIR ref).

second measurement series. The improvement in LOD can be explained by the higher dynamic range and better temporal confinement of the excitation pulse in the second measurement series. To rank these values, the results of the benchmarking measurement performed with identical parameters and a commercial, research-grade FTIR spectrometer (MIRA Analyzer, MicroBiotlytics GmbH) as well as the state-of-the-art FRS instrument presented in [74] are shown. With optimized performance the FRS instrument presented here outperformed the LOD of 3  $\mu\text{g}/\text{ml}$  of the FTIR spectrometer by a factor of 10 and the state-of-the-art FRS instrument by a factor 1.7.

The determination of the LOD of  $\text{DMSO}_2$  solved in water is a first indicator for the performance of the developed spectrometer. Regarding the sensitivity to a specific molecule within a non-complex solvent, the developed instrument can compete with commercial FTIR spectrometers as well as with the state-of-the-art in FRS. Before commissioning the new device for real-world applications however, further studies are necessary. The demonstrated LOD must be reproduced on a day-to-day basis preferably with a larger number of measurements to validate statistics and in a spectroscopically more complex solvent than water. Also the specificity of the instrument, i.e. its ability to distinguish the relative concentration of different molecules must be characterized in a suitable experiment. To enable sophisticated biological studies with large numbers of samples the reproducibility of the exciting MIR waveform must be guaranteed over the period of several weeks. This is highly non-trivial in the context of high power femtosecond oscillators and requires further optimization of the system.

## 3.6 Towards a rapid-scanning instrument

The electric-field-resolving spectrometer presented here as well as time-resolving pump-probe studies [75], and two-dimensional spectroscopy [76] require mutual delaying between two (or more) involved laser pulses. Commonly, mutual delaying is implemented by varying the geometrical path length of one pulse with respect to the other. To this end, one pulse travels across a retroreflector mounted on a motorized translation stage. While the stage moves, the delay is recorded in synchrony with the signal.

This approach however, has two major drawbacks. Firstly, it involves mechanically moving parts and can therefore cause beam pointing fluctuations. Secondly, the stage speed is limited by the inertia of the moving components and restricts the scan rate to the few-Hz regime. This is neither sufficient to observe rapidly evolving systems like for instance, biological processes on their real time scale, nor to overcome technical noise which for most laser sources reaches into the kHz-regime.

In the field of FTIR spectroscopy, several concepts to increase the scan rate have been developed. Griffiths et al. [77] introduced a rapid scan spectrometer based on a tilted rotating mirror which allows for scan rates of 1 kHz. In another approach, the coated surface of a mechanical resonator driven by a piezo-oscillator vibrating at ultrasonic frequency acts as a rapidly moving mirror [78]. An implementation of this approach in our

electric-field-resolving spectrometer which enables a scan rate of 38 kHz is discussed below. Compared to other rapid scanning techniques, this idea is cost effective, conceptually simple, and in principle, applicable to any wavelength and spectral bandwidth. However, the amplitude of the mirror motion and therefore the maximum delay is limited to 1.5 ps [79]. Additionally, this approach as well as the rotating mirror approach rely on mechanically moving components and are therefore prone to pointing instabilities.

By exploiting an acousto-optic programmable dispersive filter (AOPDF) as delay line a similar scan rate of 36 kHz was achieved without the necessity of mechanically moving optical elements [80]. Here, the pulse train of a femtosecond laser and a shear acoustic wave interact inside an anisotropic medium. Upon interaction, part of the laser pulse is diffracted and changes its polarization from the ordinary to the extraordinary axis of the medium due to the acousto-optic effect [81]. The difference of the ordinary and the extraordinary refractive index leads to a temporal delay of the diffracted pulse at the end surface of the crystal with respect to the non-diffracted pulse depending on the position of temporal overlap between the acoustic and the optic pulse. The optic wave travels orders of magnitude faster inside the crystal than the acoustic wave such that consecutive laser pulses encounter a quasi-static acoustic pulse at increasing distance from the entrance surface of the crystal. This leads to a linearly evolving delay with a shot to shot increment defined by the difference between ordinary and extraordinary refractive index, the ratio of the speed of sound and light inside the crystal, and the repetition rate of the laser. The maximum delay depends on the length of the anisotropic medium. For typical crystal parameters and NIR lasers with tens of MHz repetition rate the time increment, i.e. the temporal resolution amounts to sub 10 fs and the maximum delay to a few ps. These values are perfectly suited for THz time-domain spectroscopy however, for MIR spectroscopy in liquid samples a longer delay and a higher temporal resolution are desirable. Interleaved scanning can increase the temporal resolution at the cost of the scan rate but the inflexibility of the scanning parameters is a major drawback of the acousto-optic delay line. In addition, costly post-amplification of the delayed sampling pulse required due to the low diffraction efficiency of the AOPDF adds further complexity to the system and reduces the attractiveness of the approach. However, the all-optical realization of the delay enables unprecedented timing precision as low as a few as [82] without any active feedback or delay axis correction.

The use of mode-locked oscillators offers yet another possibility for mutual delaying of two laser pulse trains. In asynchronous optical sampling (ASOPS), a constant offset in repetition frequency between two mode-locked oscillators introduces a linearly evolving delay ramp which is periodically repeated with the offset frequency  $\Delta f$  [83]. Dual-comb spectroscopy exploits the same idea for implementing a motionless FTIR spectrometer with frequency resolution ultimately limited by the comb line width [67]. Besides active stabilization of the repetition rate offset, frequency comb technology also requires the synchronization of the carrier-envelope phases of the employed oscillators. Our field-resolving spectrometer based on electro-optic sampling of intrinsically phase-stable IPDFG wave-

forms however, is insensitive to CEP fluctuations. Thus, the accuracy of the mutual delay from asynchronous oscillators is only limited by the timing jitter between the two pulse trains, i.e. defined by the ability to measure and control their repetition frequency offset.

The repetition rate and repetition rate offset define the maximum delay and the shot-to-shot delay increment, i.e. the temporal resolution in ASOPS. The delay increment  $\Delta t$  is given by  $\Delta t = \Delta f / (f_1 f_2)$  with the repetition rate  $f_1$  and  $f_2$  of the two mode locked oscillators, and the repetition rate offset by  $\Delta f = f_1 - f_2$  [84]. The maximum delay is determined by the inverse repetition rate  $f_1$  whereas the offset frequency inherently coincides with the scan rate. In combination with GHz oscillators, THz time-domain spectrometers with kHz scan rates and temporal resolution of a few hundred fs were realized with ASOPS [85, 86]. However, to resolve MIR radiation up to 60 THz with MHz oscillators repetition rate offsets below 10 Hz are necessary. Especially for spectroscopy in the liquid phase where dephasing times of less than 10 ps are common, the low repetition rate of the oscillator causes a long dead time and limits the duty cycle of such a spectrometer to less than one per mill. Together with the required low repetition rate offset, i.e. low scan rate, the ASOPS approach becomes unattractive for MHz systems.

By modulating the repetition rate offset of the two modelocked oscillators periodically around zero, the mutual delay can be reset after an arbitrary time defined by the periodicity of the modulation. This allows to maximize the duty cycle of the spectrometer by choosing the maximum delay adequate to the actual signal of interest. At the same time, the scan rate defined by the modulation frequency is increased. In electronically controlled optical sampling (ECOPS), the repetition rate of one oscillator is locked to the repetition rate of the second oscillator with a phase-locked feedback loop whose set point can be varied with an arbitrary function generator [87]. The amplitude and frequency of this variation are used to adjust the scanning parameters to the experimental needs. This possibility makes ECOPS the most flexible approach towards a rapid scanning instrument and justifies its high cost and complexity.

### 3.6.1 Delay axis calibration in rapid scanning

In comparison to mechanical delay lines, where the actual optical path difference can be precisely tracked with an interferometer as described above, dual oscillator approaches require more advanced schemes for delay tracking. Common ASOPS or ECOPS THz time-domain spectrometers rely on the precision of the repetition rate offset for delay axis calibration. Ideally, the delay  $\tau$  increases with measurement time  $t$  as  $\tau = \Delta f t / f_1$  [88]. Thus, any timing jitter between the oscillators causes a deviation of the repetition rate offset  $\Delta f$  from the nominal value and therefore a time axis calibration error. Timing jitter is greatly suppressed if the two asynchronous pulse trains are emitted from the same laser resonator. This was achieved in an Yb:YAG thin disk laser by sharing all cavity optics including the active medium except for the end mirrors and output couplers [89]. Thus two spatially separated pulse trains emerge with the possibility to independently control the repetition rate via the position of the end mirror. Another approach for fiber lasers

is to exploit chromatic dispersion inside the cavity to generate two pulse trains at slightly different wavelength and repetition rate [90].

If two independent cavities are employed, active synchronization of the repetition rates is necessary to reduce the timing jitter. This requires the precise detection of the momentary repetition rate difference and the compensation of deviations thereof from the nominal repetition rate difference. Commonly, the compensation is achieved in a master-slave configuration where the cavity length of the so-called slave oscillator is adjusted with a piezoelectric transducer (PZT). However, the suppression of the delay axis calibration error in these schemes is limited by the sensitivity of detecting the instantaneous repetition rate offset and the ability to control it.

An electronic approach to generate an error signal proportional to the momentary difference in repetition rate is to convert the two pulse sequences into RF signals using amplified photodiodes and compare them electronically. By using higher harmonics of the repetition rate instead of the fundamental, the sensitivity of the error signal to timing jitter increases accordingly [88]. However, due to electronic noise, saturation effects in the photodiode and coupling of amplitude and phase noise the resulting timing jitter still lies above 10 fs. This result suffices to temporally resolve THz transients as the standard application of ASOPS/ECOPS, but MIR waveforms require an at least one order of magnitude better timing precision.

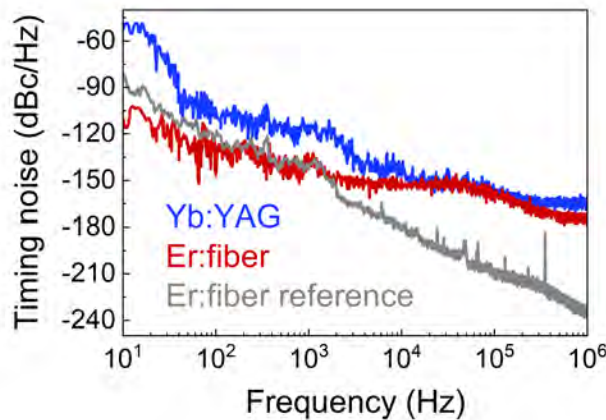


**Figure 3.20:** Comparison of the timing noise of the Yb:YAG oscillator and a commercial Er:fiber oscillator at the 368th and 183th harmonic of the repetition rate, respectively. The grey line denotes a more precise reference measurement of the Er:fiber laser with a balanced optical cross-correlator.

Compared to the direct extraction of RF signals from optical pulse trains, balanced optical-to-microwave phase detection (BOM-PD) reduces the influence of amplitude-to-phase noise coupling and photodetector nonlinearities [91]. In this method, the timing information between a microwave signal and an optical pulse train is transferred into the optical domain before detection with a photodiode via a differentially biased Sagnac fiber

loop [92]. This enabled the extraction of an RF signal from an optical pulse train with a timing jitter smaller than 2 fs [93]. However, our attempts to use a commercial BOM-PD (Menlo, BOM-PD High-resolution optical-RF phase detector) to detect the repetition rate of the high power Yb:YAG thin disk oscillator were not successful. The main difference to previous BOM-PD experiments is the oscillator technology. The high average power of the Yb:YAG thin disk laser requires high pump power and continuous water flow for cooling which translates into increased intensity noise. In addition, the Kerr lens based modelocking mechanism enhances amplitude-to-phase noise coupling [94].

To verify this assumption we performed a timing noise measurement of the Yb:YAG oscillator at the 368th harmonic of the repetition rate with an amplified photodiode and an RF spectrum analyzer. The measurement was repeated with a commercial low noise Er:fiber oscillator (Menlo, C-fiber femtosecond erbium laser) for comparison as shown in Fig.(3.20). Since the described method is only a coarse characterization of the timing noise a reference measurement with a balanced optical cross correlator for the commercial fiber laser was provided by the manufacturer (grey line). A comparison of the Er:fiber timing noise for the two methods reveals that above 2 kHz the direct measurement with the photodiode was limited by the electronic noise of the RF spectrum analyzer. Therefore, the simple measurement is not sufficient to characterize the timing jitter across the whole bandwidth from 10 Hz to 1 MHz but it supports the assumption that the high power Yb:YAG oscillator shows increased timing jitter compared to a low power fiber oscillator which is the workhorse for THz time domain spectroscopy with dual oscillator rapid scanning.

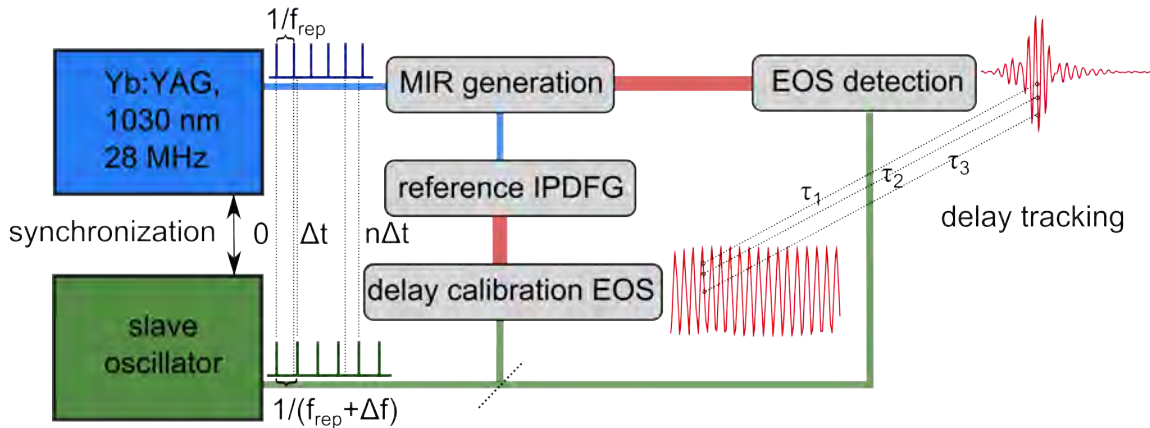


**Figure 3.21:** Schematic layout of a dual oscillator rapid scanning setup including electro-optic delay tracking. The Yb:YAG oscillator generates a phase stable mid infrared (MIR) waveform which is electro-optically sampled by a second oscillator with detuned repetition rate  $f_{rep}$ . With the delay calibration EOS a reference IPDFG transient is recorded to track the precise delay between the asynchronous pulse trains for each laser shot.

Due to the complication of repetition rate synchronization including a high power Yb:YAG thin disk oscillator, we designed a solution for delay axis calibration which is

not determined by the mutual timing jitter of the asynchronous pulse trains. Instead of relying on the suppression of timing jitter, the idea is to precisely track the momentary delay between the two pulse trains in a purely optical manner.

In the specific example of the presented *Infrasampler*, the Yb:YAG oscillator is utilized to generate inherently phase stable midinfrared waveforms which are electro-optically sampled by a second oscillator with a detuned repetition rate. To simultaneously track the momentary delay between the two loosely locked pulse trains, the Yb:YAG driving pulses are recycled after MIR generation to produce a second IPDFG transient. This reference transient is also electro-optically sampled by the second oscillator and allows for mapping the measured reference EOS signal to an exact delay position [95]. Ideally, the reference transient has a constant instantaneous frequency and amplitude across the entire delay range of interest. Electro-optic delay tracking (EODT) is also applicable to a chirped reference transient with varying amplitude if it was precisely determined before. However, a crucial condition is that the mutual shot-to-shot timing jitter is smaller than half the oscillation period of the reference transient. If the recording of the EODT signal and the actual EOS measurement are synchronized by a suitable trigger each laser shot can be unambiguously correlated with a precise delay.

The high sensitivity of EOS detection together with inherently phase stable IPDFG waveforms promises a delay axis calibration error for EODT well below 1 fs.

### 3.6.2 First experimental rapid scanning traces in the mid infrared

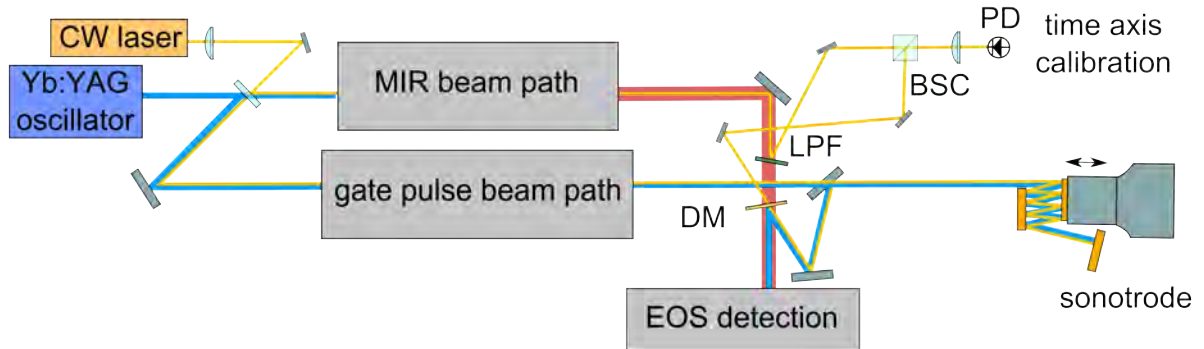
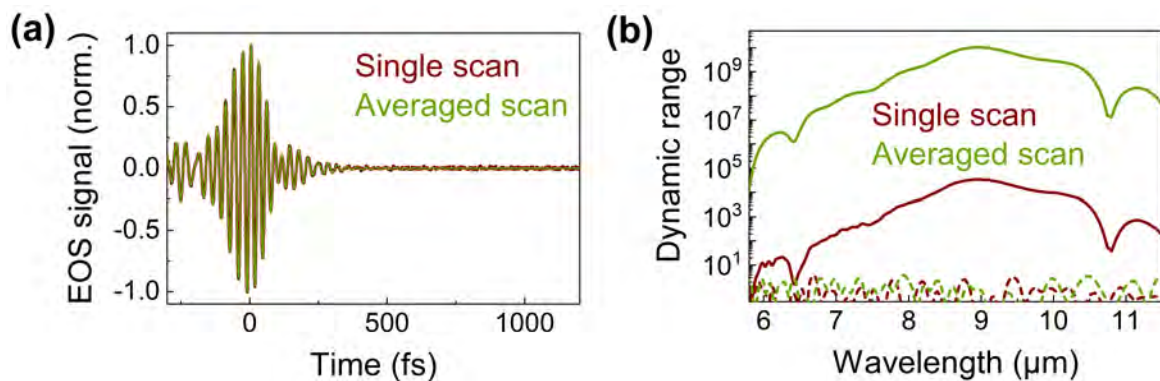


**Figure 3.22:** Sketch of the experimental setup for rapid scanning with a sonotrode oscillating at 19.2 kHz. To achieve a maximum delay of 1.5 ps the sampling pulse undergoes 8 reflections on a mirror glued to the sonotrode surface. The delay axis is calibrated with an interferometric signal generated by a CW laser. LPF: 3  $\mu\text{m}$  long pass filter, BSC: beam splitter cube, DM: dichroic mirror, PD: photodiode.

Besides time-axis calibration, all rapid scanning techniques require fast detectors and analog-to-digital converters capable of recording every laser shot with sufficient dynamic

range, and computational infrastructure to handle the increased amount of generated data. As these requirements already complicate the EOS detection of MIR waveforms, we set up an experiment based on a fast mechanical delay line before implementing the more complex dual oscillator solution. Another aim of this pre-experiment is to analyze the noise behavior of EOS measurements if single scans are recorded faster than the MIR intensity fluctuates.

To this end, we employ a mirror glued to the rapidly oscillating surface of a sonotrode<sup>2</sup> to introduce a geometrical path difference in the NIR sampling arm. The sonotrode consists of a PZT driven at 19.2 kHz which couples an acoustic wave to an ultrasonic resonator where the amplitude of the vibration is amplified [78]. The sampling beam travelled eight times over the oscillating mirror to increase the maximum delay range to 1.5 ps. These multiple reflections amplify beam pointing instabilities due to the sonotrode motion and render the setup prone to beam clipping. As in IDT a CW laser at 1550 nm co propagated with the MIR and the NIR beam to calibrate the time axis of the sonotrode scan. In this approach, the interference pattern of both beams was directly recorded with a photodiode and fed into a predictor-corrector algorithm. Thus, a time axis calibration error as low as 111 as for a single scan and 14 as for 100 scans was achieved [79].



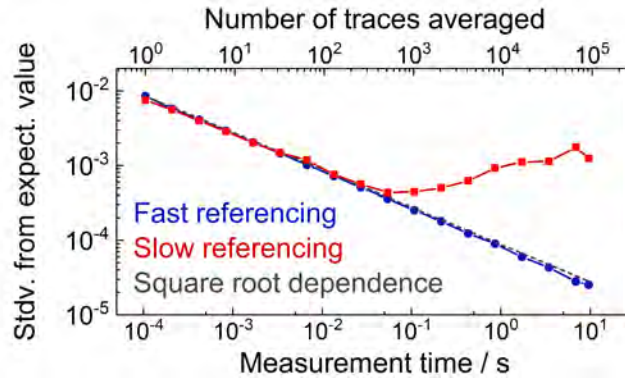
**Figure 3.23:** a) EOS trace of the MIR pulse measured with a sonotrode delay line. A single scan is recorded within 25  $\mu\text{s}$ . For the averaged trace 365800 single scans were acquired within 9 s. b) Representation of the EOS signal in the frequency domain normalized to the according noise floor.

Fig.(3.23a) shows an EOS trace recorded with the sonotrode within 25  $\mu\text{s}$ . The red line denotes a single scan and the green line denotes the average of 365800 normalized scans which are acquired within a measurement time of 9 s. In Fig.(3.23b) the measurement dynamic range is depicted for the single and the averaged scan as the Fourier transformation normalized to the corresponding noise floor. The maximum dynamic range in a single scan is  $3 \times 10^4$  and in the averaged scan it is  $10^{10}$ . At the time of this measurement, the optimization of the EOS detection and MIR generation had not been finalized. Therefore,

<sup>2</sup>The sonotrode was provided by our collaborator Prof. Dr. Joachim Heberle at the Freie Universität Berlin. All measurements with this device were performed by my colleagues Alexander Weigel, Philip Jacob, and David Gröters.

the temporal profile as well as the spectral coverage and maximum dynamic range deviate from the measurements shown in Section 3.3.

To evaluate the potential of recording entire EOS traces with a rate of 38.4 kHz, i.e. faster than most technical noise affecting the measured signal in slow scan, two different reference techniques were evaluated. The difference of two consecutive traces in the time domain as well as the spectral division of their Fourier transform was calculated for an increasing number of measurements. When the referencing of single forward and backward scans was performed before averaging, the standard deviation from the expectation value of both referencing methods decreased with the square root of the number of measurements. When the single scans were averaged before referencing, the standard deviation started to increase again for measurement times longer than 50 ms due to technical noise in the low frequency range [96]. The deviation from the expectation value in the case of differential referencing is shown in Fig.(3.24) for an increasing number of measurements, i.e. increasing measurement time. The red squares correspond to the situation of differential referencing after averaging of the corresponding number of measurements, which is comparable to slow scanning.



**Figure 3.24:** Standard deviation from the expectation value in the case of differential referencing for an increasing number of measurements, i.e. measurement time. The blue line corresponds to fast referencing, i.e. subtraction of single forward and backward scans before averaging. The red line corresponds to slow referencing, i.e. averaging of single scans before subtraction.

This behavior indicates that fast referencing allows to scale the sensitivity of the instrument by increasing the measurement time without being limited by fluctuations of the laser system. Thus, rapid scanning with the sonotrode-approach ‘freezes’ technical noise on the time-scale of a single scan.

Besides fast scanning, intra-scan referencing [97] can also eliminate technical drifts on the time-scale of typical measurement durations of several tens of seconds. In intra-scan referencing, reference and sample traces are recorded with conventional slow scanning in a quasi-simultaneous manner. This results in very similar signal distortions in the two traces due to technical noise which cancel upon referencing.

Because rapid scanning based on the sonotrode-approach offers very limited flexibility of the scanning parameters and is prone to mechanical instabilities the further development of a rapid scanning instrument focuses on a dual-oscillator concept.

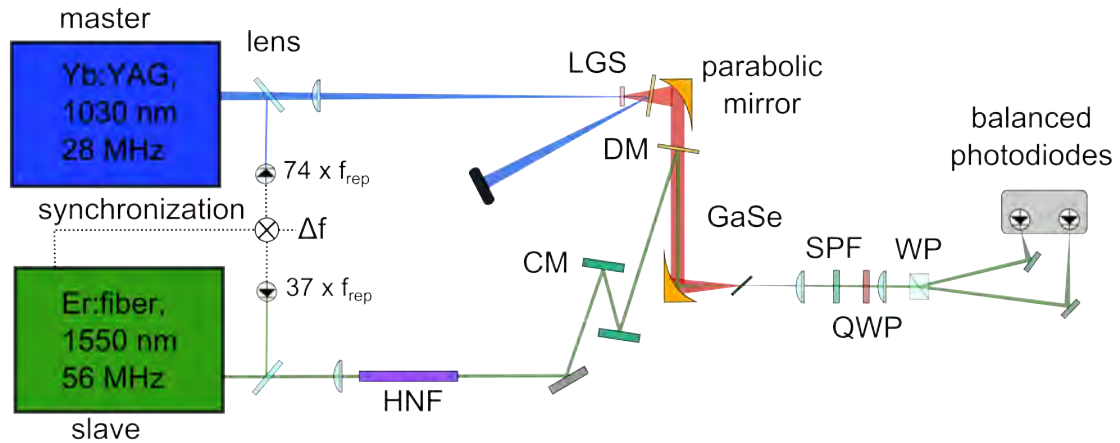


**Figure 3.25:** Schematic layout of the dual oscillator rapid scan. The Yb:YAG oscillator generates MIR radiation which is electro -ptically sampled by a second oscillator with detuned repetition rate. The repetition rates of the two oscillators are actively synchronized with an error signal based on the 74th and 37th harmonic of the repetition rate, respectively. LGS: *LiGaS<sub>2</sub>* crystal, DM: dichroic mirror, CM: chirped mirror, HNF: highly nonlinear fiber, SPF: short pass filter, QWP: quarter wave plate, WP: Wollaston prism, GaSe: GaSe crystal.

Therefore, the sampling pulse train for EOS detection was generated by a second mode locked laser instead of splitting it off from the driving pulse as described above. The second oscillator was a commercial Er:fiber laser (Menlo, C-fiber femtosecond erbium laser) emitting 90 fs pulses at a central wavelength of 1550 nm with an average power of 300 mW and a repetition rate of 56 MHz. The repetition rate was chosen to be exactly twice the repetition rate of the Yb:YAG oscillator generating the MIR probe pulses and enables lock-in detection at 28 MHz. The commercial oscillator was employed as slave oscillator and therefore includes a stepper motor and a PZT element with up to 80 kHz bandwidth to control the repetition rate. The 90-fs output pulses were further spectrally broadened and compressed to 11 fs in a highly nonlinear fiber assembly<sup>3</sup> (for further information see Section 4.3.3 and [98]) to achieve sufficient temporal resolution to sample radiation with wavelengths down to 5  $\mu\text{m}$ .

First, we conducted an ASOPS measurement<sup>4</sup> with a constant repetition rate offset of 3.24 Hz between the Yb:YAG and the Er:fiber oscillator. Therefore the 74th harmonic

<sup>3</sup>The highly nonlinear fiber assembly was designed and provided by the group of Prof. Dr. Alfred Leitenstorfer at the University of Konstanz

<sup>4</sup>All measurements using the ASOPS and ECOPS technique were performed by my colleagues Alexander Weigel and Philip Jacon.

of the Yb:YAG repetition rate at 2072 MHz detected with an amplified photodiode was mixed with the signal of a direct digital synthesizer (DDS) including the desired repetition rate offset. Accordingly, the 37th harmonic of the Er:fiber repetition rate at 2072 MHz was mixed with the signal of a second DDS synchronized to the first DDS. By mixing the resulting RF signals, an error signal proportional to the desired repetition rate offset and the deviation thereof due to timing jitter between the oscillators was generated. The error signal was used to lock the repetition rate of the Er:fiber laser to the repetition rate of the Yb:YAG laser with the desired offset via a PI<sup>2</sup>D controller acting on the cavity length of the former.

To account for the difference in sampling pulse wavelength a second EOS detection with a 300  $\mu\text{m}$  thick GaSe crystal at a theta angle of  $43^\circ$  was set up. A sketch of the experiment is shown in Fig.(3.25). The resulting EOS trace recorded with ASOPS at 3.24 Hz repetition rate offset is shown in Fig.(3.26a). The delay axis was calibrated according to  $\tau = \Delta f t / f_1$  with the nominal values for the repetition rate offset frequency  $\Delta f$  and the repetition rate  $f_1$  of the Yb:YAG oscillator. The time axis calibration allows to perform a Fourier transformation and calculate the measured spectrum of the MIR waveform which is depicted in Fig.(3.26b). For comparison, the spectrum measured with a conventional mechanical scan, sampling pulses with a central wavelength of 1030 nm, and a 85  $\mu\text{m}$  thick GaSe crystal is shown in green. The difference in spectral coverage between mechanical scan and ASOPS has two main reasons. The ASOPS measurement was performed in ambient air and the mechanical scan at a pressure of  $10^{-3}$  mbar. Therefore the spectrum recorded with ASOPS shows absorption features below 7  $\mu\text{m}$  which can be attributed to water vapor (grey line for reference). The increased spectral coverage of the ASOPS measurement for wavelengths above 10  $\mu\text{m}$  can be explained by the difference in sampling pulse wavelength. The phase matching bandwidth of the SFG involved in the EOS detection process for a 1550 nm sampling pulse is broader than for a 1030 nm sampling pulse although the GaSe crystal for the 1550 nm pulses is thicker.

The dynamic range of a single scan ASOPS measurement and a single mechanical scan measurement is not directly comparable due to the longer integration time for the latter. In ASOPS one data point corresponding to a single laser shot is recorded with a shot-to-shot delay increment of 4 fs whereas for the mechanical scan at a stage speed of 0.25 mm/s 138613 laser shots are averaged within the same delay period. Assuming that the SNR scales with  $\sqrt{N}$  for increasing number of averages, one can estimate the single scan dynamic range in ASOPS required to reach the performance of the mechanical scan. The major limitation in this experiment is the average power of the commercial Er:fiber oscillator generating the sampling pulses. The sampling pulse power on the EOS crystal is 50 mW for the Er:fiber oscillator compared to 350 mW for the Yb:YAG oscillator. To achieve comparable conditions for both methods the losses in the Er:fiber beam path can be reduced by using customized optics, the MIR and sampling beam spot size on the EOS crystal can be minimized to increase the sampling pulse intensity, and the broader phase matching bandwidth at 1550 nm enables the use of thicker GaSe crystals.

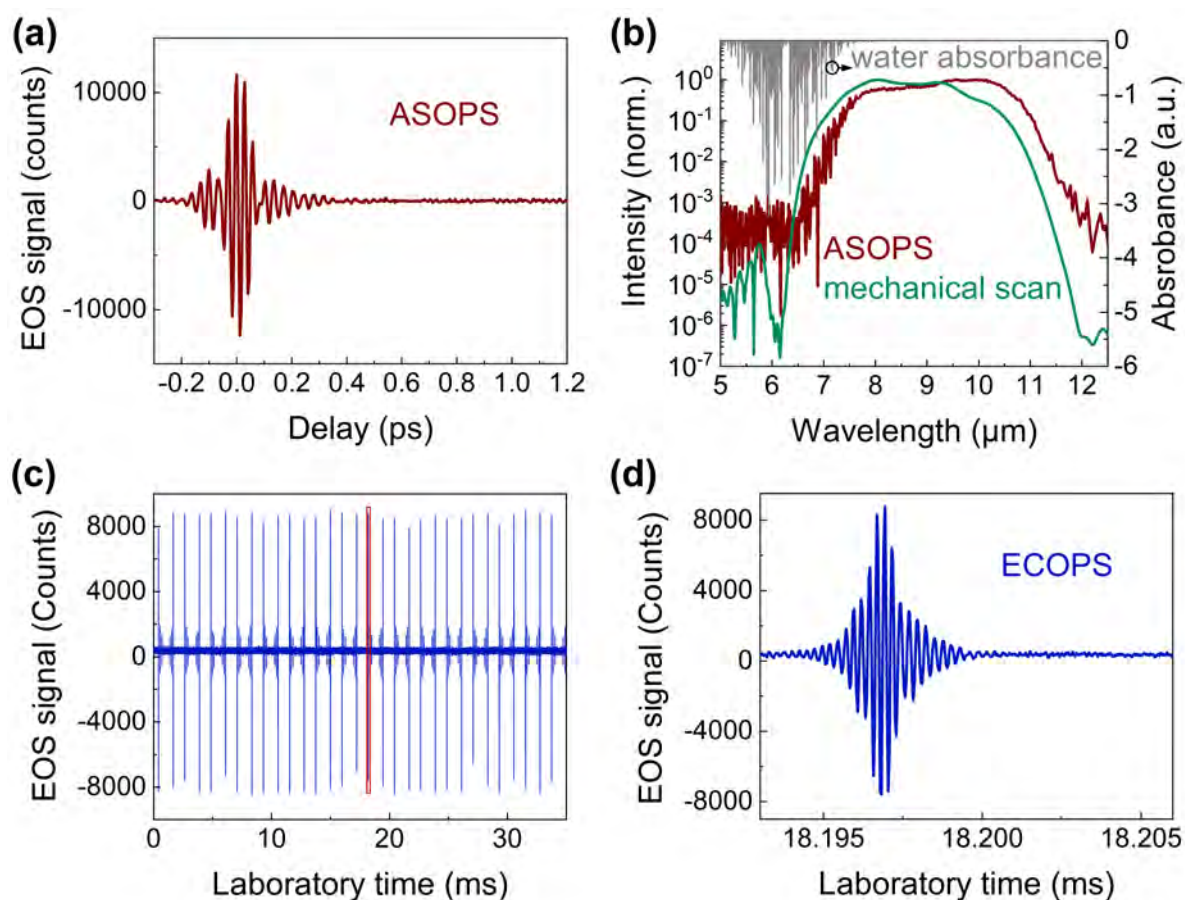


**Figure 3.26:** EOS measurements with dual oscillator fast scan. **a)** Asynchronous optical sampling (ASOPS): The offset in repetition rate between the two mode locked lasers is locked to 3.24 Hz resulting in 6.5 scans per second. **b)** Frequency domain representation of a single scan ASOPS measurement. For comparison a normalized spectrum recorded with conventional mechanical scanning is shown in green and the absorbance of water vapor in grey. **c)** Electronically controlled optical sampling (ECOPS): The offset in repetition rate between the two mode locked lasers is modulated between 3.24 Hz and -3.24 Hz at a frequency of 450 Hz. The time axis is shown in laboratory time instead of delay. **d)** Close-up of the time axis section illustrated by the red square in part (c).

Although the demonstrated ASOPS configuration allowed to record the EOS trace shown in Fig.(3.26a) within 13  $\mu\text{s}$  the repetition rate offset frequency of 3.24 Hz required to achieve a delay increment sufficient to sample MIR radiation with MHz oscillators limited the number of scans to 6.5 per second. By modulating the repetition rate offset between 3.24 Hz and -3.24 Hz with a modulation frequency of 450 Hz the number of scans increased to 900 per second. The resulting EOS trace recorded in ECOPS mode is shown in Fig.(3.26c). The alternating sequence of forward and backward scans indicates the sign switch of the repetition rate offset. The time axis section indicated by the red rectangular

is depicted as close-up in Fig.(3.26d) and reveals that the oscillations of the MIR waveform can be resolved with ECOPS. The time axis is given in laboratory time because delay axis calibration is more complex compared to ASOPS as the repetition rate offset constantly changes. In the future, a precise delay axis calibration will be provided by EODT. The repetition rate offset modulation frequency and therefore the scan rate can be increased to several kHz with optimized PI<sup>2</sup>D loop settings.

In conclusion, a first dual oscillator scan at fixed and modulated repetition rate offset frequency was realized with a high power MHz laser resolving wavelength down to 6  $\mu\text{m}$ . Delay axis calibration with EODT promises similar precision to IDT for mechanical scanning without requiring a tight synchronization of the oscillator repetition rates. A thorough quantitative comparison of the SNR behavior in mechanical and dual oscillator scan is currently being conducted in our laboratory to assess the performance of the new methods. The noise behavior of the sonotrode scan indicates the potential of recording single EOS traces faster than the major contributions of technical noise.

# Chapter 4

## Broadband interferometric subtraction of optical fields

In this chapter, the concept of *optical arithmetic*, i.e. the experimental *subtraction* of light fields by overlapping them in space and time with opposing phase, is introduced. The first section of this chapter explains how this concept can be exploited to overcome common limitations in spectroscopy, whereas the second section gives a quantitative estimation of the expected sensitivity improvement due to optical subtraction in the cases of time-integrated and field-resolved spectroscopy. The third section deals with the experimental realization and characterization of a deep nulling interferometer first in the near-infrared and then in the mid-infrared spectral region.

### 4.1 Advantages of differential spectroscopy

Any spectroscopic instrument is limited in detection sensitivity by undesired fluctuations of the measured signal, that is, technical noise. These signal fluctuations incorporate excitation, detection, and digitization noise. For laser-based sources with high brightness, usually the former is dominating due to increased excitation noise as compared to thermal light sources. In an excitation noise limited frequency-domain measurement the minimum detectable absorbance is approximately given by the relative intensity noise of the light source in the considered spectral element [36]. In a time-domain measurement, this restriction can be relaxed due to the temporal separation of excitation and sample response. As shown in Chapter 3 the developed *Infrasampler* allows to detect the resonant response of a molecular sample in a shot-noise-dominated manner. However, the time window for shot-noise dominated detection is restricted by the temporal roll-off of the excitation pulse.

We showed that we can temporally compress the excitation pulse in Section 3.4.2 but the roll-off remains unsatisfactory. In Section 3.4.1 we demonstrated that at a working pressure of  $10^{-3}$  mbar all molecular background from the surrounding environment is reduced to the detection noise floor. However, for real-world samples, the molecules of interest occur

in a surrounding of a variety of highly abundant molecules often carrying no relevant information. To isolate the molecular signal of interest one commonly records a sample measurement and a reference measurement containing only the highly abundant molecules consecutively and subtracts or divides them numerically. The quality of the suppression of molecular background and exciting light pulse in this numerical referencing is defined by the reproducibility of the spectroscopic instrument which in turn is mainly determined by the intensity noise of the employed light source and the accuracy of the delay-axis in the case of the *Infrasampler*.

If the subtraction of sample and reference signal is carried out optically in a broadband destructive interferometer, it renders the sensitivity of the spectrometer independent of fluctuations of the source intensity and the delay scan in the ideal case. To this end, the sample is placed in one arm and the reference is placed in the other arm of a symmetric interferometer such that the destructive port reveals the exact difference and common fluctuations are cancelled [99]. The advantage of this method for frequency-domain spectroscopy is evident but it also enhances the sensitivity of field-resolved spectroscopy including time-domain gating. It enables background-free detection in principle immediately after the excitation and increases the visibility of low abundant components in the presence of the molecular background signal.

In 1966 Bar-Lev established the field of dual-beam FTIR spectroscopy and utilized balanced detection to eliminate common intensity fluctuations of the interferogram and the anti-interferogram beam produced by an FTIR spectrometer [100]. In later works [101, 102], sample and reference were inserted into the interferogram and anti-interferogram beam, respectively. Both beams were focused onto a single detector to cancel the common AC components of the opposing interferograms. Besides mitigating the intensity noise limitation, these concepts helped to relax the dynamic range requirements of the digitization electronics and reduced the measurement time [103].

However, in all dual-beam FTIR schemes the DC-component of the interferogram (i.e. the baseline) is always present on the detector which can lead to detector saturation. In contrast, optical subtraction of reference and sample signal leads to the spatial isolation of the sought-for difference signal (ideally) free from background. Thus, the dynamic range requirements of the detector are dictated by the (much weaker) actual signal of interest.

For EOS-based detection, this reduction of the signal dynamic range is advantageous already before the signal hits the photo diodes. If a comparably large number of MIR photons reaches the EOS crystal, the involved SFG process can lead to a considerable depletion of gate pulse photons. This results in a nonlinear EOS response with respect to the electric field of the MIR pulse. Interferometric subtraction reduces the number of MIR photons to the actual signal of interest and helps to avoid this undesirable nonlinear effect. At the same time the reduction to the actual signal of interest at the EOS crystal facilitates focusing the MIR beam to its diffraction limited spot size without being limited by the damage threshold of the EOS crystal. Increasing the intensity by minimizing the MIR focal spot size enhances the sensitivity of the EOS detection but leads to crystal damage in a direct measurement without interferometric subtraction. This advantage will gain even more importance as soon as MIR sources with higher power will become available.

## 4.2 Sensitivity improvement due to optical subtraction

Before describing the experimental realization of broadband optical subtraction, an estimation of the signal-to-noise ratio improvement due to this method for different spectroscopic techniques based on analytical expressions and a numerical model is presented. In source-noise-limited frequency-domain spectroscopy, the suppression of RIN directly affects the ability of an instrument to detect small concentrations of a specimen. Due to the temporal separation of excitation and sample response the detection sensitivity in time-domain spectroscopy is less exposed to excess source noise. However, the suppression of molecular background noise in broadband optical subtraction still increases the visibility of low-abundance molecules. The influence of a finite, fluctuating extinction ratio on this sensitivity improvement is discussed in the following.

### 4.2.1 Differential vs. direct measurements in frequency-domain spectroscopy

In this section, we derive expressions for the signal-to-noise ratio in direct and differential transmission spectroscopy in the frequency domain to understand the connection between intensity noise suppression and sensitivity improvement in broadband optical subtraction. The two different configurations are illustrated in Fig.(4.1).

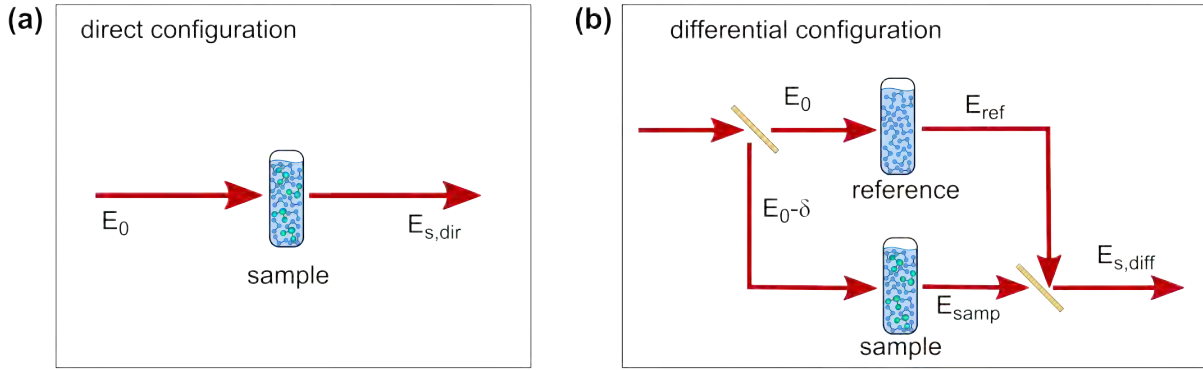


**Figure 4.1:** Illustration of the direct (a) and the differential (b) measurement configuration. In the differential configuration the electric field amplitude in the sample arm is reduced by the imbalance factor  $\delta$  to account for an imperfect interferometric extinction.

According to Beer's Law, the power of a light source within a spectral element after transmission through a sample with attenuation  $A$  is:

$$P_{s,dir} = P_0 e^{-A}, \quad (4.1)$$

where  $P_0$  is the power arriving at the detector without the sample. The attenuation  $A$  is proportional to the absorption cross section within the spectral element, the sample

concentration, and the sample thickness.  $P_{s,dir}$  is the quantity which is commonly measured in frequency-domain, transmission spectroscopy. However, the power attributed purely to the light-matter interaction under scrutiny is the difference between  $P_0$  and this quantity:

$$P_{M,dir} = P_0 - P_{s,dir} = P_0 (1 - e^{-A}). \quad (4.2)$$

The purely molecular signal  $P_{M,dir}$  vanishes in the limit of  $A \rightarrow 0$  and the measured quantity  $P_{s,dir}$  reduces to the background signal  $P_0$ . The equality  $E = c\sqrt{P}$  with the proportionality constant  $c$  connects the electric field and the measured power. Therefore, we can write:

$$E_{s,dir} = c\sqrt{P_0 e^{-A}} = E_0 e^{-A/2}, \quad (4.3)$$

with  $E_0 = c\sqrt{P_0}$ .

To calculate the molecular signal in optical subtraction, we begin with the interference of the opposing electric fields from the reference and the sample arm. As the destructive interference in a real-world experiment will always be imperfect, a finite interferometric extinction is modelled as a small imbalance  $\delta$  in the electric field amplitudes, i.e.  $\delta = \sqrt{4\Delta}$  with the extinction ratio  $\Delta$ . The extinction ratio  $\Delta$  is defined as the ratio of the intensities of destructive and constructive interference which is the experimental observable for the imperfect interferometric extinction. In the following, this imbalance is accounted for by reducing the electric field amplitude of the sample field with respect to the reference field. Thus, the electric field of the differential signal  $E_{s,diff}$  reads:

$$E_{s,diff} = E_{ref} - E_{samp} = E_0 - (1 - \delta) E_0 e^{-A/2} = E_0 (1 - (1 - \delta) e^{-A/2}) \quad (4.4)$$

and the power arriving at the detector is given by:

$$P_{s,diff} = \frac{1}{c^2} E_{s,diff}^2 = P_0 (1 - (1 - \delta) e^{-A/2})^2. \quad (4.5)$$

To obtain the purely molecular signal we subtract the background signal which is defined as  $\lim_{A \rightarrow 0} (P_{s,diff}) = P_0 \delta^2$ :

$$P_{M,diff} = P_0 \left( (1 - (1 - \delta) e^{-A/2})^2 - \delta^2 \right). \quad (4.6)$$

Here, we accounted for the finite extinction ratio by reducing the electric field amplitude of the sample arm, see Eqn.(4.4). A similar derivation can be performed by reducing the electric field amplitude of the reference arm. The resulting small difference in the molecular signal compared to Eqn.(4.6) is negligible for most practical cases.

Besides the expressions derived for the purely molecular signal in the direct and differential measurement in Eqn.(4.2) and Eqn.(4.6), respectively, we need to quantify the noise powers for the two configurations to compare the limit of detection. To this end, we consider the uncorrelated noise contributions of the laser intensity noise  $P_L$ , the detector noise  $P_{det}$ , and the shot noise  $P_{SN}$  to the total noise power  $P_{N,tot}$ :

$$P_{N,tot} = \sqrt{P_L^2 + P_{det}^2 + P_{SN}^2}. \quad (4.7)$$

The detector noise is a constant defined by the noise equivalent power of the employed detector but the laser and the shot noise scale with the power incident on the detector. Thus, we can write the noise power in the direct measurement  $P_{N,dir}$ :

$$P_{N,dir} = \sqrt{(\sigma P_{s,dir})^2 + P_{det}^2 + \frac{P_{s,dir}hf}{T}}, \quad (4.8)$$

and the differential measurement  $P_{N,diff}$ :

$$P_{N,diff} = \sqrt{(\sigma P_{s,diff})^2 + P_{det}^2 + \frac{P_{s,diff}hf}{T}}, \quad (4.9)$$

where  $\sigma$  is the relative intensity noise of the laser source,  $h$  is Planck's constant,  $f$  is the optical frequency, and  $T$  is the measurement time for the respective spectral element. Now we can determine the minimum detectable attenuation, i.e. the limit of detection (LOD) for both configurations by setting the total noise power equal to the purely molecular signal which corresponds to a signal-to-noise ratio of 1. Solving the equation  $P_{N,tot} = P_M$  for the attenuation  $A$  reveals an expression for the LOD depending on the input power, the system-dependent noise parameters, and the extinction ratio.

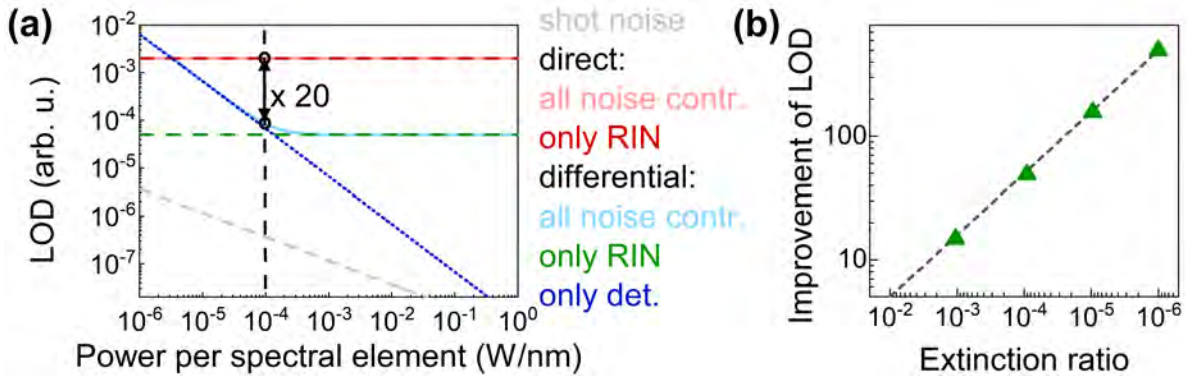


**Figure 4.2:** **a)** Comparison of the limit of detection (LOD) in the direct and the differential case for increasing power per spectral element for a relative intensity noise (RIN) of 0.2 % and an extinction ratio of  $6.4 \times 10^{-4}$ . The dashed black line denotes the power level of the Er:fiber laser. **b)** Ratio of the direct and the differential LOD in the intensity noise limited regime. For decreasing extinction ratio the LOD improvement asymptotically approaches  $1/\sqrt{4\Delta}$  (dashed black line).

Fig.(4.2a) shows the LOD for the direct and the differential configuration calculated for the experimental parameters used to detect the methane resonances shown in Fig.(4.12) for increasing power per spectral element. In this case, the RIN was determined to 0.21 % (integrated in the frequency band between 1 Hz and 100 kHz) and the extinction ratio amounted to  $6 \times 10^{-4}$ . The incident power  $P_0$  of 100  $\mu$ W/nm provided by the employed Er:fiber laser is indicated with a dashed black line. We consider a  $4 \times 10^{-2}$ -nm broad spectral element centered at 1645 nm with a respective measurement time of 10 ms. The

noise equivalent power of the utilized optical spectrum analyzer at this wavelength is  $1.6 \times 10^{-10}$  W/nm.

To distinguish the influence of the different noise contributions, Fig.(4.2a) also shows different LOD curves accounting solely for laser intensity noise, shot noise, or detector noise, respectively. For both configurations, the common shot-noise-limited LOD curve confirms the fundamental limit imposed by linear spectroscopy with classical light. In the direct measurement, the LOD is intensity-noise-limited for all considered powers whereas the differential measurement is purely detector-noise-limited up to  $60 \mu\text{W}/\text{nm}$  resulting in a worse differential LOD up to  $3 \mu\text{W}/\text{nm}$  compared to the direct LOD. This is caused by the fact that the purely molecular signal in the differential configuration is reduced depending on the extinction ratio (see Eqn.(4.6)). Due to the suppression of laser intensity noise however, the differential LOD at the employed power per spectral element of  $100 \mu\text{W}/\text{nm}$  is improved by a factor of 20 compared to the direct LOD. Thus, the input power  $P_0$  has to be sufficiently high to reach the intensity-noise-limited regime in the differential measurement to fully exploit the sensitivity improvement in optical subtraction. The onset of the intensity-noise-limited regime shifts to higher powers with improving extinction ratio but it is never limited by detector saturation. In optical subtraction, the signal arriving at the detector mainly consists of the purely molecular signal and a small contribution from the extinction-ratio-dependent background.

Fig.(4.2b) illustrates the LOD improvement in optical subtraction estimated for different extinction ratios in the intensity-noise-limited regime. The green triangles are the ratio of the calculated LOD for the differential and the direct case. For decreasing extinction ratio, the LOD improvement asymptotically approaches  $1/\sqrt{4\Delta}$  (dashed black line) assuming the availability of sufficiently high power. This dependence demonstrates the potential of broadband optical subtraction for sensitivity improvement in classical transmission spectroscopy. However, for every spectroscopic instrument a detailed analysis of the noise contributions, an estimation of the achievable extinction ratio, and an evaluation of the available input power is necessary to decide whether the sensitivity improvement due to optical subtraction prevails the additional complication of the setup.

### 4.2.2 Differential vs. direct measurements in field-resolved, time-domain spectroscopy

In the time-domain approach described in Chapter 3 the conditions for the detection of small concentrations of molecules differ from those in time-integrating, frequency-domain spectroscopy. In contrast to frequency-domain (including FTIR) spectroscopy, the detection with electro-optic sampling allows to record the electric field of the resonant sample response isolated from the noisy excitation in a time window which is dominated by gate pulse shot-noise. Here, a numerical model to estimate the time-dependent signal-to-noise ratio in quasi background-free electric-field-resolved spectroscopy comparing the direct and the differential approach is developed.

To this end, we utilized the EOS measurement of the MIR waveform shown in Fig.(3.11a)

as excitation pulse and simulated the interaction of its electric field with sample and reference molecules by a set of Lorentzian oscillators. In the time domain, this is represented by the superposition of the instantaneous and the phase-shifted resonant molecular response. The former was neglected in this context because it is very small compared to the intensity noise of the excitation pulse. The latter was described by a Lorentzian-shaped absorption band with a peak absorption  $\alpha$  and an effective dephasing time  $T_2$ . The effective dephasing time  $T_2$  is connected to the full-width-at-half-depth line width  $\delta\nu$  in the frequency-domain by  $T_2 = (\pi\delta\nu c)^{-1}$  with the speed of light  $c$  [33].

For the sample molecules we assumed a line width of  $13.47\text{ cm}^{-1}$  and a central frequency of  $1139\text{ cm}^{-1}$  which corresponds to the major absorption line of  $\text{DMSO}_2$  molecules solved in water within the spectral coverage of the excitation [36]. For the reference molecules we considered a set of six Lorentzian oscillators with central frequencies between  $1323\text{ cm}^{-1}$  and  $1724\text{ cm}^{-1}$  and line widths between  $36\text{ cm}^{-1}$  and  $80\text{ cm}^{-1}$ . In the described model, this combination of Lorentzian oscillators represents a typical organic substance surrounding the  $\text{DMSO}_2$  molecules and contributing to a strong molecular background signal. This is a purely qualitative approach because exact quantitative modelling of a surrounding substance is computationally intensive and does not affect the qualitative outcome of the presented proof-of-concept study. The mean absorption of the Lorentzian oscillators constituting the molecular background was  $75\text{ cm}^{-1}$  in a  $30\text{ }\mu\text{m}$  thick sample cuvette. The absorption of the low-abundant  $\text{DMSO}_2$  molecules was a factor of 100 weaker. In the following, we refer to the combination of sample and reference molecules in a  $30\text{ }\mu\text{m}$  thick measurement volume as sample cuvette and to the reference molecules alone as reference cuvette.

Fig.(4.3a) illustrates the direct measurement configuration, i.e. the propagation of the excitation pulse through the sample cuvette. The electric field which is coherently emitted by the molecules in the sample after excitation is magnified in the sketch for better visibility. Fig.(4.3b) illustrates the differential configuration, where the excitation pulse is split into two copies. One of the copies passes through the reference cuvette and the other one passes through the sample cuvette. Afterwards both copies are destructively recombined to isolate the coherently emitted electric field of the molecules of interest. Fig.(4.3c) and (d) show the numerical results for the direct and the differential configuration, respectively. The blue curves correspond to the envelope of the measured EOS signal normalized to the peak of the excitation pulse. In Fig.(4.3d) the difference of the electric fields of the excitation pulse after interaction with the Lorentzian oscillators in the sample cuvette and the reference cuvette, i.e. the measured EOS signal in the differential configuration, is shown. The red line denotes the instantaneous response of the molecules which is identical to the excitation pulse in our model. For comparison, the purely resonant response of the  $\text{DMSO}_2$  molecules is depicted in green. Compared to the direct configuration, the amplitude of the differential excitation pulse is reduced by the interferometer losses. Here, we assumed a splitting ratio of 50:50 at the beam splitter and beam combiner, respectively and an AR coating with broadband transmission of 0.95. Consequently, the resonant response of the  $\text{DMSO}_2$  molecules, i.e. the sought-for signal, is reduced by the same factor in the differential

configuration. To account for the imperfect extinction of interferometric subtraction, the amplitude of the excitation pulse was reduced for the interaction with the sample cuvette molecules by an imbalance factor  $\sqrt{4\Delta}$  as described in the previous section.

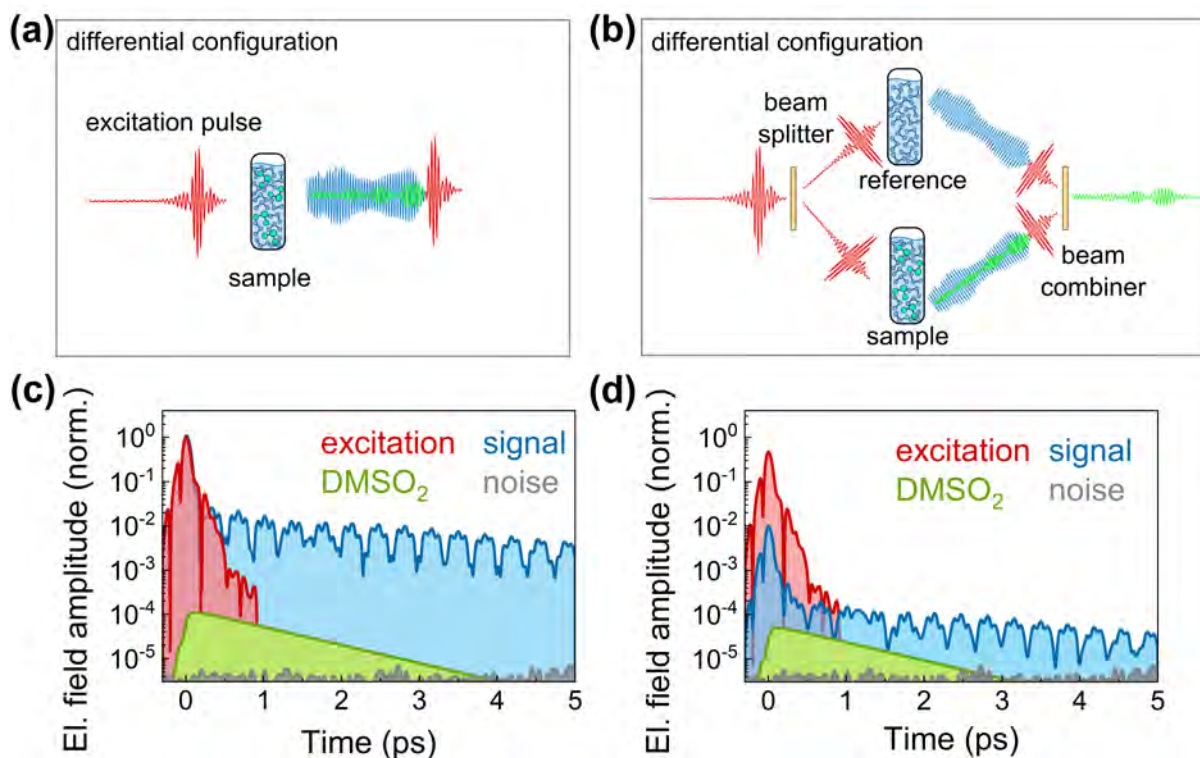


**Figure 4.3:** **a)** Sketch of the direct configuration. **b)** Sketch of the differential configuration. The coherently emitted electric field of the excited molecules is magnified for better visibility. **c)** Numerical results of simulation of the excitation pulse interaction with DMSO<sub>2</sub> molecules embedded in a cluster of high abundant resonant molecules. The green curve denotes the resonant response of the DMSO<sub>2</sub> molecules alone. **d)** Numerical results for the differential signal simulated as difference of the electric fields of the excitation pulse after interaction with a cluster of highly abundant resonant molecules with and without DMSO<sub>2</sub> molecules. The imperfect extinction of interferometric subtraction is considered as slight imbalance in the excitation pulse amplitude. Compared to the direct signal in part (a) the excitation pulse is reduced by the interferometer losses.

The comparison of Fig.(4.3a) and (4.3b) reveals that the excitation pulse as well as the background from surrounding molecules in the differential measurement is reduced depending on the extinction ratio. This results in a proportional suppression of intensity fluctuations. In both configurations, however, the ultimate noise limit for EOS detection is given by the quantum efficiency of the nonlinear up-conversion and the shot-noise of the gate pulse and is therefore identical. The magnitude of the ultimate noise level shown in grey was obtained by an array of randomly distributed numbers (white noise) with an rms amplitude of the inverse dynamic range of  $5.5 \times 10^5$  (see Fig.(2.15b), note that the DR in

electric field scales with the square root of the DR in intensity).

To examine the influence of intensity noise suppression in optical subtraction on the time-dependent signal-to-noise ratio of gate-pulse-shot-noise-dominated field-resolved detection, we defined the signal and the noise amplitude for the direct and the differential configuration according to the previous section. The signal amplitude attributed solely to the resonant response of the DMSO<sub>2</sub> molecules was obtained by subtracting the background signal, i.e. the signal without DMSO<sub>2</sub> molecules from the measured signal as described in Eqn.(4.2) and Eqn.(4.6), respectively. However, to account for field-resolved detection we rewrite these equations using the equality  $E = c\sqrt{P}$  with the proportionality constant  $c$  which yields

$$E_{M,dir} = E_0 \left(1 - e^{-A/2}\right), \quad (4.10)$$

for the direct configuration and

$$E_{M,diff} = E_0 (1 - \delta) \left(1 - e^{-A/2}\right), \quad (4.11)$$

for the differential configuration. The noise amplitude is defined as the difference of two reference traces. In the direct measurement, amplitude fluctuations of the exciting waveform are the dominant source of noise. To model these fluctuations, the excitation pulse amplitude was modulated with two different arrays of randomly distributed numbers with an rms amplitude which corresponds to the integrated intensity noise of the MIR radiation (see Section 3.2.2). This resembles the experimental situation of two subsequent excitation pulses. Each pulse interacted with the Lorentzian oscillators in the reference cuvette and the difference of the resulting traces revealed the time-dependent noise amplitude for the direct configuration.

In the differential measurement, the crucial parameter is the extinction ratio. The amplitude fluctuations of the excitation pulse within one measurement are suppressed due to interferometric subtraction. Compared to the direct configuration, the noise in the differential configuration is reduced by the imbalance factor  $\delta$  as described above.

The resulting signal-to-noise ratio is shown in Fig.(4.4) for the direct and the differential configuration. The simulated integrated RIN of the excitation pulse matches the measured value of 0.07%. The shaded yellow area denotes the SNR values below unity where the signal would drown in noise in the experiment. In Fig.(4.4a) the extinction ratio is scaled between  $10^{-5}$  and  $10^{-3}$ . For all considered extinction ratios the SNR rises faster above unity and reaches higher values than in the direct configuration for almost the entire time window. Beyond 0.5 ps, the direct SNR curve shows strong modulations which are attributed to the beating of the molecular background signal (compare Fig.(4.3)). This beating results in dips in the amplitude of the molecular background signal and therefore in the absolute RIN and generates spikes in the SNR curve. This behaviour shows that in the direct configuration the SNR is dominated by the amplitude fluctuations of the molecular background. The fact that the spikes in the direct SNR lie above the differential SNR for some cases indicates that if the gate pulse shot noise becomes dominant the SNR

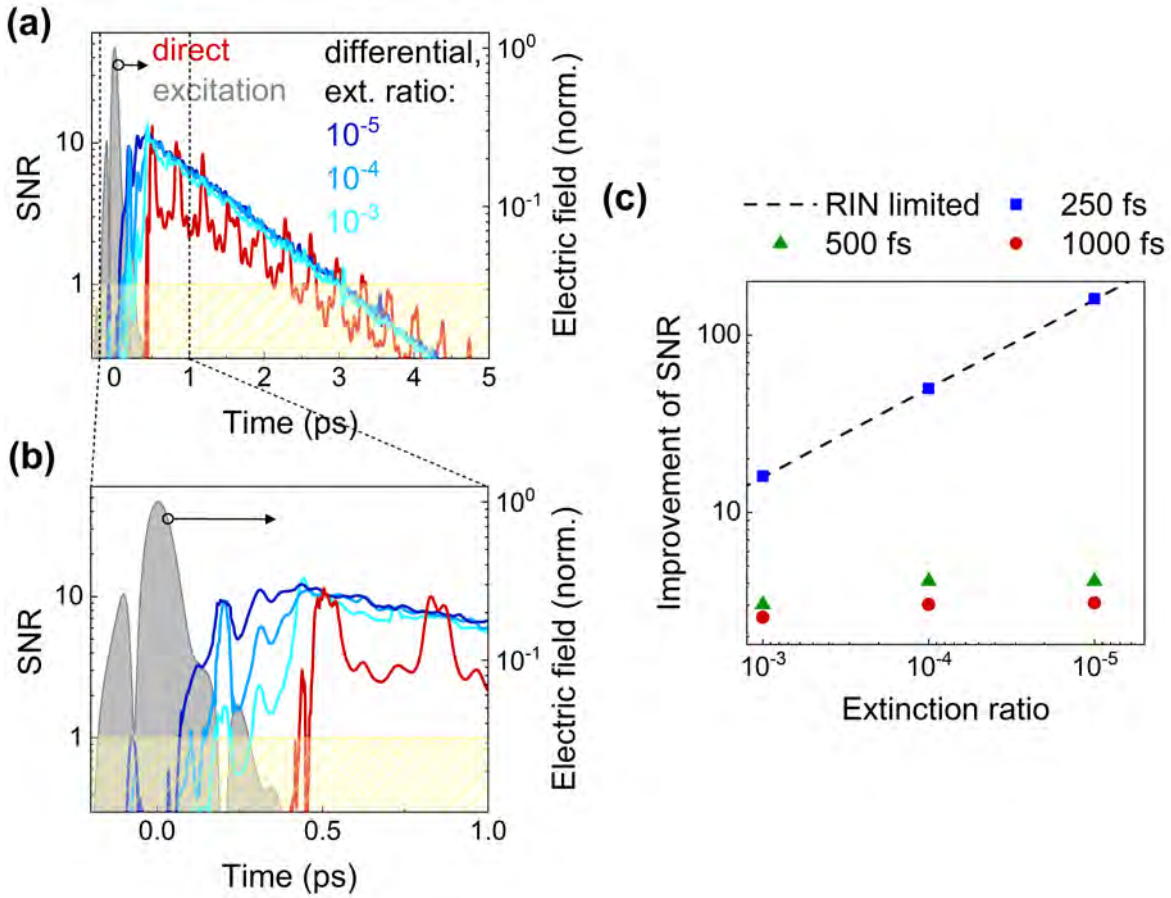


**Figure 4.4:** Simulation of electric-field-resolved direct and differential signal-to-noise ratio for an integrated RIN of the excitation of 0.07 %. **a)** In the shaded yellow area noise covers the signal. As a reference for the eye, the excitation pulse is shown in grey. The interferometric extinction ratio in the differential configuration is scaled between  $10^{-5}$  and  $10^{-3}$ . **b)** Close-up of (a). **c)** Improvement in SNR comparing direct and differential configuration for the considered extinction ratios. The blue squares, the green triangles, and the red dots correspond to the simulated improvement factor evaluated at 250 fs, 600 fs, and 1 ps, respectively. The black dashed line indicates the theoretical improvement factor enabled by suppression of intensity noise in the differential configuration if gate pulse shot noise is omitted.

in the direct case can reach higher values than in the differential case due to interferometer losses. For an extinction ratio of  $10^{-4}$  and  $10^{-5}$  the SNR curves beyond 0.5 ps are similar and unmodulated. The reason is that fluctuations of the excitation pulse amplitude and therefore fluctuations of the molecular background are almost entirely suppressed already at an extinction ratio of  $10^{-4}$  and the flat ultimate noise limit dominated by gate pulse shot noise prevails over almost the full time window. For an extinction ratio of  $10^{-3}$  the modulations of the SNR curve beyond 0.5 ps, i.e. the influence of excitation pulse

amplitude fluctuations, are strongly suppressed. As the close-up to the first picosecond shown in Fig.(4.4b) illustrates, the main improvement due to a better extinction ratio is that the SNR rises faster above unity and reaches its maximum earlier.

Fig.(4.4c) illustrates the improvement in SNR between direct and differential configuration for the considered extinction ratios. The blue squares, the green triangles, and the red dots correspond to the simulated improvement factor evaluated at 250 fs, 600 fs and 1 ps. The black dashed line indicates the theoretical improvement factor enabled by suppression of intensity noise if gate pulse shot noise is omitted. The improvement factor at 250 fs coincides with the black dashed line for all considered extinction ratios because at this point RIN is the dominant source of noise for all configurations and gate pulse shot noise can be neglected. At 600 fs and 1 ps the improvement factor deviates from the black dashed line and the simulated SNR improvement stagnates for extinction ratios better than  $10^{-3}$  which can be explained by the dominating gate pulse shot noise for these parameters. If the gate pulse shot noise cannot be neglected the improvement factor is reduced by the interferometer losses which limit the ultimate differential SNR to a lower level than the ultimate direct SNR. Further improving the extinction ratio can only result in a better SNR if RIN is the dominant source of noise. To exploit the full potential of differential molecular fingerprinting enabled by a better extinction ratio the excitation pulse amplitude has to be scaled accordingly. The difference between the improvement factors at 600 fs and 1 ps is caused by the difference in decay time between the signal of interest and the molecular background chosen in the simulation.

For the experimental realization of differential molecular fingerprinting, besides the extinction ratio the stability of the destructive interference must be evaluated and if necessary actively controlled in order not to introduce an additional source of noise.

In conclusion, the simulation of the time-dependent SNR revealed that optical subtraction helps to increase the sensitivity of quasi background-free time-resolved spectroscopy. The optical-subtraction-induced suppression of the intensity fluctuations of the excitation and the molecular background increases the SNR of detecting small concentration changes in complex molecular consortia (here simulated by adding DMSO). The advancement is particularly large shortly after the peak of the excitation, where the intensity noise of the overall signal (excitation and molecular background) substantially exceeds the detection noise, i.e. at  $t < t_B$ . Optical subtraction effectively shifts  $t_B$  closer to the peak of the excitation, allowing background-free detection of sought-after coherent molecular signals, where they are strongest, right after their initiation. For increasing MIR excitation power,  $t_B$  tends to shift to ever later times (for otherwise unchanged excitation pulse properties), allowing optical subtraction to broaden the window of background-free detection ever more substantially. In addition, for higher excitation powers, the increasing laser spot size on the EOS crystal (in order to avoid optical damage) provides ever greater room for enhancing the electric field strength of the sought-after molecular signal on the detector by focusing the beam more tightly following optical subtraction which prevents the high fields of the excitation pulse from hitting the crystal. As a consequence, optical subtraction is expected

to increasingly improve the sensitivity of field-resolved infrared spectroscopy for ever higher excitation powers.

### 4.3 Mach-Zehnder-type deep nulling interferometer

The theoretical study on the sensitivity improvement helps to estimate the required experimental performance of an achromatic interferometer necessary to successfully implement broadband optical subtraction. The challenge of interferometric, optical subtraction for application in broadband frequency-domain and ultrafast, time-domain spectroscopy is to simultaneously cancel all wavelength components of an often super-octave spectrum. In classical interferometry, a phase shift between the two arms of an interferometer is achieved by introducing a length change  $\Delta l$  in one interferometer arm to yield a phase shift  $\Delta\phi$ :

$$\Delta\phi = 2\pi \frac{\Delta l}{\lambda} \quad (4.12)$$

This equation shows that a phase shift due to mutual delaying always depends on the wavelength  $\lambda$ . Broadband optical subtraction however, requires a wavelength-independent phase shift of  $\pi$  for achromatic destructive interference between the electric field from the reference and the sample arm. Our solution for an achromatic phase shift of  $\pi$  based on a Mach-Zehnder-type interferometer can be adapted for radiation spanning from the visible to the far infrared spectral region.

#### 4.3.1 Achromatic phase shift of $\pi$

In the field of observational astronomy, the idea of interferometric nulling to detect faint extrasolar planets in front of bright stars [104] arose in 1978. Since then, several solutions for achromatic phase shifting were realized [105]. A geometrical phase shift of  $\pi$  can be achieved by employing mirror-symmetric periscopes in the two arms of the interferometer, respectively [106]. The Gouy phase shift occurring in the propagation of a focused beam can be exploited for achromatic deep nulling by introducing an additional focus in one arm of the interferometer [107]. Another concept consists of a pair of Fresnel rhombs acting as achromatic quarter wave plate inside each interferometer arm [108]. By rotating the Fresnel rhombs in one arm of the interferometer by  $45^\circ$  with respect to the polarization of the incident light and in the other arm by  $-45^\circ$ , an achromatic phase shift of  $\pi$  is produced. All the described concepts are either technically challenging, costly or not suitable for ultrashort laser pulses.

A simpler approach was realized by Hayden et al. [109] for spectral absorption and dispersion measurements of liquid samples with a tunable narrowband laser. We adapted this Mach-Zehnder-type approach for broadband optical subtraction enabling the spatial separation of the sought-for sample response from the exciting light pulse and the molecular background.

Light waves experience an achromatic phase shift of  $\pi$  when they are reflected off a boundary to a medium with higher refractive index. However, when the reflection happens at a boundary to a medium with lower refractive index the phase is unaffected. This fundamental property of light waves is exploited in a classical Mach-Zehnder interferometer by orienting the beam splitter and beam combiner accordingly. In the standard geometry, the light travelling to the constructive port of the interferometer is transmitted once and reflected once by the beam splitter or beam combiner, respectively in each arm of the interferometer. Consequently, light entering the destructive port of the interferometer experiences an unequal number of reflections and transmissions in each interferometer arm leading to an intensity imbalance for unequal splitting ratios. This is especially important for broadband radiation where the splitting ratio varies across the spectral bandwidth which in turn results in a wavelength-dependent interferometer.

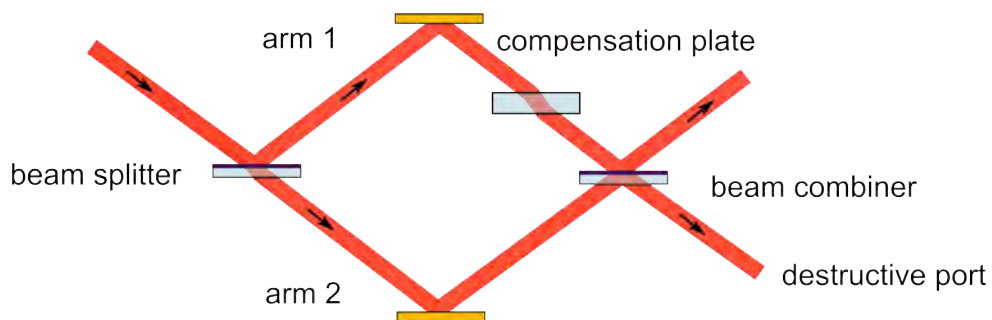


**Figure 4.5:** Broadband interferometric subtraction in a Mach-Zehnder-type interferometer. In arm 1 the beam is reflected off the first surface of the beam splitter whereas in arm 2 the beam is reflected off the second surface of the beam combiner leading to an achromatic phase shift of  $\pi$  in the destructive port of the interferometer. To compensate for the additional material passage a plate twice as thick as the beam splitter is introduced in arm 1.

To avoid intensity imbalances we combined an equal number of reflections and transmissions in each arm in the destructive port of the interferometer shown in Fig.(4.5) [110]. Here, the interfering light in the upper port has opposing phase because it is reflected off the first surface of the beam splitter in arm 1 and off the second surface of the beam combiner in arm 2. By adding a compensation plate in arm 1 which is exactly twice as thick as the beam splitter, we equalized the number of transmissions and reflections and the material passage in the two arms.

For beam splitting and combination we used the Fresnel reflection off uncoated surfaces to avoid bandwidth limitations and undesired inequalities between the two interferometer arms due to a coating. Therefore, the splitting ratio is defined by the refractive index of the beam splitter material, the angle of incidence, and the polarization of the incident light. The intensity  $I_1$  from one arm reaching the destructive port of the interferometer

when the other arm is blocked is given by:

$$I_1 = I_2 = I_0 T^4 R, \quad (4.13)$$

where  $I_0$  is the intensity incident on the interferometer,  $R$  is the reflectivity, and  $T$  is the transmission at the beam splitter and combiner, respectively. Assuming there is no absorption one can substitute  $R = 1 - T$  in Eqn.(4.13) and calculate that  $I_1$  and  $I_2$  are maximized for  $T = 0.8$  and  $R = 0.2$ . Together with the Fresnel equations, one can find the optimum angle of incidence for given incident light and material to increase the sought-for difference signal.

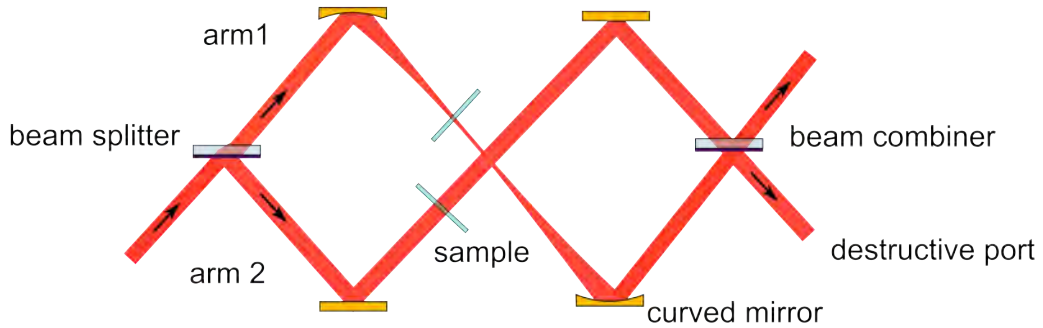


**Figure 4.6:** Broadband interferometric subtraction for spatial separation of linear and nonlinear response. An achromatic phase shift of  $\pi$  is achieved through the Gouy phase shift due to the additional focus in one interferometer arm. In each arm an identical sample is placed in the focus and the collimated beam, respectively.

With a slight adaptation, this interferometer can, in principle, be employed to isolate the nonlinear from the linear polarization response of a sample. As discussed in Chapter 2 the nonlinear polarization response of matter is usually orders of magnitude smaller than the linear one and can only be accessed by sufficiently high intensities. For example in attosecond polarization spectroscopy [111], a reference measurement with significantly reduced intensity is scaled and subtracted numerically from a measurement with intensity high enough to provoke nonlinear effects to isolate the nonlinear response.

In the modified interferometer geometry shown in Fig.(4.6), the achromatic phase shift of  $\pi$  between the two arms is caused by the Gouy-phase introduced by an additional focus in one arm 1. Thus, the compensation plate becomes unnecessary because the symmetric port of the interferometer where each arm is reflected and transmitted once contains the difference signal. One of the identical samples in the two arms is placed in or close to the focal plane of the curved mirror. The second curved mirror is utilized to mode match the two arms after recombination. By choosing the input power and beam waist, as well as the focal length of the curved mirrors such that only in the focal plane the intensity is sufficiently high to introduce a nonlinear polarization response in the sample, one can

optically subtract the linear response and directly access the pure nonlinear response in the experiment.

### 4.3.2 Theoretical limitation of the extinction ratio

The significant parameter for broadband optical subtraction is the extinction ratio, i.e. the ratio of the intensity in the constructive and destructive interference port. It is a measure for the quality of the intensity suppression usually integrated across the spectral bandwidth of the incident light source. This quantity can be influenced by different factors including spatial misalignment of optical elements inside the interferometer, thickness mismatch and surface quality of the beam splitter, beam combiner and compensation plate substrates, depolarization effects, and intensity imbalances. To estimate the theoretical limit of the extinction ratio and to quantify the influence of different parameters we modelled different scenarios.

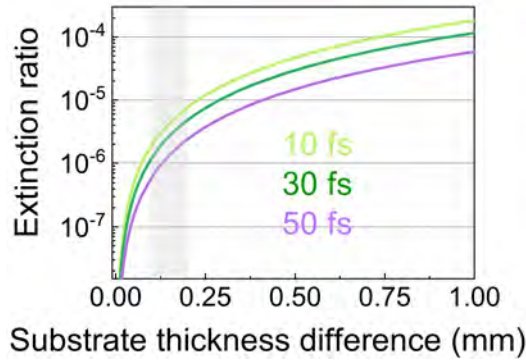


**Figure 4.7:** Calculated extinction ratio for increasing substrate thickness mismatch between the transmissive components inside the interferometer for different input pulse length. The shaded grey area denotes the thickness tolerances specified by different manufacturers.

First, we analyzed the influence of thickness mismatch between the transmissive optics in the two interferometer arms on the extinction ratio in terms of dispersion. To this end, we simulated the propagation of FT-limited Gaussian pulses with durations between 10 fs and 50 fs and a central wavelength of 1.5  $\mu\text{m}$  inside the interferometer by dispersing their electric field in one arm by 9 mm borosilicate crown glass (N-BK7) and in the other arm by 9 mm N-BK7 and additional substrate thickness mismatch. The extinction ratio is given by the intensity of the difference of the calculated electric fields and the intensity of their sum. Fig.(4.7) shows that the influence of thickness mismatch on the extinction ratio increases with shorter pulse durations. The shaded grey area in Fig.(4.7) denotes the range of thickness tolerances specified by different suppliers of N-BK7. In the worst case, the thickness deviations of the different transmissive elements add up to 0.6 mm in this example and the extinction ratio is limited to  $7 \times 10^{-5}$  for pulses with a duration of 10

fs. For other materials than N-BK7 the manufacturing tolerances and the dispersion can differ. However, the presented estimation illustrates how critical the substrate thickness is for a good extinction ratio.

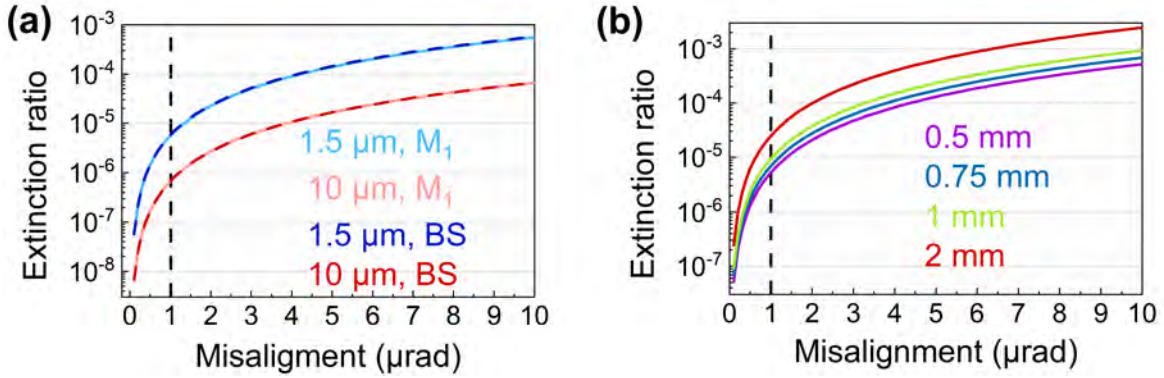


**Figure 4.8:** Calculated extinction ratio for increasing angular misalignment of the optical elements inside the interferometer. The shaded black line denotes the alignment precision of commercial kinematic mounts. **a)** Influence of the central wavelength for angular misalignment of the mirror  $M_1$  in arm 1 and the beam splitter BS. **b)** Influence of the incident beam waist (radius at FWHM) at a central wavelength of  $1.5 \mu\text{m}$ .

Besides slightly different transmissive optics in the two interferometer arms, misalignment of the optical components leads to imperfect spatial overlap of the interfering beams and therefore influences the extinction ratio. Ideally, all surfaces of the optical elements should be parallel to each other to guarantee spatial overlap of the interfering beams and an identical angle of incidence on the transmissive elements for intensity and dispersion matching. To quantify the influence of angular misalignment of optical elements, we built a geometrical optics model of the interferometer shown in Fig.(4.5) using ray transfer matrix analysis. By extending the ABCD-matrices representing the optical elements to  $3 \times 3$ -matrices we introduced a small angular misalignment [112]. The overlap integral of the interfering Gaussian beams for a certain angular misalignment normalized to the overlap integral of the interfering Gaussian beams without misalignment, i.e. two perfectly overlapping Gaussian beams [113] yields the extinction ratio given by its deviation from unity. This model includes only the influence of misalignment on the spatial overlap and neglects correlated intensity and dispersion imbalances.

Fig.(4.8a) shows the calculated extinction ratio for an interferometer arm length of 30 cm, an incident beam waist of 0.6 mm (radius at FWHM), and a central wavelength of  $1.5 \mu\text{m}$  and  $10 \mu\text{m}$ , respectively, for increasing angular misalignment. Here,  $M_1$  denotes the mirror in arm 1 and BS denotes the beam splitter. As Fig.(4.8a) shows, misalignment of different optical elements has the same quantitative influence on the extinction ratio. The alignment sensitivity decreases noticeably for increasing wavelength. Fig.(4.8b) illustrates that the alignment sensitivity increases with the incident beam waist (radius at FWHM,

centralwavelength 1.5  $\mu\text{m}$ ). The simulations also corroborate the expectation that a shorter interferometer arm length is beneficial for the alignment sensitivity.

Commercially available motorized kinematic mirror mounts have an alignment precision of 1  $\mu\text{rad}$  as denoted by the dashed black line in Fig.(4.8a) and (b). For different central wavelengths and incident beam waists, this alignment precision allows for an extinction ratio between  $6 \times 10^{-7}$  and  $2 \times 10^{-5}$  if only the spatial overlap is considered.

For a precise calculation of the expected extinction ratio for given experimental parameters a more comprehensive numerical model is necessary, combining the discussed influence factors and including beam front distortion and depolarization effects. However, to classify the experimental results, the presented values and tendencies are a good indicator.

### 4.3.3 Broadband optical subtraction in the near-infrared

To test the concept of the Mach-Zehnder-type interferometer for broadband optical subtraction, we set up a proof-of-principle experiment using a super-octave near-infrared light source. From a practical point of view, it is more convenient to begin with a near-infrared light source because the necessary diagnostic tools like high resolution beam profiler, high dynamic range spectrometer, fluorescent cards, and also high quality beam splitter substrates are readily available. The employed light source is based on a commercial Er: fiber oscillator (Menlo C-fiber femtosecond erbium laser at 56 MHz) delivering 300 mW of output power at 1.55  $\mu\text{m}$  central wavelength. The 90-fs output pulses were further spectrally broadened and compressed in a highly nonlinear fiber assembly<sup>1</sup> [98]. The broadened spectrum is shown in Fig.(4.9a) and spans from 950 nm to 2100 nm at a -30 dB level. A FROG measurement of the temporally compressed pulses employing a 10  $\mu\text{m}$  thick BBO crystal for SHG reveals the temporal intensity profile shown in Fig.(4.9b) with a pulse duration of 11 fs at FWHM and an average power of 175 mW.

For beam splitting and combining we used 3-mm thick, plane N-BK7 substrates and a 6-mm thick N-BK7 substrate as compensation plate. The high surface quality ( $\lambda/10$ ), small thickness tolerance ( $\pm 0.1$  mm), and good parallelism ( $\pm 30$  arcsec) of these substrates is beneficial for a high extinction ratio. At  $60^\circ$  angle of incidence, the uncoated N-BK7 surfaces provide a reflectivity of 0.2 for s-polarized light at 1.55  $\mu\text{m}$ . This agrees with the splitting ratio for maximized differential signal discussed in Section 4.3.1. Together with the substrate thickness of 3 mm, this results in a sufficient spatial separation between the reflection off the first and the second surface to spatially filter undesired multiple reflections.

Fig.(4.9c) shows a sketch of the interferometric setup including diagnostics and an active feed-back loop for arm length stabilization. To this end, an auxiliary CW laser was coupled into the interferometer slightly separated from the main beam in height. At the constructive port of the interferometer, the CW laser propagates through an ellipsometer

<sup>1</sup>The highly nonlinear fiber assembly was designed and provided by the group of Prof. Dr. Alfred Leitenstorfer at the University of Konstanz.

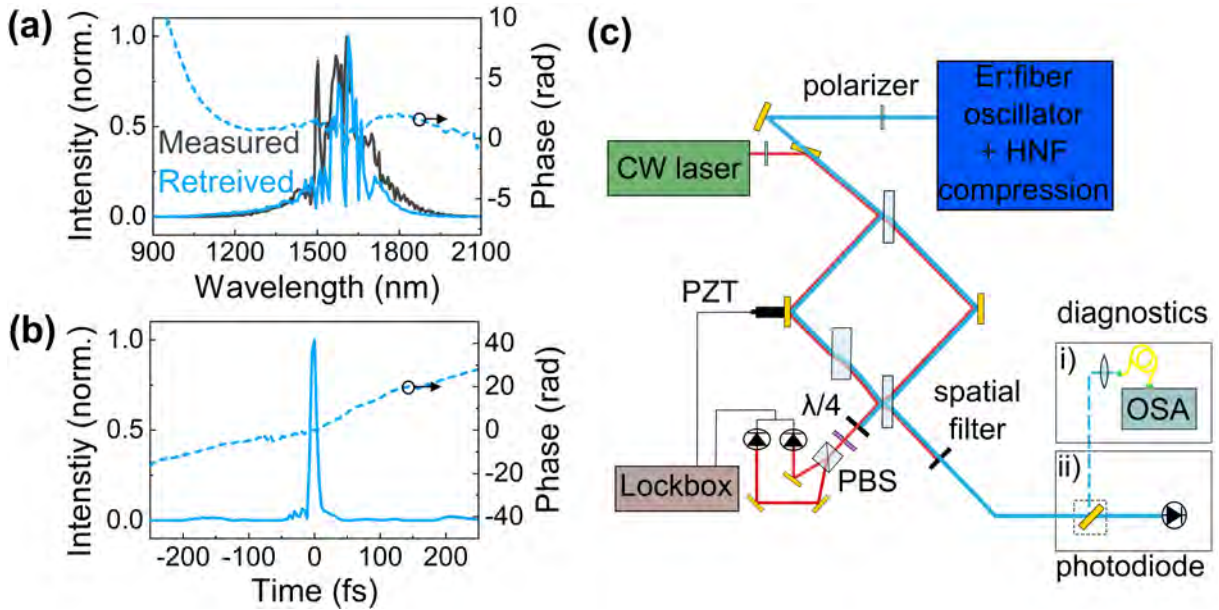


**Figure 4.9:** Characterization of the input pulses to the interferometer generated by a commercial Er: fiber laser with subsequent nonlinear compression. **a)** Comparison of the measured spectrum and the spectrum retrieved from a FROG measurement. The dashed line denotes the retrieved spectral phase. **b)** Retrieved temporal intensity profile and temporal phase. **c)** Sketch of the Mach-Zehnder-type interferometric setup for broadband optical subtraction including diagnostics and active arm length stabilization. PZT: piezo-electric transducer,  $\lambda/4$ : quarter wave plate, PBS: polarizing beam splitter, OSA: optical spectrum analyzer.

consisting of a QWP and a polarizing beam splitter cube to generate a Hänsch-Couillaud error signal [114] on a balanced photodiode. The input polarization of the auxiliary laser was chosen to be linear with  $45^\circ$  rotation with respect to the propagation plane, so that light travelling to the constructive port of the interferometer acquires a different amount of polarization rotation in each arm, respectively, due to the unequal number of reflections and transmissions. Thus, the generated error signal is zero if both interferometer arms have the same optical path length and changes proportionally to the sign and magnitude of any deviation from this zero delay position. The error signal was connected to a PI<sup>2</sup>D controller which activates a PZT acting on the length of one interferometer arm. This active feed-back loop allowed to reduce intensity fluctuations of the destructive interference owing to deviations from the zero delay position. Beam pointing fluctuations of the incoming light beam are strongly suppressed in the interference signal due to the symmetry of the interferometric setup.

The performance of the interferometer was characterized by recording the interference signal at the destructive port with a photodiode while applying a saw-tooth voltage to the PZT acting on the optical path length. To ensure a linear response of the photodiode,

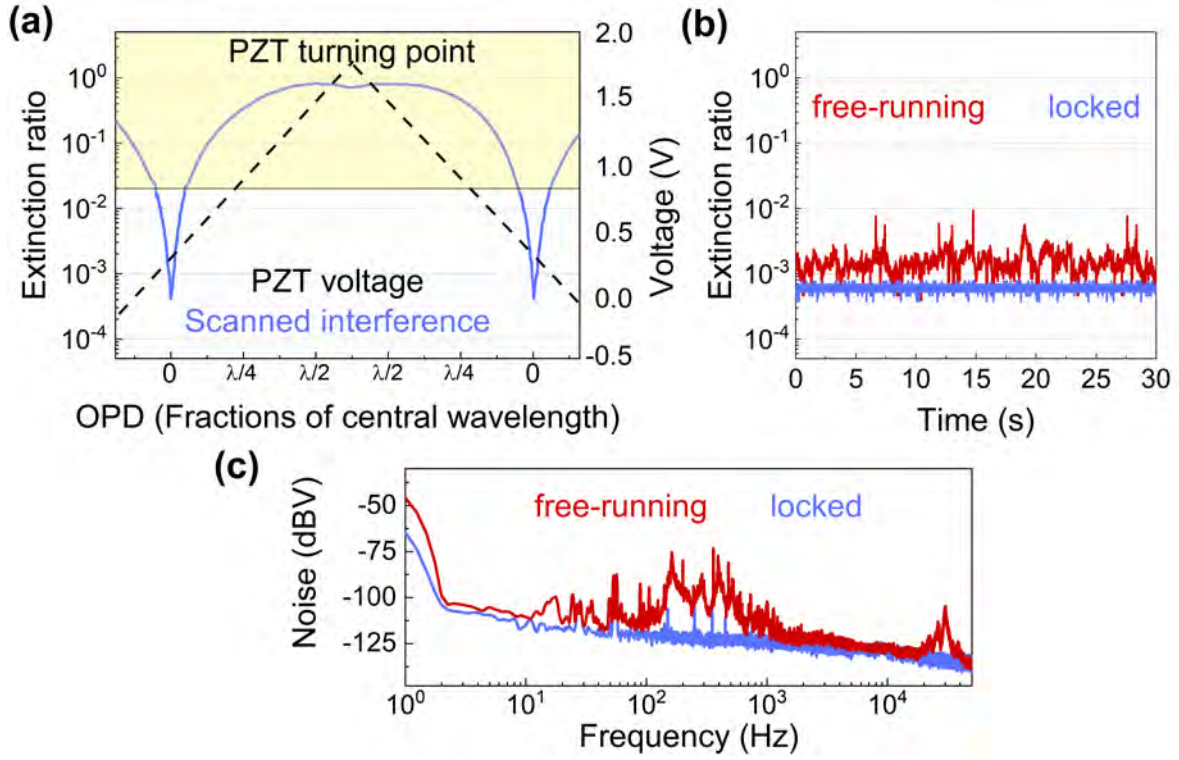


**Figure 4.10:** Characterization of the extinction ratio. **a)** Destructive interference recorded with a photodiode while a saw tooth voltage applied to the piezo electric transducer scanned the interferometer length across the zero delay point. The shaded area denotes the signal amplitude where a neutral density filter was applied to avoid saturation of the photodiode. **b)** Destructive interference recorded with a photodiode with and without active interferometer length stabilization. **c)** Frequency-resolved measurement of the intensity fluctuations in the destructive port of the interferometer measured with an RF analyzer with and without active interferometer length stabilization.

we introduced a calibrated neutral density filter far from the zero delay position. In an ideal interferometer, the interfering light fields  $E_1$  and  $E_2$  are identical and the following equation holds:

$$I_{con} = |E_1 + E_2|^2 = |2E_1|^2 = 4I_1, \quad (4.14)$$

where  $I_{con}$  is the intensity of the ideal constructive interference and  $I_1$  is the intensity reaching the constructive port when one interferometer arm is blocked. To calculate the extinction ratio, we divided the recorded photodiode signal by 4 times the voltage measured when one interferometer arm is blocked. The resulting curve is shown in Fig.(4.10a) and reaches a minimum of  $4 \times 10^{-4}$ . The maximum of the curve does not reach unity because ideal constructive interference cannot be achieved in the port designed for destructive interference. A modification of the optical path difference will always result in a

wavelength-dependent phase difference between the two interferometer arms and therefore imperfect interference.

Fig.(4.10b) compares the extinction ratio recorded over half a minute with and without active length stabilization. The root mean square (RMS) value of the extinction ratio with active interferometer length stabilization is  $6.1 \times 10^{-4}$ . A comparison of the standard deviation of the free-running and the locked extinction ratio reveals a reduction of fluctuations by almost one order of magnitude from  $6.4 \times 10^{-4}$  in the free-running to  $7.2 \times 10^{-5}$  in the locked state. The discrepancy between the rms value of the stabilized extinction ratio and the minimum of the scanned extinction ratio can result from differing air fluctuations and mechanical instabilities in the two arms of the interferometer, which cannot be removed by the 1-dimensional PZT lock.

Fig.(4.10c) shows the frequency-resolved intensity fluctuations in the destructive interferometer port, measured with an RF analyzer with and without active length stabilization. In the free-running case, strong fluctuations were observed between 50 Hz and 1 kHz. These fluctuations correspond to air fluctuations and mechanical resonances within the optical setup. Beyond 1 kHz the fluctuations decrease except for a peak at 30 kHz. This can most likely be attributed to the resonance frequency of the PZT. With the active feed-back loop the fluctuations up to 1 kHz are strongly suppressed.

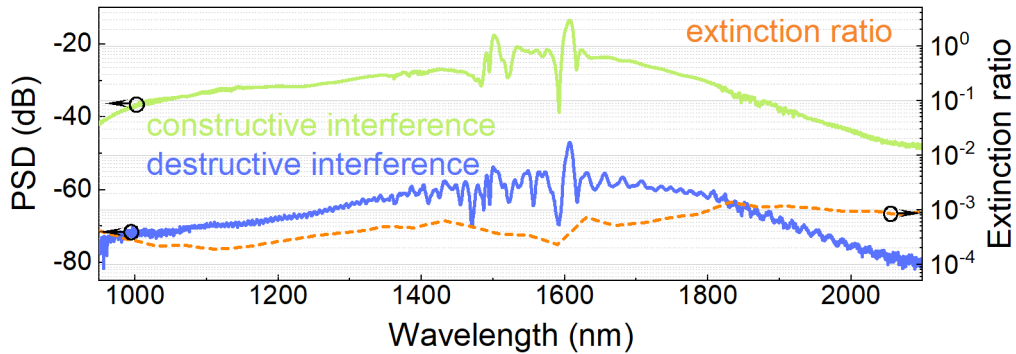


**Figure 4.11:** Characterization of the extinction ratio measured with an optical spectrum analyzer. The ratio of the measured destructive interference spectrum and the constructive interference spectrum yields the frequency-resolved extinction ratio.

To test the achromaticity of our concept for broadband optical subtraction, we characterized the frequency-resolved extinction ratio. Fig.(4.11) shows the power spectral density measured with an optical spectrum analyzer in the destructive port of the interferometer between 950 nm and 2100 nm. The power spectral density of the constructive interference was obtained by blocking one arm of the interferometer and multiplying the recorded curve by a factor of four as described above. The frequency-resolved extinction ratio was calculated by integrating the measured power spectral density in steps of 40 nm and dividing the resultant destructive by the constructive curve. The integration avoids extrema due to non-coinciding modulations in the destructive and constructive power spectral density

stemming from the fact that the signal to noise ratio for the destructive power spectral density is limited by the noise floor of the optical spectrum analyzer. A comparison of the rms value of the spectrally integrated extinction ratio of  $6.1 \times 10^{-4}$  and the spectrally-resolved extinction ratio of  $6.2 \times 10^{-4}$  reveals an excellent agreement. The flatness of the extinction ratio over more than one spectral octave is an evidence for the achromaticity of the introduced phase shift of  $\pi$  and enables the applicability of optical subtraction in a Mach-Zehnder-type interferometer to broadband frequency-domain and ultrafast, time-domain spectroscopy.

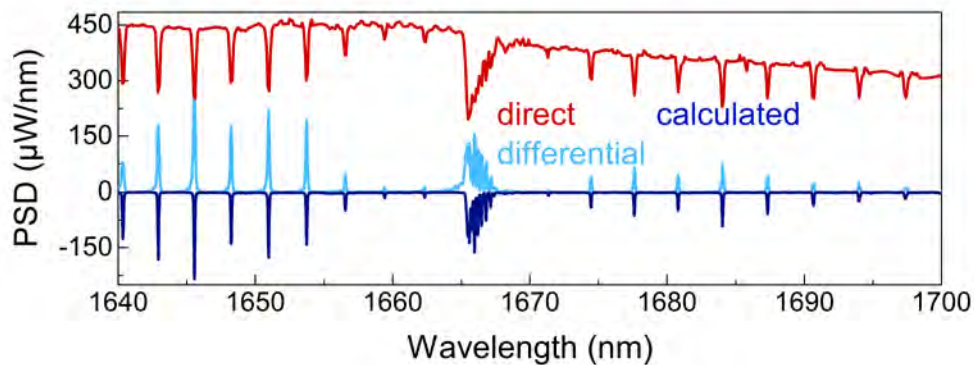


**Figure 4.12:** Methane resonances within the  $2\nu_3$  vibrational overtone band, in direct and differential measurement configuration, at 1 bar. For comparison, the inverted theory curve based on absorbance cross sections from the HITRAN database is shown for the differential measurement.

In a spectroscopic proof-of-principle experiment, we demonstrated the qualitative difference between a traditional absorbance measurement and a measurement employing optical subtraction. Therefore, we placed a 8 cm long gas cell inside one arm of the interferometer and two windows identical to the 1 mm thick FS entrance and exit window of the gas cell in the other arm. In this way, the intensity and dispersion in the two interferometer arms was balanced and the extinction ratio was not noticeably affected. The rudimentary construction and the lack of an accurate pressure gauge did not allow for precise control of the sample gas pressure in the cell. Evacuation of the cell and refilling it with methane up to ambient pressure resulted in an approximate concentration of 1 bar of methane. The difference between the refractive index of methane and ambient air causes a phase shift between the sample arm and the reference arm which was compensated for by readjusting the optical path difference between the two arms.

Fig.(4.12) shows the methane resonances in the  $2\nu_3$  vibrational overtone band within the spectral coverage of the utilized optical spectrum analyzer. For the differential measurement, the interference of reference and sample arm in the destructive interferometer port was recorded. For the direct measurement, the contribution from the reference arm was blocked. Based on methane absorbance cross sections from the HITRAN database [115] we calculated the inverted theory curve shown in dark blue, corresponding to the

differential measurement. The good agreement between theory and experiment proves the quantitative accuracy of the differential method.

In the time-domain picture, the instantaneous response of the methane molecules to an ultrashort excitation pulse is identical to the excitation pulse up to a small fraction of energy transferred to molecular vibrations. Therefore, in the differential measurement the instantaneous molecular response largely cancels upon destructive interference with the excitation pulse from the reference arm. The resulting differential signal mainly contains the resonant molecular response in front of a quasi-zero background. In contrast, the direct measurement reveals the resonant sample response as depletion of the signal at the vibrational resonance frequencies of the molecules (i.e. absorption in the picture of classical spectroscopy) due to destructive interference of the instantaneous and the phase-shifted, resonant sample response [33].

#### 4.3.4 Broadband optical subtraction in the mid-infrared

The successfully demonstrated concept for broadband optical subtraction in a Mach-Zehnder-type interferometer is readily transferable to the mid-infrared spectral region by substituting the N-BK7 beam splitters. Common materials which are transparent in the mid-infrared spectral region and commercially available as windows in optical quality are germanium, silicon, and zinc selenide (ZnSe), amongst others. For our proof-of-concept experiment in the mid-infrared we chose uncoated, 3-mm thick ZnSe substrates for beam splitting and combining and a 6-mm thick ZnSe substrate as compensation plate. Compared to the other materials, ZnSe is also transparent in the visible and near-infrared spectral regions and offers the possibility to use visible alignment lasers. To maximize the differential signal in a more elaborate setup, one could consider broadband AR coatings on one surface of the beam splitter and beam combiner, respectively and on both surfaces of the compensation plate.

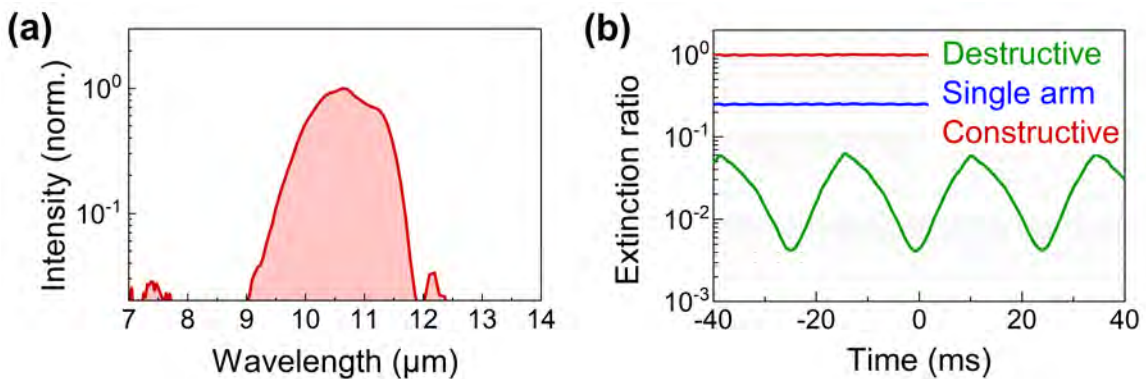


**Figure 4.13:** Broadband optical subtraction in the mid-infrared. **a)** Spectral coverage of the employed mid-infrared light source. **b)** Destructive interference recorded with a MCT detector while a saw tooth voltage applied to the piezo electric transducer periodically scanned the interferometer length across the zero delay point.

For the experiment, we employed a mid-infrared light source based on nonlinear down-conversion of a near-infrared Yb:YAG oscillator which is very similar to the source described in Chapter 3. Fig.(4.13a) shows the spectral coverage of the mid-infrared light source. The experimental setup was equivalent to the setup depicted in Fig.(4.9b). With the help of co-propagating fundamental radiation, the transmissive elements were exchanged by the described ZnSe substrates. We inserted a plano-convex ZnSe lens with a focal length of 500 mm in front of the interferometer to enable spatial filtering of undesired reflections for the six times larger MIR beam waist as compared to the NIR beam.

Fig.(4.13b) shows the destructive interference of the MIR radiation recorded with a liquid-nitrogen-cooled MCT detector while the optical path length difference was periodically scanned across zero. By dividing this curve by four times the value recorded when one interferometer arm was blocked, we calculated the extinction ratio. The curve for the extinction ratio does not reach unity because the range of the PZT is not sufficient to change the optical path difference by  $\lambda/2$  at a central wavelength of 10.5  $\mu\text{m}$ . The longer central wavelength therefore also implies that the extinction ratio is less sensitive to interferometer length fluctuations. The minimum extinction ratio is  $4.2 \times 10^{-3}$ . This value is a factor of 7 higher than the minimum extinction ratio at a central wavelength of 1.55  $\mu\text{m}$  although theory predicts less alignment sensitivity at longer wavelengths. However, the unavoidably larger beam size in the MIR causes the complementary effect. The lack of compact high resolution beam profilers additionally complicates the interferometer alignment in the MIR. Besides these effects, the quality of the available ZnSe substrates is inferior to the N-BK7 substrates used in the NIR. The ZnSe substrates were found to introduce uncorrelated wave front and beam shape distortions leading to a degradation of the extinction ratio. For future experiments, diamond substrates could mitigate this short-coming due to their wide transparency, low dispersion, and high surface quality.

### 4.3.5 Dual-compartment liquid cuvette

Another indispensable component for the application of broadband optical subtraction to spectroscopic experiments is a reference and a sample cuvette. Ideally, two identical cuvettes are placed in the sample and the reference arm of the interferometer without affecting the extinction ratio. A first attempt for a dual-compartment liquid cuvette is depicted in Fig.(4.14a)<sup>2</sup>. It consists of two 1 mm thick rectangular ZnSe windows separated by a  $\sim 30 \mu\text{m}$  thick Teflon gasket. Two square openings in the gasket form two separate liquid compartments each connected to a microfluidic channel. Via two tubes, each compartment can be filled and drained with different fluids independently.

To investigate how similar the two cuvette compartments are, we measured the electric field of a mid-infrared waveform after transmission through one compartment of the liquid cuvette (position A) and the other compartment of the liquid cuvette (position B) with

---

<sup>2</sup>The dual compartment liquid cuvette was designed and produced by our collaborator Gianluca Greci at the National University of Singapore.

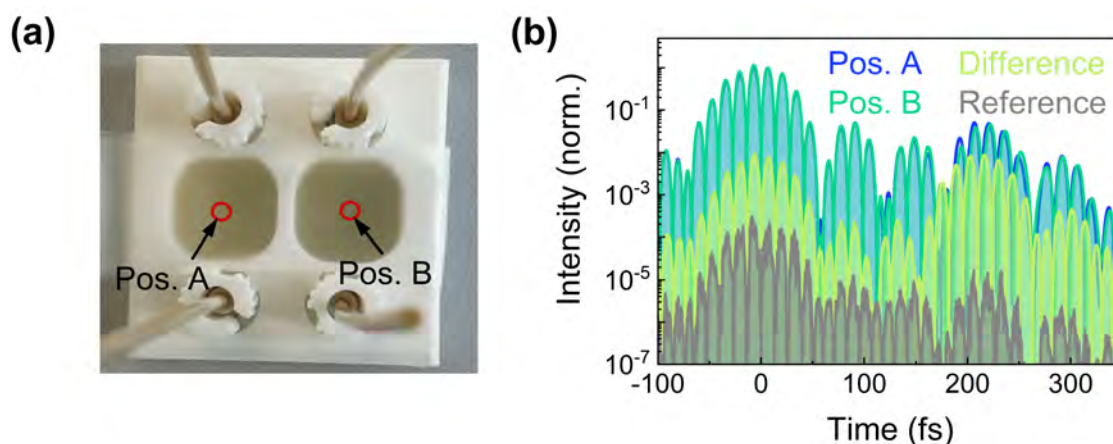


**Figure 4.14:** (a) Dual compartment liquid cuvette designed for optical subtraction in the mid-infrared. (b) Intensity of the EOS signal measured after the mid infrared waveform passed through position A and position B in the empty dual compartment cuvette, respectively. The green line denotes the difference of both measurements. For comparison, the grey line shows the difference of two EOS measurements taken subsequently at the same position in the dual compartment cuvette.

electro-optic sampling. Fig.(4.14b) shows the time-resolved intensity of the mid-infrared waveform for the two measurements. The peak 230 fs after the main pulse corresponds to the back reflection of the MIR pulse inside the empty cuvette. Compared to the measurement at position A, the backreflection in the measurement at position B appears slightly later. The temporal delay of the backreflection corresponds to a compartment cuvette thickness of 34.2  $\mu\text{m}$  at position A and 34.4  $\mu\text{m}$  at position B. The numerical difference of the two measurements shown in green illustrates the resulting problem. The suppression of the back reflection is deteriorated leading to a worse extinction ratio. For comparison, the numerical difference of two subsequent measurements at the same position is shown in grey. The overall better suppression in the difference of two measurements at the same position compared to the difference of the measurement at position A and B indicates that the quality of the first generation dual-compartment cuvette is not sufficient. In the future, additional measures have to be taken to equalize the two compartments.

# Chapter 5

## Energy transfer between molecules and electric fields on a sub-cycle time scale

This chapter describes the application of the developed instrument to study the energy transfer between the electric field of laser pulses and resonant molecules in a time-resolved fashion. Due to the high temporal resolution and sensitivity of the instrument, it is possible to simultaneously observe phenomena on time scales reaching from few femtoseconds to many picoseconds. In the first section of this chapter, the different relaxation channels of linearly excited molecules are discussed and analytic expressions for the totally absorbed and re-emitted energy are derived for the case of an impulsive excitation. The second section of this chapter deals with the measurement of the energy balance of molecules excited by a quasi-impulsive and a dispersive laser pulse. All experimental results are reproduced by an ab-initio quantum chemistry model, providing detailed insight into the dynamics of the light-matter interaction.

### 5.1 Coherent emission of excited molecules

A resonant MIR laser pulse can excite a vibrationally active molecule from its vibrational ground state  $\varepsilon_0$  to the first excited state  $\varepsilon_1$  by absorption of a photon of energy  $\hbar\omega = \varepsilon_1 - \varepsilon_0$ . According to the Boltzmann distribution at room temperature, almost all molecules are in the vibrational ground state because the energy difference  $\varepsilon_1 - \varepsilon_0$  to the first excited state is orders of magnitude larger than  $k_B T$  with the Boltzmann constant  $k_B$  and the temperature  $T$ . The probability of exciting a molecule from the ground state to the first excited state depends on the molecule-specific transition dipole moment. Each vibrationally excited molecule represents an electronic dipole oscillating at the excitation frequency. For an ensemble of excited molecules, the oscillating dipoles constitute a macroscopic polarization which is  $90^\circ$  phase shifted with respect to the exciting light field. This macroscopic polarization is the source of an again  $90^\circ$ -phase-shifted electric field emitted by the excited

molecular ensemble [116].

In an ideal ensemble of molecules, i.e. non-interacting and stationary molecules, the electric field emitted by the molecules would oscillate at constant frequency and decay only due to the finite life time of the excited state which is governed by the Einstein coefficient for spontaneous emission. In the frequency domain the finite excited state lifetime gives rise to the natural line broadening of the considered vibrational transition [117].

In a real gas, the molecules interact with each other and their velocities follow the temperature-dependent Maxwell-Boltzmann distribution. Due to the Doppler effect, the resonance frequency of the moving molecules is shifted depending on their instantaneous velocity. This distribution of resonance frequencies causes the electric field emitted by the molecular ensemble to dephase. In the frequency domain, the Doppler effect causes an inhomogeneous line broadening with a Gaussian profile. Interactions between the molecules in a gas can be classified as elastic or inelastic collisions. In the latter, the collision leads to a radiation-free energy transfer either from the excited molecule to the collision partner in the form of internal energy or to both colliding molecules in the form of kinetic energy. In the former, the varying distance between the interacting molecules effects the energy levels of the excited molecule and therefore its instantaneous emission frequency. For the macroscopic polarization and thus for the electric field emitted by the molecules, this effect causes dephasing. In the frequency domain, both elastic and inelastic collisions lead to pressure-dependent homogeneous line broadening with a Lorentzian profile.

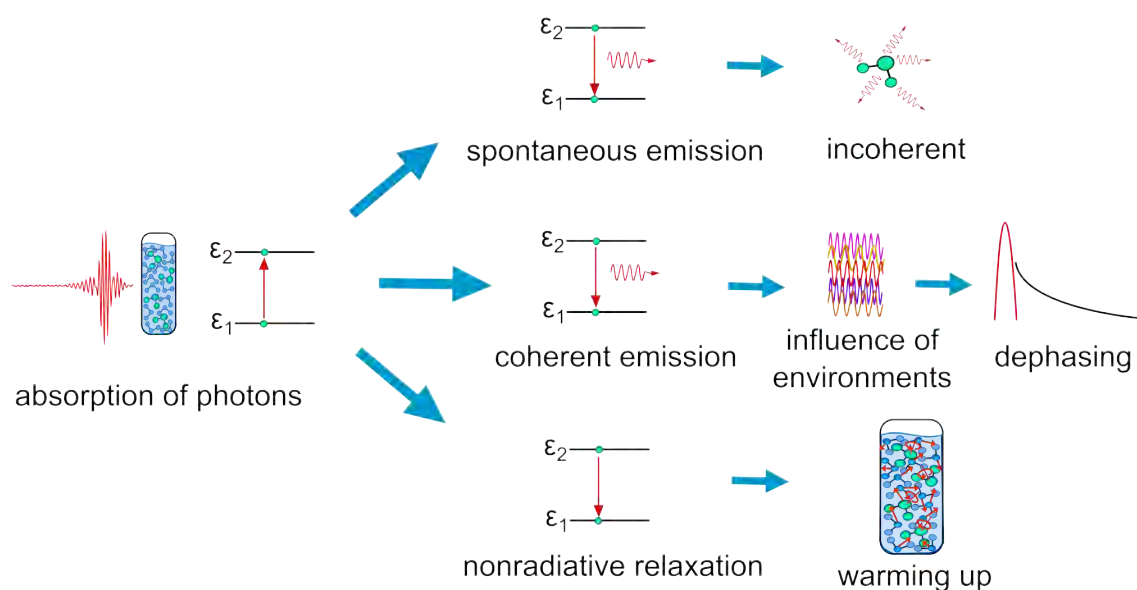


**Figure 5.1:** Sketch of possible energy relaxation channels of vibrationally excited molecules in the liquid phase after interaction with a resonant light field.

In a liquid, the particle density is much higher and the resonantly excited molecules are surrounded by solvent molecules. The instantaneous environment of a molecule at the moment of excitation influences its electronic structure and therefore its energy levels

depending on the polarity of the solvent molecules and possible interactions like hydrogen bonds. The geometrical structure of a molecule can also be influenced by its microscopic environment [118]. If an ensemble of excited molecules with different microscopic environments is considered, the macroscopic electric field emitted by the molecules dephases due to the environment-dependent distribution of resonance frequencies. Thereby averaging over molecules in different environments or averaging over the temporally varying environment of one molecule yields the identical result [116]. In addition, inelastic collisions between the molecules at a higher rate than in less dense gases lead to a nonradiative depopulation of the excited state, i.e. the dissipation of absorbed energy into heat. The different energy relaxation channels for a vibrationally excited molecule in the liquid phase are schematically visualized in Fig.(5.1).

In the following, a formalism to quantify the absorbed and coherently emitted energy of molecules solved in water is derived, using the example of the test molecule DMSO<sub>2</sub>. Under certain assumptions, field-resolved measurements allow to temporally separate both contributions. A full picture, including the origin of absorption features in frequency-resolved measurements, is given.

### 5.1.1 Ab-initio simulation of the refractive index

To understand all effects involved in the interaction between resonant molecules and an exciting electric field, we initiated a collaboration with the chair for theoretical femtochemistry at the chemistry faculty of the Ludwig Maximilians University Munich held by Prof. Dr. Regina de Vivie-Riedle. Based on an ab-initio quantum chemistry model, our collaborators Martin Peschel and Dr. Daniel Keefer can calculate the temporal evolution of the microscopic dipole moment of a certain molecular system upon excitation by a given laser pulse. Here, we consider DMSO<sub>2</sub> molecules surrounded by water molecules vibrationally excited by the electric field of the experimental laser pulse as characterized in Section 3.5. For the given experimental intensity, only the first excited level of the vibrational eigenstates of the molecule is noticeably populated and the interaction between molecules and electric field is well described in a linear manner.

Density functional theory facilitates the calculation of the energy levels, i.e. the resonance frequencies, and of the transition dipole moments, i.e. the coupling strength of certain transitions to an external electric field, from the Schrödinger equation. The interaction with the surrounding water molecules is considered by averaging different microscopic environments. For each microscopic environment, the potential energy is described by an outer layer of structureless medium with macroscopic properties and an inner layer of a limited number of explicit water molecules arranged around the DMSO<sub>2</sub> molecule.<sup>2</sup> From the resulting transition dipole moments  $\mu_k$  and the resonance frequencies  $\omega_k$  one can

---

<sup>2</sup>The author thanks Martin Peschel for the explanation of the basic concepts of the quantum chemistry calculation.

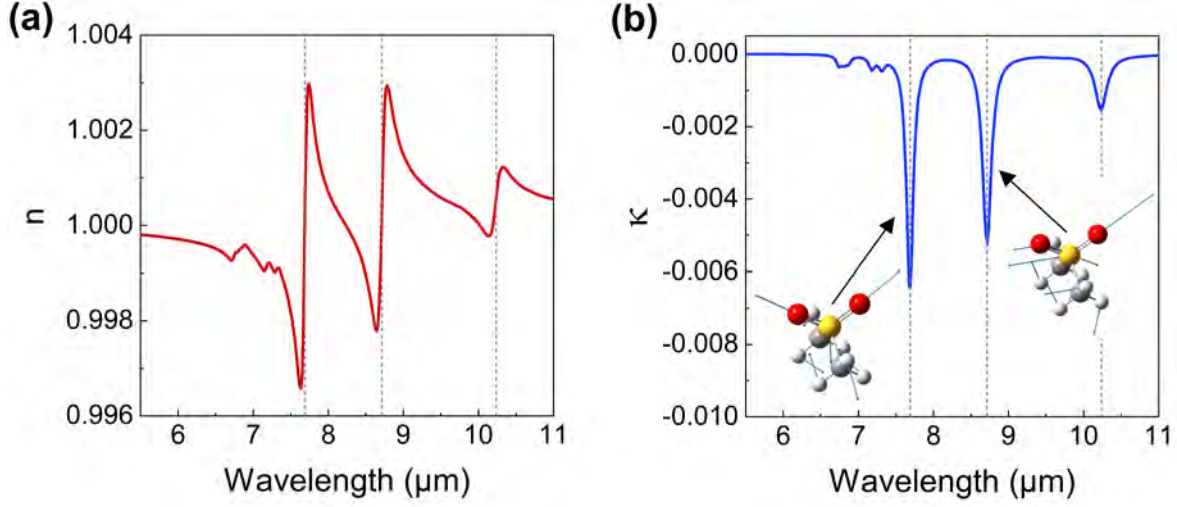


**Figure 5.2:** Real (a) and imaginary (b) part of the refractive index of 10 mg/ml DMSO<sub>2</sub> solved in water calculated from the ab-initio quantum chemistry model of the molecular system. The sketches of the molecule illustrate the vibrational resonances at 8.7 μm and 7.7 μm, which correspond to the symmetric and asymmetric stretch mode of the S-O bonds in DMSO<sub>2</sub>.<sup>1</sup>

calculate the linear susceptibility  $\chi^{(1)}$  of DMSO<sub>2</sub> solved in water [116]:

$$\chi^{(1)}(\omega) = \frac{2}{3} \frac{\beta N_A}{\epsilon_0 M_{\text{DMSO}_2} \hbar} \sum_{k=1}^N \frac{|\mu_k|^2 \omega_k}{\omega_k^2 - (\omega + i\Gamma)^2}, \quad (5.1)$$

with the concentration  $\beta$ , the Avogadro constant  $N_A$ , the vacuum permittivity  $\epsilon_0$ , the molecular mass of DMSO<sub>2</sub>  $M_{\text{DMSO}_2}$ , the number of vibrational resonances within the spectral coverage of the excitation pulse  $N$ , and the relaxation constant  $\Gamma$ . In the described model, the relaxation constant  $\Gamma$  was derived from a classical molecular dynamics simulation. The linear susceptibility is connected to the complex refractive index by

$$\underline{n}(\omega) = \sqrt{1 + \chi^{(1)}(\omega)} \quad (5.2)$$

and describes the macroscopic optical properties of the solution. In Fig.(5.2) the real and the imaginary part of the complex refractive index of 10 mg/ml DMSO<sub>2</sub> solved in water calculated from the ab-initio model using Eqn.(5.1) and Eqn.(5.2) is shown<sup>3</sup>. The real part  $n$  of the complex refractive index corresponds to the phase velocity and the imaginary part to the extinction coefficient  $\kappa$  which yields the absorption coefficient  $\alpha = -2\kappa\omega/c$ . In the ab-initio model, all resonances except for the major resonances at 8.7 μm and 7.7 μm are calculated from an empirical model to keep the computational costs at a reasonable level. The resonances at 8.7 μm and 7.7 μm correspond to the symmetric and asymmetric stretch

<sup>3</sup>The parameters from the ab-initio quantum chemistry model were provided by our collaborator Martin Peschel at the chair of Prof. Dr. Regina de Vivie-Riedle, Ludwig Maximilians University Munich.

mode of the S-O bonds in DMSO<sub>2</sub>. For illustration, both vibrational modes are depicted in Fig.(5.2b) with the arrows denoting the displacement vector of the according atoms.

From the complex refractive index  $\underline{n}$  the electric field of a laser pulse after propagation through a layer of DMSO<sub>2</sub> solution of thickness  $d$  can be calculated:

$$\tilde{A}_{sample}(\omega) = \tilde{A}_{ref.}(\omega) e^{-i(\underline{n}(\omega)-1)\frac{\omega d}{c}}, \quad (5.3)$$

where  $\tilde{A}_{ref.}$  is the Fourier transform of the complex electric field of the laser pulse after the transmission through a pure water reference and  $\tilde{A}_{sample}$  is the Fourier transform of the complex electric field of the laser pulse after the transmission through the DMSO<sub>2</sub> solution.

In the further course of this chapter, the ab-initio model will be compared to the experimentally recorded electric field after transmission of a laser pulse through DMSO<sub>2</sub> solution.

### 5.1.2 Energy balance formalism

Fig.(5.3a) shows the energy spectral density of a 30-fs Gaussian pulse before and after transmission through a 30  $\mu\text{m}$  thick layer of 10 mg/ml DMSO<sub>2</sub> solved in water. The energy spectral density after transmission through the DMSO<sub>2</sub> solution  $\bar{S}_{sample}$  was calculated using Eqn.(5.3) and the complex refractive index from the quantum chemistry model. For simplicity, only the resonance at 8.7  $\mu\text{m}$  was included. The energy spectral densities in Fig.(5.3a) correspond to the sample and reference spectra measured in conventional, frequency-resolved transmission spectroscopy. The purple shaded area, i.e. the difference of the energy spectral densities of sample and reference, is commonly interpreted as the energy absorbed by the sample molecules  $E_{final}$ :

$$E_{final} = \int_{-\infty}^{\infty} (\bar{S}_{ref.}(\nu) - \bar{S}_{samp.}(\nu)) d\nu, \quad (5.4)$$

with the energy spectral density  $\bar{S}_n(\nu)$ . According to the Beer-Lambert law  $\bar{S}_{samp.}(\nu) = \bar{S}_{ref.}(\nu) e^{-\alpha(\nu)d}$  with the absorption coefficient  $\alpha(\nu)$  and the sample thickness  $d$  we can write:

$$\begin{aligned} E_{final} &= \int_{-\infty}^{\infty} \bar{S}_{ref.}(\nu) (1 - e^{-\alpha(\nu)d}) d\nu \\ &\approx \int_{-\infty}^{\infty} \bar{S}_{ref.}(\nu) (\alpha(\nu)d - \alpha^2(\nu)d^2/2) d\nu, \end{aligned} \quad (5.5)$$

using the Taylor expansion of the exponential function up to the second order, which is a good approximation for small concentrations.

In a time-domain measurement, a more complete picture of the interaction between resonant molecules and an exciting electric field is revealed. Fig.(5.3b) shows the Fourier transformation of Eqn.(5.3), i.e. the electric field of the reference pulse and the reference pulse after interaction with the DMSO<sub>2</sub> molecules. The inset depicts the macroscopic electric field which is emitted by the coherently oscillating molecular dipoles after excitation

with the 30-fs pulse. The rapid decay indicates the dephasing of the oscillating dipoles due to interaction with the surrounding water molecules.

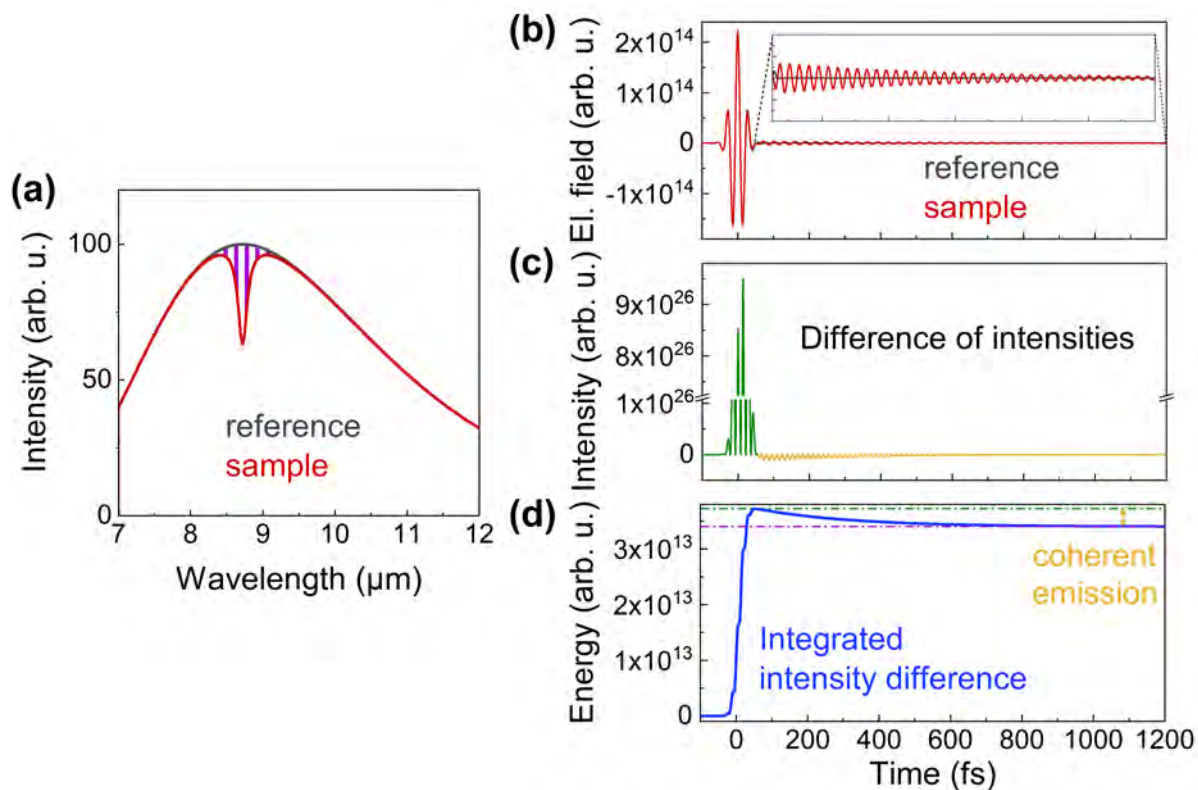


**Figure 5.3:** **a)** Conventional frequency-resolved transmission spectroscopy of 10 mg/ml DMSO<sub>2</sub> solved in water with a 30-fs Gaussian pulse spectrally centered at the maximum of the absorption line. For simplicity, only the strongest absorption line at 8.7 μm is considered. **b)** Time domain representation of the identical situation. The inset shows the fast decay of the macroscopic electric field emitted by the coherently oscillating molecular dipoles. **c)** Difference of the intensities of the electric field of the reference and the sample. Green coloured values denote the temporal region of predominant molecular absorption and yellow coloured values of predominant coherent re-emission. **d)** Integration of the instantaneous intensity difference along the time axis. The end value (dashed purple line) of the resulting energy balance (blue) coincides with the purple area in the frequency domain representation. The maximum (dashed green line) is interpreted as the amount of totally absorbed energy and the difference between maximum and end value as the amount of coherently re-emitted energy.

Fig.(5.3c) shows the difference of the squared electric fields (that is, the instantaneous intensity) of the reference and the sample waveforms. Positive values of the instantaneous intensity difference are coloured in green and negative values in yellow. This colour code indicates time intervals of predominant absorption (green) and predominant re-emission (yellow) of the DMSO<sub>2</sub> molecules.

The blue line in Fig.(5.3d) shows the integration of the instantaneous intensity difference along the time axis, i.e. the ensemble-integrated, instantaneous energy difference of the entire molecular system with respect to the unexcited state. This quantity is denoted energy balance of the molecular system  $E_{molecules}(\tilde{t})$ :

$$E_{molecules}(\tilde{t}) = \int_{-\infty}^{\tilde{t}} (I_{ref.}(t) - I_{samp.}(t)) dt, \quad (5.6)$$

where  $I_n(t) = C|A_n(t)|^2$  is the instantaneous intensity with the electric field amplitude  $A_n(t)$  and the proportionality constant  $C$ , and  $\tilde{t}_0$  is a time before the interaction. According to the Plancherel theorem, the end level of this energy balance  $E_{final}$  is identical to the purple shaded area in the frequency domain representation shown in Fig.(5.3a):

$$\begin{aligned} E_{final} &= \int_{-\infty}^{\infty} (I_{ref.}(t) - I_{samp.}(t)) dt \\ &= \int_{-\infty}^{\infty} (\bar{S}_{ref.}(\nu) - \bar{S}_{samp.}(\nu)) d\nu. \end{aligned} \quad (5.7)$$

Correspondingly, the end level  $E_{final}$  is denoted with a dashed purple line. However, in addition to this end level, the time-resolved energy balance reveals the entire dynamics of the resonant absorption by the DMSO<sub>2</sub> molecules and the dissipation into the molecular ensemble in a non-radiative or incoherent manner. The maximum of the energy balance indicates that initially more energy is absorbed by the molecules than recorded in a frequency-resolved measurement. The difference between the maximum and the end value of the energy balance (denoted with the yellow arrow in Fig.(5.3d)) corresponds to the energy which is coherently re-emitted by the resonantly excited molecules and detected by FRS. In this case, the portion of coherently re-emitted energy amounts to 8 % of the energy which is totally absorbed by the molecules from the exciting light field. A time-integrating detection scheme cannot distinguish between coherently emitted radiation of the molecules and radiation directly emitted by the spectroscopic light source. Therefore, the ratio of re-emitted energy is not accessible with such a detection scheme.

### 5.1.3 Ratio of absorbed and re-emitted energy

A clear separation of resonant absorption and coherent re-emission in the time domain is only possible if both mechanisms do not overlap, i.e. if the excitation pulse is infinitesimally short. In the limit of a  $\delta$ -pulse, an explicit expression for the coherently re-emitted energy  $E_{em.}$  can be derived. To this end, we start with the electric field  $A_{sample}(t)$  after transmission through the sample:

$$A_{sample}(t) = A_{ref}(t) * h(t) = A_{ref}(t) * (h(t) - \delta(t)) + A_{ref}(t), \quad (5.8)$$

with  $h(t)$  being the Fourier transform of the complex sample response function  $H(\nu)$ . In the limit of a  $\delta$ -pulse excitation, the first term of Eqn.(5.8) describes the coherently

re-emitted radiation  $A_{em.}(t)$  because the second term  $A_{ref}(t)$  is non-zero only during the infinitesimally short duration of the excitation:

$$A_{em.}(t) := A_{ref}(t) * (h(t) - \delta(t)). \quad (5.9)$$

Now we can calculate the re-emitted energy  $E_{em.}$ :

$$\begin{aligned} E_{em.} &:= \int_{-\infty}^{\infty} I_{em.}(t) dt = \int_{-\infty}^{\infty} C |A_{ref}(t) * (h(t) - \delta(t))|^2 dt \\ &= \int_{-\infty}^{\infty} \bar{S}_{ref.}(\nu) |H(\nu) - 1|^2 d\nu. \end{aligned} \quad (5.10)$$

For a  $\delta$ -pulse excitation, the energy spectral density must be constant so that:

$$\int_{-\infty}^{\infty} \bar{S}_{ref.}(\nu) |H(\nu) - 1|^2 d\nu = \bar{S}_{ref.} \int_{-\infty}^{\infty} |H(\nu) - 1|^2 d\nu. \quad (5.11)$$

Due to causality we know that the Fourier transform  $h(t) - \delta(t)$  of the function  $H(\nu) - 1$  is zero for  $t < 0$ . Therefore the real part of  $H(\nu) - 1$  is equal to half of the re-emitted energy:

$$\begin{aligned} \bar{S}_{ref.} \int_{-\infty}^{\infty} |\Re[H(\nu)] - 1|^2 d\nu &= E_{em.}/2 \\ \Rightarrow E_{em.} &= 2\bar{S}_{ref.} \int_{-\infty}^{\infty} |\Re[H(\nu)] - 1|^2 d\nu. \end{aligned} \quad (5.12)$$

With the complex absorption coefficient  $\underline{\alpha}(\nu) = 2i(\underline{n}(\nu) - 1)k$  and the Taylor expansion of the exponential function for small concentrations,  $E_{em.}$  becomes:

$$\begin{aligned} E_{em.} &= 2\bar{S}_{ref.} \int_{-\infty}^{\infty} |\Re[e^{-\underline{\alpha}(\nu)d/2}] - 1|^2 d\nu \\ &\approx 2\bar{S}_{ref.} \int_{-\infty}^{\infty} \Re^2[-\underline{\alpha}(\nu)d/2 + \underline{\alpha}^2(\nu)d^2/8] d\nu, \end{aligned} \quad (5.13)$$

and with the equality  $\alpha(\nu) = -2\Im[\underline{n}(\nu)]k$  we arrive at:

$$E_{em.} \approx \bar{S}_{ref.} \int_{-\infty}^{\infty} \alpha(\nu)^2 d^2/2 d\nu. \quad (5.14)$$

The maximum of the energy balance, i.e. the totally absorbed energy  $E_{max}$  is defined as:

$$\begin{aligned} E_{max} &= E_{final} + E_{em.} \\ &\approx \bar{S}_{ref.} \int_{-\infty}^{\infty} (\alpha(\nu)d - \alpha(\nu)^2 d^2/2) d\nu + \bar{S}_{ref.} \int_{-\infty}^{\infty} \alpha(\nu)^2 d^2/2 d\nu \\ &= \bar{S}_{ref.} \int_{-\infty}^{\infty} \alpha(\nu) d d\nu. \end{aligned} \quad (5.15)$$

Fig.(5.4a) and (b) show the calculated values for the  $\delta$ -pulse limit (solid lines) and the 30-fs Gaussian excitation pulse (dashed lines) comparing their frequency-resolved energy

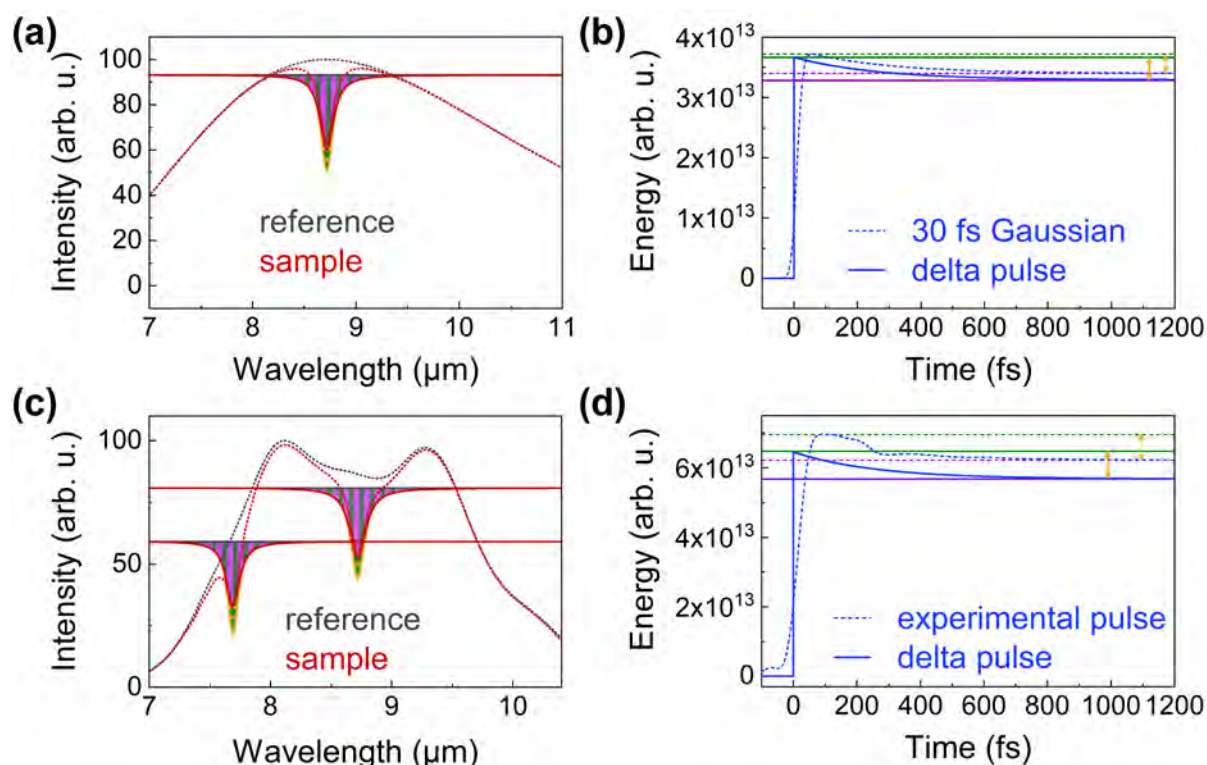


**Figure 5.4:** **a)** Comparison of the reference and sample spectrum of a 30-fs Gaussian excitation pulse (dashed lines) and a  $\delta$ -pulse (solid lines). In the  $\delta$ -pulse limit, the energy spectral density of the coherently re-emitted energy (yellow striped area) can be calculated exactly. The purple paid area corresponds to the end value of the energy balance and the green paid area to the maximum, i.e. the totally absorbed energy. **b)** Time-resolved energy balance for the 30-fs pulse and the  $\delta$ -pulse. **c)** Analogue to (a), including two absorption features of DMSO<sub>2</sub> and an experimental excitation pulse with a duration of 62.5 fs. **d)** Time-resolved energy balance for the experimental pulse and the  $\delta$ -pulse. The energy balance was calculated for each absorption line independently and then added.

spectral density and their time-resolved energy balance, respectively. In the frequency domain representation, the energy corresponding to the maximum of the energy balance, i.e. the totally absorbed energy is depicted as green area, the energy corresponding to the end value, i.e. the part of the absorbed energy which dissipates in a non-radiative or incoherent manner is depicted as striped purple area, and the energy corresponding to the difference of maximum and end value, i.e. the coherently re-emitted energy is depicted as striped yellow area. Only in the  $\delta$ -pulse limit the totally absorbed and re-emitted energy is well defined. However, the good agreement of the maximum and the end value for  $\delta$ -pulse and 30-fs pulse excitation in Fig.(5.4b) justifies the definition of a quasi-impulsive regime. In the quasi-impulsive regime, the deviation between the maximum and the end value of the energy balance as compared to the  $\delta$ -pulse limit is small and the determination of the ratio between coherently re-emitted and absorbed energy is possible. From Eqn.(5.14) and

Eqn.(5.15) it follows that the ratio between coherently re-emitted and absorbed energy scales linearly with the absorption coefficient  $\alpha$ , i.e. with the concentration.

To decide whether an experimental excitation pulse lies in the quasi-impulsive regime, all resonance features within its spectral coverage have to be considered for the energy balance. The energy balance then consists of the sum of several  $\delta$ -pulse energy balances. In Fig.(5.4c) and (d) this concept is illustrated for the two major absorption features of DMSO<sub>2</sub> and the experimental excitation pulse from Section 3.5. For each absorption line the constant energy spectral density of the  $\delta$ -pulse is defined as the weighted average of the reference spectrum of the experimental pulse in the vicinity of the absorption peak.

The colour code in Fig.(5.4c) and (d) is equivalent to the colour code in Fig.(5.4a) and (b). The absolute values of the maximum and the end value of the energy balance for the  $\delta$ -pulse and the experimental pulse deviate slightly because the energy spectral density in the experiment is not constant across the absorption feature. However, the ratio between coherently re-emitted and absorbed energy of 12 % and 11 % for the  $\delta$ -pulse and the experimental pulse, respectively, is in good agreement.

## 5.2 Experimental energy balance of vibrationally excited DMSO<sub>2</sub> molecules

The spectroscopic instrument whose development is described in Chapter 3 is the adequate tool to experimentally validate the ab-initio model of vibrationally excited DMSO<sub>2</sub> molecules surrounded by water. Due to the high dynamic range and the precise delay axis of the electric-field-resolved detection we can evaluate the experimental energy balance and compare it to the theoretical findings on a sub-electric-field-cycle time scale.

### 5.2.1 Quasi-impulsive excitation

In analogy to the benchmarking experiment presented in Section 3.5, we performed alternating EOS measurements of the MIR waveform after transmission through a 30  $\mu\text{m}$  thick layer of pure water and a 30  $\mu\text{m}$  thick layer of 10 mg/ml DMSO<sub>2</sub> solved in pure water. The experimental parameters were identical to the configuration applied in the second benchmarking measurement series except for the number of single scans per measurement. Here, we averaged over 10 forward and 10 backward scans before exchanging the sample in the liquid cuvette.

Fig.(5.5a) shows an exemplary EOS trace of the water reference and the DMSO<sub>2</sub> sample. In the time window starting 400 fs after the maximum of the exciting MIR waveform the y-axis is scaled by a factor of 20 to visualize the dominating resonant response of the DMSO<sub>2</sub> molecules. Before applying the energy balance formalism, the measured data was filtered in the Fourier domain using a super-Gaussian filter with a FWHM of 2.8  $\mu\text{m}$  centered at 8.8  $\mu\text{m}$ . Filtering removes noise components outside the spectral coverage of the exciting MIR waveform. In the next step, the instantaneous intensity of the measured electric field of the sample is subtracted from the instantaneous intensity of the measured

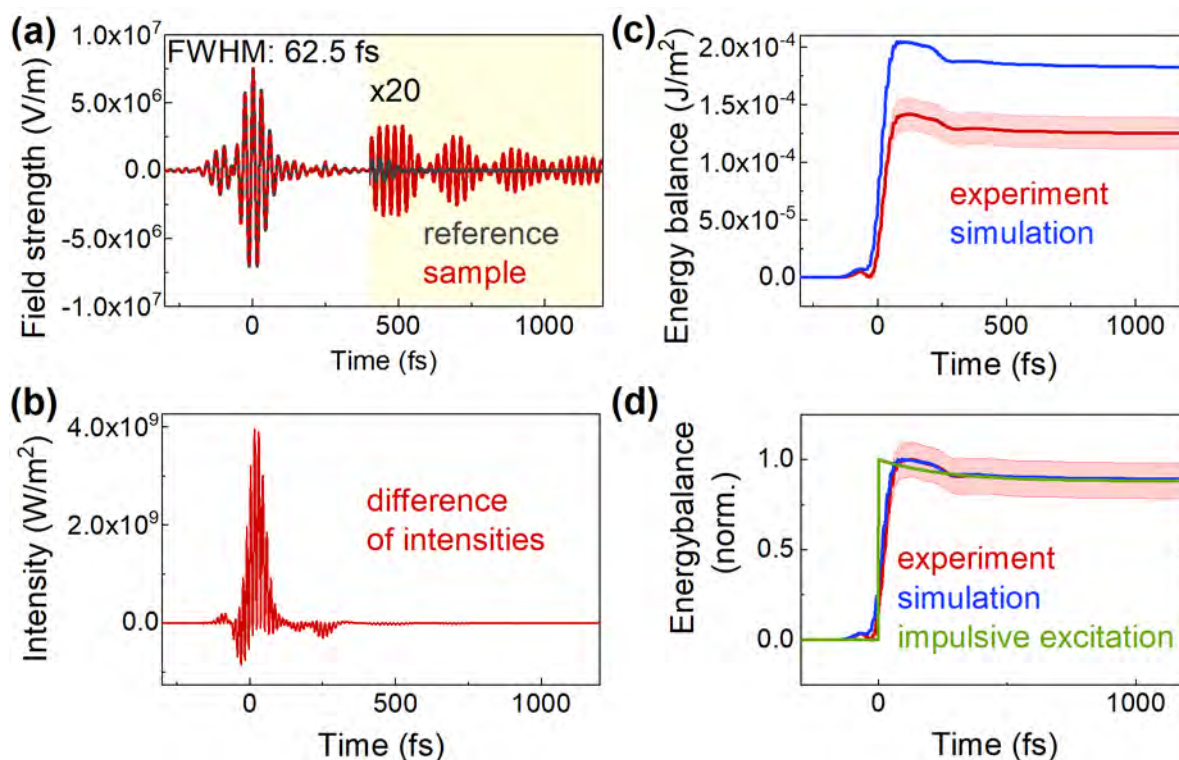


**Figure 5.5:** Energy balance of DMSO<sub>2</sub> upon quasi-impulsive excitation. **a)** EOS trace of the MIR waveform after transmission through pure water (reference) and 10 mg/ml DMSO<sub>2</sub> solved in pure water (sample). Within the yellow shaded area the amplitude is scaled by a factor of 20. The EOS signals are calibrated to the experimental field strength using the measured peak intensity after transmission through water. **b)** Difference of the instantaneous intensity of reference and sample. **c)** Integration of the instantaneous intensity difference over time yields the energy balance of experiment and calculations. The red curve denotes the mean value of five consecutive measurements and the red shaded area the standard deviation thereof. The blue curve was calculated based on an ab-initio model of DMSO<sub>2</sub> molecules in a water environment. **d)** Normalized energy balance of experiment and simulation. For comparison, the green line shows the calculated energy balance of the molecular system upon impulsive excitation with a delta pulse.

electric field of the reference. By using the real electric fields, the rapidly varying part of the carrier field is included in the instantaneous intensity difference. Exact temporal overlapping of the maxima of reference and sample measurement avoids timing jitter errors in the instantaneous intensity difference. The resulting instantaneous intensity difference is shown in Fig.(5.5b). According to the introduced definition of the instantaneous intensity difference, positive values in Fig.(5.5b) correspond to a time period where the DMSO<sub>2</sub> molecules predominantly absorb energy from the electric field, whereas negative values indicate a time period of prevailing coherent emission by oscillating molecular dipoles. The negative contributions previous to the maximum of the excitation pulse can be explained

by the prepulse-feature (see Section 5.2.2).

To evaluate the temporal evolution of the energy change of the DMSO<sub>2</sub> molecules upon resonant excitation with a few-cycle MIR waveform, the instantaneous intensity difference is integrated along the time axis. Fig.(5.5c) depicts the resulting energy balance. The red line denotes the mean value of five consecutive measurements and the red shaded area the error bar corresponding to their standard deviation. In analogy to the experimental energy balance, we calculated the energy balance based on the ab-initio model of DMSO<sub>2</sub> molecules in a water environment. To this end, the measured reference pulse was propagated through a 30 μm thick medium with a complex refractive index as defined in Eqn.(5.3). This indirect calculation is necessary because the more direct time dependent energy expectation value of the molecular system in the ab-initio model does not include propagation effects.

To allow a quantitative comparison of simulation and experiment the measured EOS trace was calibrated. Therefore, the peak intensity of the MIR pulse after propagation through the liquid cuvette filled with pure water was estimated. With an average power of 5 mW, a spot size of 300 μm (diameter at FWHM of the intensity envelope), and a pulse duration of 62.5 fs the peak intensity  $I_{peak}$  amounts to  $7.5 \times 10^{10} W/m^2$  which according to the relation  $I_{peak} = cn\epsilon_0/2|E_{peak}|^2$  corresponds to a maximum field strength of  $7.4 \times 10^6$  V/m. For these parameters no noticeable population of higher vibrational levels occurs and a purely linear description of the interaction between exciting electric field and DMSO<sub>2</sub> molecules is justified.

Fig.(5.5c) shows a good qualitative agreement between the energy balance from the ab-initio model and the experiment. However, the maximum and the end value deviate by a factor of 1.4. This deviation exceeds the experimental error and its origin will be discussed below. As a measure for the ratio between absorbed and coherently re-emitted energy, the normalized energy balance is plotted in Fig.(5.5d). In this representation, the agreement between experiment and ab-initio model is excellent. Thus, the simulation results need to be scaled by a factor of 1/1.4 to match the experimental results. Following the argumentation above, the end value of the normalized energy balance corresponds to the ratio of incoherently emitted energy and, consequently, 1 - the end value denotes the ratio of coherently emitted energy. For the observed molecular system, the ratio of coherently emitted energy amounts to 12 % of the totally absorbed energy. For comparison, the normalized energy balance for a truly impulsive excitation with a delta pulse as described in Section 5.1.3 is shown. The end values of the experimental energy balance and the calculated energy balance for a delta pulse agree well and prove that the measured ratio of coherently emitted energy of 12 % is reasonable. The experimental pulse duration of 62.5 fs lies still in the regime of quasi-impulsive excitation where a temporal separation of absorbed and re-emitted energy is possible.

To understand the origin of the quantitative deviation between the experimental and the calculated energy balance, we compare the respective absorption curves of 10 mg/ml DMSO<sub>2</sub> solved in water shown in Fig.(5.6). The absorption  $\alpha$  is defined by the Beer-Lambert law  $I(\omega) = I_0(\omega)e^{-\alpha z}$  with  $I(\omega)$  being the FT of the sample EOS trace,  $I_0(\omega)$  the FT of the reference EOS trace, and  $z$  the nominal sample thickness of 30 μm. The

## 5.2 Experimental energy balance of vibrationally excited DMSO<sub>2</sub> molecules 97

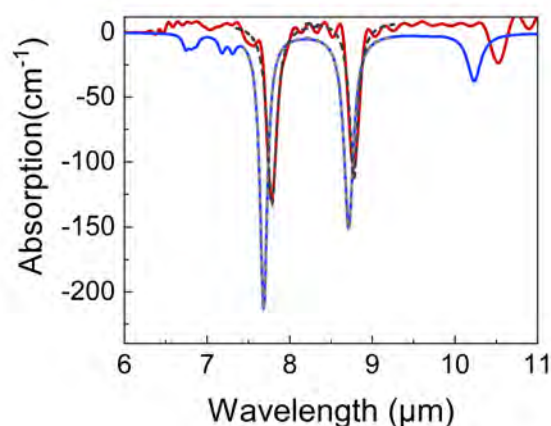


**Figure 5.6:** Absorption of 10 mg/ml DMSO<sub>2</sub> calculated for the measured data and the ab-initio model. The dashed grey lines denote a Lorentzian fit to the two major resonances within the spectral coverage of the employed light source. The red line shows the mean value of five consecutive measurements. The mean standard deviation within the shown spectral window is 1.8 % and can therefore not be distinguished from the experimental absorption curve in this plot.

red line denotes the mean value of five consecutive measurements with a mean standard deviation of 1.8 % within the considered spectral range. The dashed grey lines indicate a Lorentzian fit to the two major resonance features, respectively. Tab.(5.1) summarizes the resultant line parameters obtained from the Lorentzian fit of the measured and the calculated absorption.

**Table 5.1:** Measured and calculated parameters for the two major resonances of DMSO<sub>2</sub> within the spectral coverage of the employed light source retrieved from a Lorentzian fit of the respective absorption.

	$\lambda_1$	$\delta\lambda_1$	$\alpha_1$	$\lambda_2$	$\delta\lambda_2$	$\alpha_2$
measured	8.78	0.13	-129	7.78	0.14	-147
calculated	8.71	0.14	-150	7.68	0.11	-209

The largest deviation between experiment and ab-initio model is observed for the peak absorption  $\alpha_1$  and  $\alpha_2$ . These values are based on the transition dipole moments obtained from density functional theory. The precision of the calculated transition dipole moments is defined by the size of the employed basis set and thus depends on the available computing power. However, the employed quantum chemistry model does not allow to quantitatively estimate the errors caused by the limited basis set. The same explanation applies to the position of the resonance frequencies. Due to the smaller deviation between experiment and ab-initio model for  $\lambda_1$  and  $\lambda_2$  we conclude that the limited size of the basis set is less critical for the position of the resonance frequency. The line width  $\delta\lambda_1$  and  $\delta\lambda_2$  was modelled based on classical molecular dynamics and is therefore unaffected by the limited

size of the basis set. For a quantitative comparison of the line widths in calculation and experiment, the limited spectral resolution in the experiment has to be considered. The internal reflection from the EOS detection crystal after 1.4 ps confines the maximum delay window available for the Fourier transformation to about 2 ps and hinders an exact measurement of the line width in the frequency domain. Instead, the exponential decay of the signals in experiment and calculation could be compared in the time domain up to 1.4 ps. However, the agreement of the line widths is not of primary interest here.

The mismatch in the peak absorption explains the qualitative difference between the energy balance of experiment and calculation in Fig.(5.5c) whereas the excellent agreement of the normalized energy balance in Fig.(5.5d) demonstrates that the ab-initio model can still reproduce the temporal evolution of the energy change of the DMSO<sub>2</sub> molecules upon excitation with a quasi-impulsive excitation.

## 5.2.2 Chirped excitation

The realization of a shorter excitation pulse is currently not feasible with the presented approach for MIR generation. Instead, the interaction of temporally stretched pulses with DMSO<sub>2</sub> molecules solved in water are investigated in the following.

To this end, we inserted a 5 mm thick CaF window in the MIR beam path in front of the liquid cuvette. The high group delay dispersion of CaF leads to a temporal broadening of the MIR waveform as shown in Fig.(5.7a). The pulse duration increased from 62.5 fs to almost 1 ps. The negative curvature of the spectral phase in Fig.(5.7c) indicates a decreasing instantaneous frequency across the duration of the pulse. Fig.(5.7c) shows the difference of the instantaneous intensities of the reference and the sample.

Except for the additional material in the MIR beam path, all experimental parameters were identical to the previous measurement and we again recorded alternating EOS traces of the pulse after transmission through pure water and 10 mg/ml DMSO<sub>2</sub> solved in pure water. The two exemplary EOS traces in Fig.(5.7a) indicate that compared to the reference pulse, the pulse after transmission through the DMSO<sub>2</sub> solution shows amplitude modulations.

In analogy to the quasi-impulsive excitation, we calculated the energy balance of the molecular system upon resonant excitation with a dispersive MIR pulse. The red line in Fig.(5.8a) denotes the mean value of five consecutive measurements and the red shaded area the standard deviation thereof. The blue curve corresponds to the calculated energy balance based on the ab-initio model. According to the results of the energy balance study with the compressed pulse, the simulated curve was scaled by a factor of 1/1.4.

Compared to the quasi-impulsive case, the energy balance for the dispersive excitation differs with regard to two aspects. In the dispersive case, the energy balance has two local maxima and oscillates around the asymptotic end value with decreasing amplitude. The two local maxima can be explained by the two major resonances of DMSO<sub>2</sub> within the spectral coverage of the excitation. Due to the decreasing instantaneous frequency across the duration of the dispersive pulse, the resonance at 8.78  $\mu\text{m}$  is excited before the

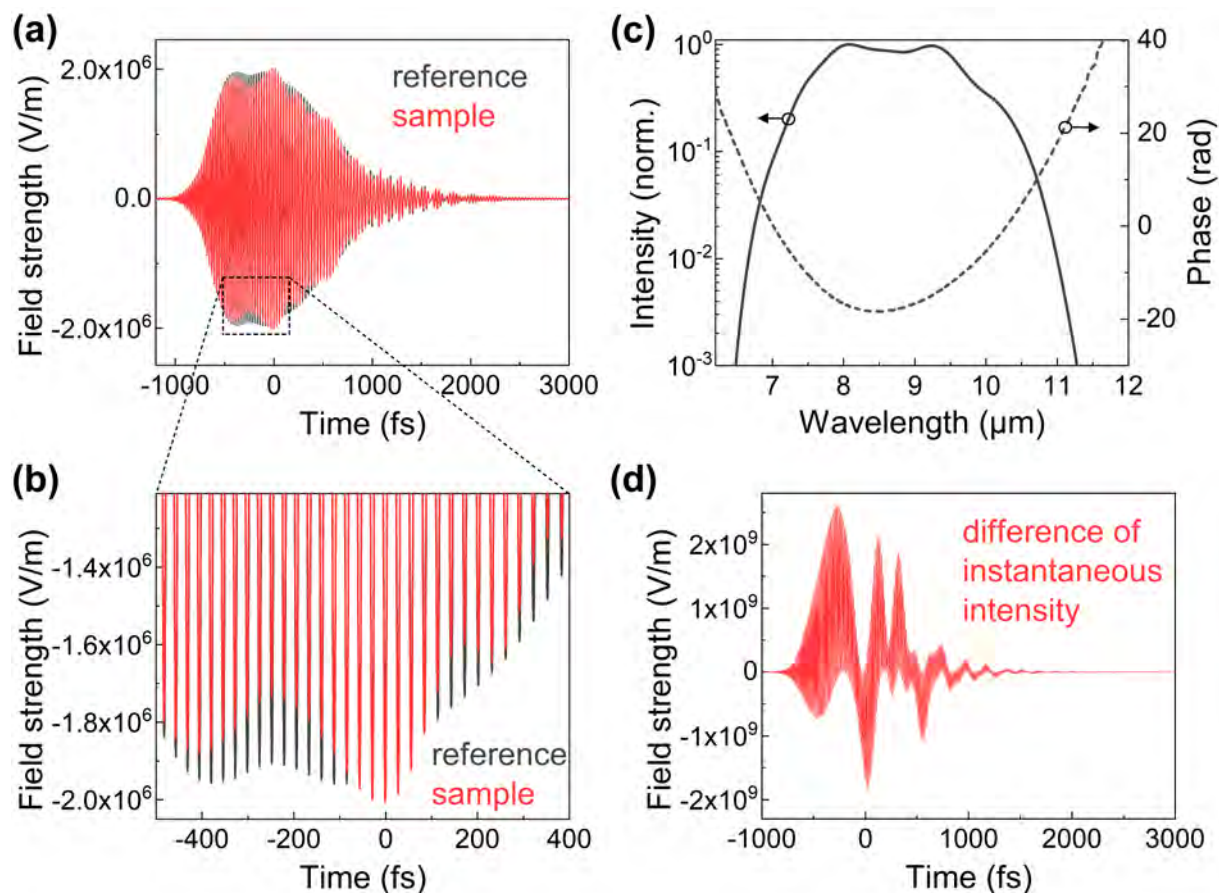


**Figure 5.7:** a) EOS trace of the dispersed MIR waveform after transmission through pure water and 10 mg/ml DMSO<sub>2</sub> solved in pure water, respectively. The pulse was temporally stretched by a 5 mm thick CaF window. b) Close-up of (a). c) Spectrum and spectral phase of the dispersed reference pulse. d) Difference of the instantaneous intensities of reference and sample.

resonance at 7.68  $\mu\text{m}$ . Thus, the molecules first absorb energy in one vibrational mode up to -60 fs and then start re-emitting at the corresponding resonance frequency. After 300 fs, the instantaneous frequency is in resonance with the next vibrational mode such that the molecules again absorb energy.

Between -60 fs and 300 fs and after 500 fs, the oscillating energy balance represents an alternating sequence of stimulated emission and absorption of the molecules. This behaviour is understood as interference of the coherently emitted radiation from the molecules at constant frequency with the changing instantaneous frequency of the exciting radiation. The period of the oscillations represents the beat frequency between the resonance frequency and the instantaneous frequency of the MIR waveform. This effect was observed for electronic resonances in sodium atoms [119] and rubidium atoms [120, 121] and referred to as *coherent transients*. If a single, well characterized resonance is excited the coherent

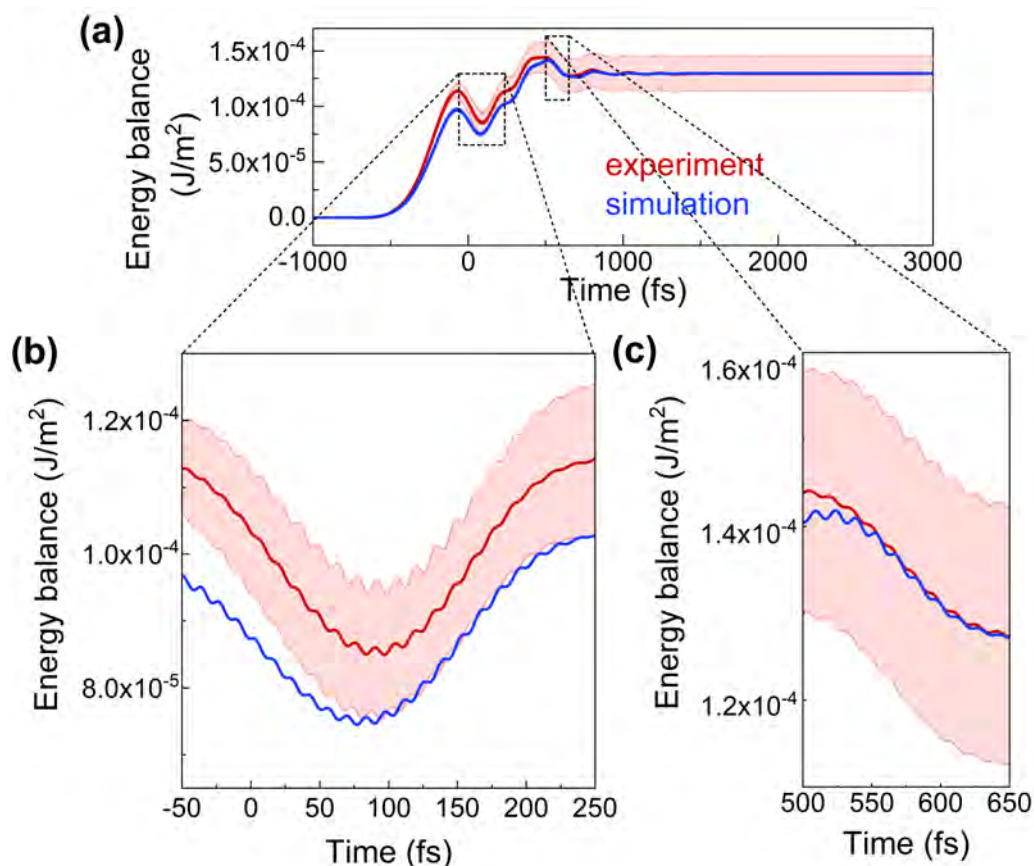


**Figure 5.8:** **a)** Time resolved energy balance of 10mg/ml DMSO<sub>2</sub> solved in water upon resonant excitation with a dispersive MIR pulse. The red line denotes the mean value of four consecutive measurements and the red shaded error the standard deviation thereof. The blue curve was calculated based on an ab-initio model. According to the results of the energy balance study with the compressed pulse, the simulated curve was scaled by dividing by a factor of 1.4. **b)** and **c)** Close-up of the experimental and calculated energy balance of the selection indicated by the dashed rectangles.

transients can be used to measure the phase of the excitation pulse in a cross-correlation experiment [122]. In the mentioned experiments, the coherent transients were observed as oscillations of the fluorescence signal in pump-probe spectroscopy. Thus, any dynamics on the sub-electric-field-cycle time scale were not accessible.

Here, we observe the same phenomenon for vibrational resonances of DMSO<sub>2</sub> molecules in the liquid phase. However, we measure the electric field of the excitation pulse and the coherently oscillating molecular dipoles as the most direct observable of the interaction. This direct observable also provides insight into the energy exchange dynamics on a sub-electric-field-cycle time scale. The close-ups of the energy balance in Fig.(5.8b) and Fig.(5.8c) exhibit oscillations at twice the instantaneous frequency of the exciting field.

## 5.2 Experimental energy balance of vibrationally excited DMSO<sub>2</sub> molecules 101

Thus, the absorbed and re-emitted energy of the molecules changes stepwise with every half-cycle of the electric field. At global turning points of the energy balance as for example at 100 fs, the amount of absorbed and re-emitted energy is equal. This situation is represented by oscillations around a quasi constant value on the sub-cycle time scale.

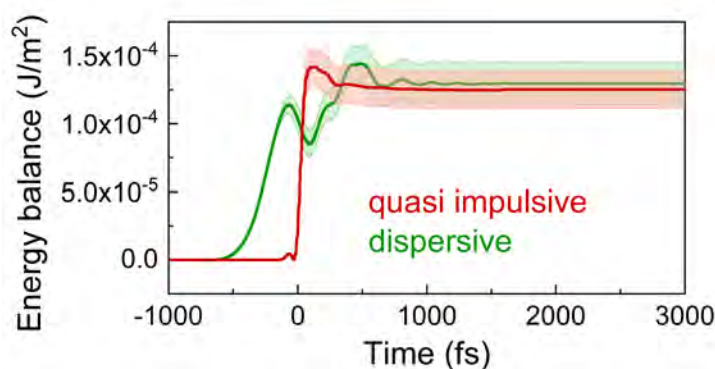


**Figure 5.9:** Energy balance of 10 mg/ml DMSO<sub>2</sub> molecules solved in water upon excitation with a quasi-impulsive and a dispersive pulse with the same energy. The solid lines denote the average of four consecutive measurements and the shaded area the standard deviation thereof.

All described effects are reproduced by the ab-initio model semi-quantitatively, i.e. by scaling the simulated energy balance with a factor of 1/1.4. The quantitative deviation was discussed above and the given explanations apply analogously to the dispersive case. In the dispersive case, a temporal separation between absorbed and coherently re-emitted energy is not possible. Thus, the estimation of the ratio between coherently emitted and absorbed energy is not feasible. In a time-integrated measurement one would expect the same outcome for a quasi-impulsive excitation and a dispersive excitation if the energy of the pulses is conserved. In Fig.(5.9) a comparison of the absolute energy balance for the two different excitation pulses is shown. The agreement of the end value (within the experimental error bar), i.e. the observable in a time-integrated measurement confirms this plausibility check.

In conclusion, we have employed electric-field-resolved spectroscopy to trace the complete energy transfer dynamics between octave-spanning, field-controlled MIR waveforms and vibrating DMSO<sub>2</sub> molecules in aqueous solution, with sub-cycle resolution: resonant absorption and stimulated emission are observed on a few-femtosecond scale, optical-phase-dependent coherent transients manifest on the femtosecond-to-picosecond scale and, owing to their varying environments in the solvent, the oscillations of coherently-excited molecules dephase within several picoseconds. Quantum-chemistry ab-initio modelling reproduces our experimental observations well. This agreement provides the basis for quantitative, molecular-scale insight into the individual mechanisms forming the macroscopic susceptibility of the sample such as direct interactions of the solute with the surrounding water molecules as well as the screening effect of the polarizable continuum. Furthermore, the

future extension of this study to nonlinear interactions of intense excitation fields with vibrating molecules is fathomable.

Besides shedding light onto the more complex energy transfer mechanisms in the case of nonlinear excitations, the experimental access to higher-order susceptibilities is likely to improve the specificity in molecular fingerprinting of complex (biological) samples.

# Chapter 6

## Summary and outlook

The aim of this dissertation was to further develop field-resolved spectroscopy, in experiment and theory, towards exploiting its full technological potential as a tool for studying the interaction of molecules with the electric fields of broadband, phase-coherent infrared pulses. A particularly attractive prospect afforded by a mature FRS instrument is to perform broadband vibrational spectroscopy as a novel method for fast, precise and high-throughput medical diagnosis.

The FRS instrument developed in this thesis is based on a 100-W-scale Yb:YAG thin-disk oscillator delivering 260-fs pulses centered at 1- $\mu\text{m}$  emission wavelength at a repetition rate of 28 MHz. The output pulses are spectrally broadened in a two-stage, all-solid-state multipass cell setup and subsequently compressed with dispersive mirrors. After the first and the second stage, the pulses have a duration of 64 fs and 15 fs, respectively. This corresponds to an overall spectral broadening factor of 18 with a throughput of 73 % resulting in a train of 2.4- $\mu\text{J}$  pulses at an average power of 66 W.

In an LGS crystal, the 1- $\mu\text{m}$  pulses are frequency down-converted to the MIR spectral region via IPDFG to yield a superoctave spectrum spanning from 5  $\mu\text{m}$  to 12  $\mu\text{m}$  at -20 dB with an averaged power of 52 mW. Active intensity noise stabilization of the NIR driving pulses enabled the reduction of the MIR RIN by a factor of 5 from 0.36 % to 0.07 % in the frequency band between 1 Hz and 100 kHz. With customized dispersive mirrors the MIR pulses were compressed to 62.5 fs. IDT-aided EOS of the MIR pulses allowed to detect their electric field with an intensity dynamic range of 11 orders of magnitude within a measurement time of 45 s and a nominal resolution of 4  $\text{cm}^{-1}$ . Operating the system at a pressure of  $10^{-3}$  mbar facilitated the detection of molecular fingerprints in a truly background free manner for the first time.

All these parameters critically affect the performance of the FRS instrument which was benchmarked in an experiment on the sensitivity to small concentrations of DMSO<sub>2</sub> molecules solved in water. In the optimized configuration, a limit of detection of 300 ng/ml was determined, which can compete with the state-of-the-art FRS instrument developed in our group and outperforms a research-grade FTIR spectrometer by more than one order of magnitude.

In the frame of developing the FRS instrument, two different concepts to replace the rather slow mechanical delay stage required for EOS detection were developed and implemented. A rapid scanning spectrometer promises to facilitate the real-time observation of live biological processes and chemical reactions. In addition, performing full EOS scans at multi-kHz rates allows to record single measurements unaffected by technical noise which is usually dominant in the low-kHz range.

When the ultrasonic vibration of a PZT is coupled to a sonotrode, the excitation of its mechanical resonance frequency leads to an amplification of the vibration. A mirror contacted to the oscillating surface of the sonotrode can be utilized as rapid mechanical delay line to record full EOS scans at 38 kHz. The sonotrode experiment conducted with the developed FRS instrument showed that with rapid referencing schemes, the spectroscopic sensitivity strictly increases with the square-root of the measurement time. To mitigate the limited delay range and the mechanical instabilities introduced by the moving parts of the sonotrode approach another concept relying on a second oscillator with detuned repetition rate was described. Periodically modulating the repetition rate offset between the two oscillators enables the application-specific adjustment of scan rate, maximum delay and delay step. The presented proof-of-principle measurements demonstrated the feasibility of ECOPS in combination with a high power Yb:YAG thin-disk oscillator for MIR detection. Together with EODT this indicates a viable solution for a flexible rapid scanning FRS instrument.

To experimentally access the difference in molecular composition of two samples attributed to their electric field difference after excitation with light, broadband, interferometric subtraction of optical fields was investigated. The design and construction of an achromatic interferometer based on the combination of Fresnel reflections off the first and second surface of a beam splitter or beam combiner, respectively enables the optical subtraction of super-octave optical fields. If a sample is placed in one arm and a reference in the other arm of the achromatic interferometer, experimental referencing yields their difference signal. For an NIR light source spanning from 950 nm to 2100 nm, an interferometric extinction of  $6 \times 10^{-4}$  was demonstrated. In the MIR spectral region, the lack of high-quality beam splitter substrates limited the extinction ratio to  $4 \times 10^{-3}$  in the wavelength range from 9  $\mu\text{m}$  to 12  $\mu\text{m}$ .

In a theoretical study, the SNR advantage for interferometric referencing in conventional transmission spectroscopy was evaluated. For intensity noise limited spectrometers the improvement of the limit of detection as compared to a direct measurement scales with  $1/\sqrt{4\Delta}$  where  $\Delta$  is the extinction ratio. However, the signal magnitude in the interferometric configuration also scales with the extinction ratio. Therefore, a sufficiently high source power has to be available to overcome detector noise.

The numerical simulations on the time-resolved SNR of FRS in the direct and the differential configuration revealed that the suppression of the excitation pulse and the global molecular background in the differential configuration can lead to a higher SNR and a time window for background free detection starting earlier after the excitation pulse. To

decide whether the additional experimental complication of interferometric referencing is beneficial, the MIR RIN and the achievable extinction ratio have to be evaluated. Other critical parameters are the intensity fluctuations of the interferometric extinction and the reduced excitation power on the sample. In the future, diamond beam splitters will be a potential candidate to improve the extinction ratio in the MIR. Together with a more advanced active interferometer length stabilization, a better engineered design, and operation in vacuum, optical subtraction could enhance the sensitivity of FRS.

The application of the developed FRS instrument to study the time-resolved energy transfer between molecules and the electric field upon vibrational excitation demonstrates the potential of directly detecting the electric field with high sensitivity and sub-optical-cycle temporal resolution for the investigation of fundamental light-matter interactions on their native time scales. When the molecules are excited with a compressed MIR pulse, the experimentally measured, time-resolved energy balance reveals the evolution of the absorbed energy and the amount of coherently re-emitted energy. The analytical expressions derived for a truly impulsive  $\delta$ -pulse excitation reproduce the experimental observations well. In a conventional, frequency-resolved measurement, only the total (i.e., time-integrated) amount of absorbed energy which dissipates into the environment of the excited molecules is accessible.

When the molecules are excited with a dispersive MIR pulse, the energy balance shows oscillations converging towards its asymptotic end value on the time scale of several hundred fs. These coherent transients are caused by the interference of the coherently emitted electric field of the molecules at constant frequency with the changing instantaneous frequency of the excitation electric field, and constitute a sequence of transient absorption and stimulated emission. In addition, the sub-optical-cycle temporal resolution allows to measure the stepwise energy changes of the molecules with every half-cycle of the exciting and the re-emitted electric field, for the first time. All experimental observations are in good agreement with an ab-initio quantum chemistry model of the molecular system.

This comprehensive study on the linear interaction between resonant molecules and exciting electric fields correlates experimental results with an ab-initio model and can readily be extended to studies of nonlinear light matter interactions.

The findings on the linear interaction between molecules and electric fields and the technological advances presented in this thesis pave the way towards a conceptually different FRS instrument. Rapid scanning based on ECOPS in combination with EODT promises to enable the acquisition of full EOS scans at multi kHz rates, i.e. faster than technical noise affects the signal. If reference and sample measurements are recorded in parallel via two physically different optical paths, spectral division of reference and sample traces will allow the extraction of the complex transfer function of a sample, nearly unaffected by technical noise. The resulting transfer function will ideally only be affected by the shot noise of the light source, i.e. by its spectral coverage and power. In this configuration, the sensitivity of FRS will increase strictly with the square root of the measurement time.

Due to rapid scanning and rapid referencing temporal filtering of the excitation pulse to

avoid intensity noise limitations is likely to become unnecessary and intensity fluctuations of the sample-specific molecular fingerprint can be suppressed by choosing an adequate reference substance. Possible saturation effects of EOS detection, photodiodes, or digitization electronics can then be mitigated by temporally stretching the excitation pulse or by implementing interferometric optical subtraction.

This technologically enhanced FRS instrument will benefit the further exploration of vibrational spectroscopy as diagnostic tool in medical applications.

# Appendix A

## Data archiving

All data utilized in this thesis can be found on the data archive server of the Laboratory for Attosecond Physics at the Max Planck Institute of Quantum Optics:  
`/afs/rzg/mpq/lap/publication_archive /theses/2021/Buberl, Theresa (PhD).`

For each figure a separate folder is available with an origin file containing the raw data. Where necessary, explanatory text files and programming code to evaluate or generate the data are included.



# Bibliography

- [1] M. J. Baker, S. R. Hussain, L. Lovergne, V. Untereiner, C. Hughes, R. A. Lukaszewski, G. Thiéfin, and G. D. Sockalingum, “Developing and understanding biofluid vibrational spectroscopy: a critical review,” *Chemical Society reviews*, vol. 45, no. 7, pp. 1803–1818, 2016.
- [2] E. F. Petricoin, A. M. Ardekani, B. A. Hitt, P. J. Levine, V. A. Fusaro, S. M. Steinberg, G. B. Mills, C. Simone, D. A. Fishman, E. C. Kohn, and L. A. Liotta, “Use of proteomic patterns in serum to identify ovarian cancer,” *The Lancet*, vol. 359, no. 9306, pp. 572–577, 2002.
- [3] E. F. Petricoin, D. K. Ornstein, C. P. Paweletz, A. Ardekani, P. S. Hackett, B. A. Hitt, A. Velasco, C. Trucco, L. Wiegand, K. Wood, C. B. Simone, P. J. Levine, W. M. Linehan, M. R. Emmert-Buck, S. M. Steinberg, E. C. Kohn, and L. A. Liotta, “Serum proteomic patterns for detection of prostate cancer,” *Journal of the National Cancer Institute*, vol. 94, no. 20, pp. 1576–1578, 2002.
- [4] J. C. Miller, H. Zhou, J. Kwekel, R. Cavallo, J. Burke, E. B. Butler, B. S. Teh, and B. B. Haab, “Antibody microarray profiling of human prostate cancer sera: antibody screening and identification of potential biomarkers,” *Proteomics*, vol. 3, no. 1, pp. 56–63, 2003.
- [5] E. F. Petricoin, C. Belluco, R. P. Araujo, and L. A. Liotta, “The blood peptidome: a higher dimension of information content for cancer biomarker discovery,” *Nature reviews. Cancer*, vol. 6, no. 12, pp. 961–967, 2006.
- [6] J. M. Chalmers, M. Diem, and P. R. Griffiths, *Vibrational spectroscopy for medical diagnosis*. Hoboken, NJ, USA: John Wiley & Sons, Inc, 2008.
- [7] A. Barth, “Infrared spectroscopy of proteins,” *Biochimica et biophysica acta*, vol. 1767, no. 9, pp. 1073–1101, 2007.
- [8] H. J. Byrne, M. Baranska, G. J. Puppels, N. Stone, B. Wood, K. M. Gough, P. Lasch, P. Heraud, J. Sulé-Suso, and G. D. Sockalingum, “Spectro-pathology for the next generation: quo vadis?,” *The Analyst*, vol. 140, no. 7, pp. 2066–2073, 2015.

- [9] J. Ollesch, S. L. Drees, H. M. Heise, T. Behrens, T. Brüning, and K. Gerwert, “FTIR spectroscopy of biofluids revisited: an automated approach to spectral biomarker identification,” *The Analyst*, vol. 138, no. 14, pp. 4092–4102, 2013.
- [10] K. Gajjar, J. Trevisan, G. Owens, P. J. Keating, N. J. Wood, H. F. Stringfellow, P. L. Martin-Hirsch, and F. L. Martin, “Fourier-transform infrared spectroscopy coupled with a classification machine for the analysis of blood plasma or serum: a novel diagnostic approach for ovarian cancer,” *The Analyst*, vol. 138, no. 14, pp. 3917–3926, 2013.
- [11] J. R. Hands, G. Clemens, R. Stables, K. Ashton, A. Brodbelt, C. Davis, T. P. Dawson, M. D. Jenkinson, R. W. Lea, C. Walker, and M. J. Baker, “Brain tumour differentiation: rapid stratified serum diagnostics via attenuated total reflection Fourier-transform infrared spectroscopy,” *Journal of neuro-oncology*, vol. 127, no. 3, pp. 463–472, 2016.
- [12] H. A. Gebbie and G. A. Vanasse, “Interferometric spectroscopy in the far infra-red,” *Nature*, vol. 178, no. 4530, p. 432, 1956.
- [13] P. R. Griffiths and J. A. de Haseth, *Fourier Transform Infrared Spectrometry*. Hoboken, NJ, USA: John Wiley & Sons, Inc, 2007.
- [14] P. Fellgett, “Spectromètre interférentiel multiplex pour mesures infra-rouges sur les étoiles,” *Journal de Physique et le Radium*, vol. 19, no. 3, pp. 237–240, 1958.
- [15] P. Jacquinot, “The luminosity of spectrometers with prisms, gratings, or Fabry-Perot etalons,” *Journal of the Optical Society of America*, vol. 44, no. 10, p. 761, 1954.
- [16] K. Araki, N. Yagi, Y. Ikemoto, H. Yagi, C.-J. Choong, H. Hayakawa, G. Beck, H. Sumi, H. Fujimura, T. Moriwaki, Y. Nagai, Y. Goto, and H. Mochizuki, “Synchrotron FTIR micro-spectroscopy for structural analysis of Lewy bodies in the brain of Parkinson’s disease patients,” *Scientific reports*, vol. 5, p. 17625, 2015.
- [17] G. S. Edwards, R. H. Austin, F. E. Carroll, M. L. Copeland, M. E. Couprie, W. E. Gabella, R. F. Haglund, B. A. Hooper, M. S. Hutson, E. D. Jansen, K. M. Joos, D. P. Kiehart, I. Lindau, J. Miao, H. S. Pratisto, J. H. Shen, Y. Tokutake, A. F. G. van der Meer, and A. Xie, “Free-electron-laser-based biophysical and biomedical instrumentation,” *Review of Scientific Instruments*, vol. 74, no. 7, pp. 3207–3245, 2003.
- [18] J. Faist, F. Capasso, D. L. Sivco, C. Sirtori, A. L. Hutchinson, and A. Y. Cho, “Quantum cascade laser,” *Science*, vol. 264, no. 5158, pp. 553–556, 1994.
- [19] Y. Yao, A. J. Hoffman, and C. F. Gmachl, “Mid-infrared quantum cascade lasers,” *Nature Photonics*, vol. 6, no. 7, pp. 432–439, 2012.

- [20] J. Haas, E. V. Catalán, P. Piron, M. Karlsson, and B. Mizaikoff, “Infrared spectroscopy based on broadly tunable quantum cascade lasers and polycrystalline diamond waveguides,” *The Analyst*, vol. 143, no. 21, pp. 5112–5119, 2018.
- [21] M. Brandstetter, L. Volgger, A. Genner, C. Jungbauer, and B. Lendl, “Direct determination of glucose, lactate and triglycerides in blood serum by a tunable quantum cascade laser-based mid-IR sensor,” *Applied Physics B*, vol. 110, no. 2, pp. 233–239, 2013.
- [22] A. Schwaighofer, M. Montemurro, S. Freitag, C. Kristament, M. J. Culzoni, and B. Lendl, “Beyond Fourier transform infrared spectroscopy: External cavity quantum cascade laser-based mid-infrared transmission spectroscopy of proteins in the amide I and amide II region,” *Analytical Chemistry*, vol. 90, no. 11, pp. 7072–7079, 2018.
- [23] J. Brons, V. Pervak, E. Fedulova, D. Bauer, D. Sutter, V. Kalashnikov, A. Apolonskiy, O. Pronin, and F. Krausz, “Energy scaling of Kerr-lens mode-locked thin-disk oscillators,” *Optics letters*, vol. 39, no. 22, pp. 6442–6445, 2014.
- [24] I. Pupeza, D. Sánchez, J. Zhang, N. Lilienfein, M. Seidel, N. Karpowicz, T. Paasch-Colberg, I. Znakovskaya, M. Pescher, W. Schweinberger, V. Pervak, E. Fill, O. Pronin, Z. Wei, F. Krausz, A. Apolonski, and J. Biegert, “High-power sub-two-cycle mid-infrared pulses at 100 Mhz repetition rate,” *Nature Photonics*, vol. 9, no. 11, pp. 721–724, 2015.
- [25] F. Stutzki, C. Gaida, M. Gebhardt, F. Jansen, A. Wienke, U. Zeitner, F. Fuchs, C. Jauregui, D. Wandt, D. Kracht, J. Limpert, and A. Tünnermann, “152 W average power Tm-doped fiber CPA system,” *Optics letters*, vol. 39, no. 16, pp. 4671–4674, 2014.
- [26] J. Zhang, F. Schulze, K. F. Mak, V. Pervak, D. Bauer, D. Sutter, and O. Pronin, “High-power, high-efficiency Tm:YAG and Ho:YAG thin-disk lasers,” *Laser & Photonics Reviews*, vol. 12, no. 3, p. 1700273, 2018.
- [27] N. Nagl, S. Gröbmeyer, V. Pervak, F. Krausz, O. Pronin, and K. F. Mak, “Directly diode-pumped, Kerr-lens mode-locked, few-cycle Cr:ZnSe oscillator,” *Optics express*, vol. 27, no. 17, pp. 24445–24454, 2019.
- [28] T. P. Butler, N. Lilienfein, J. Xu, N. Nagl, C. Hofer, D. Gerz, K. F. Mak, C. Gaida, T. Heuermann, M. Gebhardt, J. Limpert, F. Krausz, and I. Pupeza, “Multi-octave spanning, Watt-level ultrafast mid-infrared source,” *Journal of Physics: Photonics*, vol. 1, no. 4, p. 044006, 2019.
- [29] Q. Wu and X.-C. Zhang, “Ultrafast electro-optic field sensors,” *Applied Physics Letters*, vol. 68, no. 12, pp. 1604–1606, 1996.

- [30] J. U. Jepsen, C. Winnewisser, M. Schall, V. Schyja, S. R. Keiding, and H. Helm, “Detection of THz pulses by phase retardation in lithium tantalate,” *Physical review. E, Statistical physics, plasmas, fluids, and related interdisciplinary topics*, vol. 53, no. 4, pp. R3052–R3054, 1996.
- [31] M. Porer, J.-M. Ménard, and R. Huber, “Shot noise reduced terahertz detection via spectrally postfiltered electro-optic sampling,” *Optics letters*, vol. 39, no. 8, pp. 2435–2438, 2014.
- [32] M. Huber, M. Trubetskov, S. A. Hussain, W. Schweinberger, C. Hofer, and I. Pupeza, “Optimum sample thickness for trace analyte detection with field-resolved infrared spectroscopy,” *Analytical Chemistry*, vol. 92, no. 11, pp. 7508–7514, 2020.
- [33] A. Laubereau and W. Kaiser, “Vibrational dynamics of liquids and solids investigated by picosecond light pulses,” *Reviews of Modern Physics*, vol. 50, no. 3, pp. 607–665, 1978.
- [34] M. Huber, W. Schweinberger, M. Trubetskov, S. A. Hussain, O. Pronin, L. Vamos, E. Fill, A. Apolonski, M. Zigman, F. Krausz, and I. Pupeza, “Detection sensitivity of field-resolved spectroscopy in the molecular fingerprint region,” in *2017 Conference on Lasers and Electro-Optics Europe & European Quantum Electronics Conference (CLEO/Europe-EQEC)*, p. 1, IEEE, 25/06/2017 - 29/06/2017.
- [35] I. Pupeza, M. Huber, W. Schweinberger, M. Trubetskov, S. A. Hussain, L. Vamos, O. Pronin, F. Habel, V. Pervak, N. Karpowicz, E. Fill, A. Apolonski, M. Zigman, A. M. Azzeer, and F. Krausz, “Field-resolved spectroscopy in the molecular fingerprint region,” in *2017 Conference on Lasers and Electro-Optics Europe & European Quantum Electronics Conference (CLEO/Europe-EQEC)*, p. 1, IEEE, 25/06/2017 - 29/06/2017.
- [36] I. Pupeza, M. Huber, M. Trubetskov, W. Schweinberger, S. A. Hussain, C. Hofer, K. Fritsch, M. Poetzlberger, L. Vamos, E. Fill, T. Amotchkina, K. V. Kepesidis, A. Apolonski, N. Karpowicz, V. Pervak, O. Pronin, F. Fleischmann, A. Azzeer, M. Žigman, and F. Krausz, “Field-resolved infrared spectroscopy of biological systems,” *Nature*, vol. 577, no. 7788, pp. 52–59, 2020.
- [37] R. W. Boyd, *Nonlinear optics*. London: Academic, 3rd ed., 2008.
- [38] J. A. Armstrong, N. Bloembergen, J. Ducuing, and P. S. Pershan, “Interactions between light waves in a nonlinear dielectric,” *Physical Review*, vol. 127, no. 6, pp. 1918–1939, 1962.
- [39] G. P. Agrawal, *Nonlinear fiber optics*. Amsterdam and London: Elsevier/Academic Press, 4th ed., 2007.

- [40] Q. Wu and X.-C. Zhang, “Free-space electro-optics sampling of mid-infrared pulses,” *Applied Physics Letters*, vol. 71, no. 10, pp. 1285–1286, 1997.
- [41] A. Leitenstorfer, S. Hunsche, J. Shah, M. C. Nuss, and W. H. Knox, “Detectors and sources for ultrabroadband electro-optic sampling: Experiment and theory,” *Applied Physics Letters*, vol. 74, no. 11, pp. 1516–1518, 1999.
- [42] S.-G. Park, M. R. Melloch, and A. M. Weiner, “Comparison of terahertz waveforms measured by electro-optic and photoconductive sampling,” *Applied Physics Letters*, vol. 73, no. 22, pp. 3184–3186, 1998.
- [43] H. J. Bakker, G. C. Cho, H. Kurz, Q. Wu, and X.-C. Zhang, “Distortion of terahertz pulses in electro-optic sampling,” *Journal of the Optical Society of America B*, vol. 15, no. 6, p. 1795, 1998.
- [44] G. Gallot and D. Grischkowsky, “Electro-optic detection of terahertz radiation,” *Journal of the Optical Society of America B*, vol. 16, no. 8, p. 1204, 1999.
- [45] P. Sulzer, K. Oguchi, J. Huster, M. Kizmann, T. L. M. Guedes, A. Liehl, C. Beckh, A. S. Moskalenko, G. Burkard, D. V. Seletskiy, and A. Leitenstorfer, “Determination of the electric field and its hilbert transform in femtosecond electro-optic sampling,” *Physical Review A*, vol. 101, no. 3, 2020.
- [46] C. J. Saraceno, F. Emaury, C. Schriber, M. Hoffmann, M. Golling, T. Südmeyer, and U. Keller, “Ultrafast thin-disk laser with 80  $\mu$ J pulse energy and 242 W of average power,” *Optics letters*, vol. 39, no. 1, pp. 9–12, 2014.
- [47] O. Pronin, J. Brons, C. Grasse, V. Pervak, G. Boehm, M.-C. Amann, V. L. Kalashnikov, A. Apolonski, and F. Krausz, “High-power 200 fs Kerr-lens mode-locked Yb:YAG thin-disk oscillator,” *Optics letters*, vol. 36, no. 24, pp. 4746–4748, 2011.
- [48] L. E. Hargrove, R. L. Fork, and M. A. Pollack, “Locking of He–Ne laser modes induced by synchronous intracavity modulation,” *Applied Physics Letters*, vol. 5, no. 1, pp. 4–5, 1964.
- [49] M. Piché, “Beam reshaping and self-mode-locking in nonlinear laser resonators,” *Optics Communications*, vol. 86, no. 2, pp. 156–160, 1991.
- [50] C. Gaida, M. Gebhardt, T. Heuermann, F. Stutzki, C. Jauregui, J. Antonio-Lopez, A. Schülzgen, R. Amezcua-Correa, A. Tünnermann, I. Pupeza, and J. Limpert, “Watt-scale super-octave mid-infrared intrapulse difference frequency generation,” *Light, science & applications*, vol. 7, p. 94, 2018.
- [51] F. Junginger, A. Sell, O. Schubert, B. Mayer, D. Brida, M. Marangoni, G. Cerullo, A. Leitenstorfer, and R. Huber, “Single-cycle multiterahertz transients with peak fields above 10 MV/cm,” *Optics letters*, vol. 35, no. 15, pp. 2645–2647, 2010.

- [52] C. Gaida, T. Heuermann, M. Gebhardt, E. ShestaeV, T. P. Butler, D. Gerz, N. Lilienfein, P. Sulzer, M. Fischer, R. Holzwarth, A. Leitenstorfer, I. Pupeza, and J. Limpert, “High-power frequency comb at 2  $\mu\text{m}$  wavelength emitted by a Tm-doped fiber laser system,” *Optics letters*, vol. 43, no. 21, pp. 5178–5181, 2018.
- [53] A. Stingl, M. Lenzner, C. Spielmann, F. Krausz, and R. Szipöcs, “Sub-10-fs mirror-dispersion-controlled Ti:sapphire laser,” *Optics letters*, vol. 20, no. 6, pp. 602–604, 1995.
- [54] J. Brons, V. Pervak, D. Bauer, D. Sutter, O. Pronin, and F. Krausz, “Powerful 100-fs-scale Kerr-lens mode-locked thin-disk oscillator,” *Optics letters*, vol. 41, no. 15, pp. 3567–3570, 2016.
- [55] M. Seidel, G. Arisholm, J. Brons, V. Pervak, and O. Pronin, “All solid-state spectral broadening: an average and peak power scalable method for compression of ultrashort pulses,” *Optics express*, vol. 24, no. 9, pp. 9412–9428, 2016.
- [56] J. Schulte, T. Sartorius, J. Weitenberg, A. Vernaleken, and P. Russbuehdt, “Nonlinear pulse compression in a multi-pass cell,” *Optics letters*, vol. 41, no. 19, pp. 4511–4514, 2016.
- [57] M. Hanna, X. Délen, L. Lavenu, F. Guichard, Y. Zaouter, F. Druon, and P. Georges, “Nonlinear temporal compression in multipass cells: theory,” *Journal of the Optical Society of America B*, vol. 34, no. 7, p. 1340, 2017.
- [58] K. Fritsch, M. Poetzlberger, V. Pervak, J. Brons, and O. Pronin, “All-solid-state multipass spectral broadening to sub-20 fs,” *Optics letters*, vol. 43, no. 19, pp. 4643–4646, 2018.
- [59] A. Apolonski, A. Poppe, G. Tempea, C. Spielmann, T. Udem, R. Holzwarth, T. Hänsch, and F. Krausz, “Controlling the phase evolution of few-cycle light pulses,” *Physical review letters*, vol. 85, no. 4, pp. 740–743, 2000.
- [60] A. Schliesser, N. Picqué, and T. W. Hänsch, “Mid-infrared frequency combs,” *Nature Photonics*, vol. 6, no. 7, pp. 440–449, 2012.
- [61] S. A. Hussain, C. Hofer, M. Högner, T. Buberl, W. Schweinberger, D. Gerz, M. Huber, J. Jacob, A. Weigel, N. Karpowicz, F. Krausz, and I. Pupeza, “Sub-attosecond-precision optical-waveform stability measurements using electro-optic sampling,” *in preparation*, 2020.
- [62] H. Fattahi, *Third-generation femtosecond technology*. Springer theses, Cham: Springer Science and Business Media, 2016.
- [63] O. Pronin, M. Seidel, F. Lücking, J. Brons, E. Fedulova, M. Trubetskov, V. Pervak, A. Apolonski, T. Udem, and F. Krausz, “High-power multi-megahertz source of waveform-stabilized few-cycle light,” *Nature communications*, vol. 6, p. 6988, 2015.

- [64] N. R. Newbury, B. R. Washburn, K. L. Corwin, and R. S. Windeler, “Noise amplification during supercontinuum generation in microstructure fiber,” *Optics letters*, vol. 28, no. 11, pp. 944–946, 2003.
- [65] M. Huber, W. Schweinberger, F. Stutzki, J. Limpert, I. Pupeza, and O. Pronin, “Active intensity noise suppression for a broadband mid-infrared laser source,” *Optics express*, vol. 25, no. 19, pp. 22499–22509, 2017.
- [66] N. Tsurumachi, T. Fuji, S. Kawato, T. Hattori, and H. Nakatsuka, “Interferometric observation of femtosecond free induction decay,” *Optics letters*, vol. 19, no. 22, p. 1867, 1994.
- [67] F. Keilmann, C. Gohle, and R. Holzwarth, “Time-domain mid-infrared frequency-comb spectrometer,” *Optics letters*, vol. 29, no. 13, pp. 1542–1544, 2004.
- [68] I. Coddington, W. Swann, and N. Newbury, “Coherent dual-comb spectroscopy at high signal-to-noise ratio,” *Physical Review A*, vol. 82, no. 4, 2010.
- [69] C. Kübler, R. Huber, and A. Leitenstorfer, “Ultrabroadband terahertz pulses: generation and field-resolved detection,” *Semiconductor Science and Technology*, vol. 20, no. 7, pp. S128–S133, 2005.
- [70] D. Molter, M. Trierweiler, F. Ellrich, J. Jonuscheit, and G. von Freymann, “Interferometry-aided terahertz time-domain spectroscopy,” *Optics express*, vol. 25, no. 7, pp. 7547–7558, 2017.
- [71] D. Jahn, S. Lippert, M. Bisi, L. Oberto, J. C. Balzer, and M. Koch, “On the influence of delay line uncertainty in THz time-domain spectroscopy,” *Journal of Infrared, Millimeter, and Terahertz Waves*, vol. 37, no. 6, pp. 605–613, 2016.
- [72] W. Schweinberger, L. Vamos, J. Xu, S. A. Hussain, C. Baune, S. Rode, and I. Pupeza, “Interferometric delay tracking for low-noise Mach-Zehnder-type scanning measurements,” *Optics express*, vol. 27, no. 4, pp. 4789–4798, 2019.
- [73] T. Amotchkina, M. Trubetskov, S. A. Hussain, D. Hahner, D. Gerz, M. Huber, W. Schweinberger, I. Pupeza, F. Krausz, and V. Pervak, “Broadband dispersive Ge/YbF<sub>3</sub> mirrors for mid-infrared spectral range,” *Optics letters*, vol. 44, no. 21, pp. 5210–5213, 2019.
- [74] I. Pupeza, X. Gu, E. Fill, T. Eidam, J. Limpert, A. Tünnermann, F. Krausz, and T. Udem, “Highly sensitive dispersion measurement of a high-power passive optical resonator using spatial-spectral interferometry,” *Optics express*, vol. 18, no. 25, pp. 26184–26195, 2010.
- [75] M. Uiberacker, T. Uphues, M. Schultze, A. J. Verhoef, V. Yakovlev, M. F. Kling, J. Rauschenberger, N. M. Kabachnik, H. Schröder, M. Lezius, K. L. Kompa, H.-G.

- Muller, M. J. J. Vrakking, S. Hendel, U. Kleineberg, U. Heinzmann, M. Drescher, and F. Krausz, "Attosecond real-time observation of electron tunnelling in atoms," *Nature*, vol. 446, no. 7136, pp. 627–632, 2007.
- [76] D. M. Jonas, "Two-dimensional femtosecond spectroscopy," *Annual review of physical chemistry*, vol. 54, pp. 425–463, 2003.
- [77] P. R. Griffiths, B. L. Hirsche, and C. J. Manning, "Ultra-rapid-scanning Fourier transform infrared spectrometry," *Vibrational Spectroscopy*, vol. 19, no. 1, pp. 165–176, 1999.
- [78] B. Süß, F. Ringleb, and J. Heberle, "New ultrarapid-scanning interferometer for FT-IR spectroscopy with microsecond time-resolution," *The Review of scientific instruments*, vol. 87, no. 6, p. 063113, 2016.
- [79] P. Jacob, A. Weigel, D. Gröters, T. Buberl, M. Trubetskov, M. Huber, J. Heberle, and I. Pupeza, "Mid-infrared waveform measurement by rapid mechanical scanning," *EPJ Web of Conferences*, vol. 243, p. 16002, 2020.
- [80] B. Urbanek, M. Möller, M. Eisele, S. Baierl, D. Kaplan, C. Lange, and R. Huber, "Femtosecond terahertz time-domain spectroscopy at 36 kHz scan rate using an acousto-optic delay," *Applied Physics Letters*, vol. 108, no. 12, p. 121101, 2016.
- [81] P. Tournois, "Acousto-optic programmable dispersive filter for adaptive compensation of group delay time dispersion in laser systems," *Optics Communications*, vol. 140, no. 4-6, pp. 245–249, 1997.
- [82] O. Schubert, M. Eisele, V. Crozatier, N. Forget, D. Kaplan, and R. Huber, "Rapid-scan acousto-optical delay line with 34 kHz scan rate and 15 as precision," *Optics letters*, vol. 38, no. 15, pp. 2907–2910, 2013.
- [83] C. Janke, M. Först, M. Nagel, H. Kurz, and A. Bartels, "Asynchronous optical sampling for high-speed characterization of integrated resonant terahertz sensors," *Optics letters*, vol. 30, no. 11, pp. 1405–1407, 2005.
- [84] A. Bartels and T. Dekorsy, "Terahertz-spektroskopie mit high-speed ASOPS (THz spectroscopy based on high-speed ASOPS)," *tm - Technisches Messen*, vol. 75, no. 1, 2008.
- [85] A. Bartels, A. Thoma, C. Janke, T. Dekorsy, A. Dreyhaupt, S. Winnerl, and M. Helm, "High-resolution THz spectrometer with kHz scan rates," *Optics express*, vol. 14, no. 1, pp. 430–437, 2006.
- [86] A. Bartels, R. Cerna, C. Kistner, A. Thoma, F. Hudert, C. Janke, and T. Dekorsy, "Ultrafast time-domain spectroscopy based on high-speed asynchronous optical sampling," *The Review of scientific instruments*, vol. 78, no. 3, p. 035107, 2007.

- [87] F. Tauser, C. Rausch, J. H. Posthumus, and F. Lison, “Electronically controlled optical sampling using 100 Mhz repetition rate fiber lasers,” in *Commercial and Biomedical Applications of Ultrafast Lasers VIII* (J. Neev, S. Nolte, A. Heisterkamp, and C. B. Schaffer, eds.), SPIE Proceedings, p. 68810O, SPIE, 2008.
- [88] R. Gebs, P. Klopp, G. Klatt, T. Dekorsy, U. Griebner, and A. Bartels, “Time-domain terahertz spectroscopy based on asynchronous optical sampling with femtosecond semiconductor disk laser,” *Electronics Letters*, vol. 46, no. 1, p. 75, 2010.
- [89] K. Fritsch, J. Brons, M. Iandulskii, K. F. Mak, Z. Chen, F. Krausz, N. Picque, and O. Pronin, “High-power dual-comb thin-disk oscillator,” in *2019 Conference on Lasers and Electro-Optics Europe & European Quantum Electronics Conference (CLEO/Europe-EQEC)*, p. 1, IEEE, 23/06/2019 - 27/06/2019.
- [90] J. Fellingner, G. Winkler, A. S. Mayer, L. R. Steidle, and O. H. Heckl, “Tunable dual-color operation of yb: fiber laser via mechanical spectral subdivision,” *Optics express*, vol. 27, no. 4, pp. 5478–5486, 2019.
- [91] J. Kim and F. X. Kärtner, “Attosecond-precision ultrafast photonics,” *Laser & Photonics Reviews*, vol. 4, no. 3, pp. 432–456, 2010.
- [92] J. Kim, F. X. Kärtner, and F. Ludwig, “Balanced optical-microwave phase detectors for optoelectronic phase-locked loops,” *Optics letters*, vol. 31, no. 24, pp. 3659–3661, 2006.
- [93] M. Y. Peng, A. Kalaydzhyan, and F. X. Kärtner, “Balanced optical-microwave phase detector for sub-femtosecond optical-RF synchronization,” *Optics express*, vol. 22, no. 22, pp. 27102–27111, 2014.
- [94] S. Gröbmeyer, J. Brons, M. Seidel, and O. Pronin, “Carrier-envelope-offset frequency stable 100 W-level femtosecond thin-disk oscillator,” *Laser & Photonics Reviews*, vol. 13, no. 3, p. 1800256, 2019.
- [95] A. Weigel, T. Buberl, F. Krausz, and I. Pupeza, “Method and apparatus for measuring a time delay between pairs of pulses from laser pulse sequences, and applications thereof,” *PCT Patent No. PCT/EP2020/087657*, 2020.
- [96] Weigel, J. Alexander, G. Philip, B. David, H. Theresa, H. Marinus, T. Joachim, P. Michale, and Ioachim, “Ultra-rapid electro-optic sampling of octave-spanning mid-infrared waveforms,” *submitted*, 2021.
- [97] Syed Ali Hussain, *Field resolving spectrometer for mid-infrared molecular spectroscopy*. Phd thesis, Ludwig Maximilians University Munich, Munich, Germany, 2021.
- [98] D. Brida, G. Krauss, A. Sell, and A. Leitenstorfer, “Ultrabroadband Er: fiber lasers,” *Laser & Photonics Reviews*, vol. 8, no. 3, pp. 409–428, 2014.

- [99] T. Buberl, P. Sulzer, A. Leitenstorfer, F. Krausz, and I. Pupeza, “Broadband interferometric subtraction of optical fields,” *Optics express*, vol. 27, no. 3, pp. 2432–2443, 2019.
- [100] H. Bar-Lev, “A dual-beam infrared interferometer-spectrometer,” *Infrared Physics*, vol. 7, no. 2, pp. 93–98, 1967.
- [101] H. R. Chandrasekhar, L. Genzel, and J. Kuhl, “Double-beam fourier spectroscopy with interferometric background compensation,” *Optics Communications*, vol. 17, no. 1, pp. 106–110, 1976.
- [102] D. Kuehl and P. R. Griffiths, “Dual-beam Fourier transform infrared spectrometer,” *Analytical Chemistry*, vol. 50, no. 3, pp. 418–422, 1978.
- [103] D. L. Beduhn and R. L. White, “Advantages of dual-beam interferometry in Fourier transform infrared spectrometry,” *Applied Spectroscopy*, vol. 40, no. 5, pp. 628–632, 1986.
- [104] R. N. Bracewell, “Detecting nonsolar planets by spinning infrared interferometer,” *Nature*, vol. 274, no. 5673, pp. 780–781, 1978.
- [105] Pavel Gabor, *A study of the performance of a nulling interferometer testbed preparatory to the Darwin mission*. Phd thesis, Université Paris Sud - Paris XI, Paris, France, 2009.
- [106] E. Serabyn and M. M. Colavita, “Fully symmetric nulling beam combiners,” *Applied optics*, vol. 40, no. 10, pp. 1668–1671, 2001.
- [107] Y. Rabbia, J. Gay, and J.-P. Rivet, “The achromatic interfero coronagraph,” *Comptes Rendus Physique*, vol. 8, no. 3-4, pp. 385–395, 2007.
- [108] D. Mawet, C. Hanot, C. Lenaers, P. Riaud, D. Defrère, D. Vandormael, J. Loicq, K. Fleury, J.-Y. Plessier, J. Surdej, and S. Habraken, “Fresnel rhombs as achromatic phase shifters for infrared nulling interferometry,” *Optics express*, vol. 15, no. 20, pp. 12850–12865, 2007.
- [109] J. Hayden, S. Hugger, F. Fuchs, and B. Lendl, “A quantum cascade laser-based Mach–Zehnder interferometer for chemical sensing employing molecular absorption and dispersion,” *Applied Physics B*, vol. 124, no. 2, 2018.
- [110] I. Pupeza, F. Krausz, and T. Buberl, “Interferometry with an achromatic interferometric superposition of electromagnetic fields,” *PCT Patent No. PCT/EP2018/069229*, 2018.
- [111] A. Sommer, E. M. Bothschafter, S. A. Sato, C. Jakubeit, T. Latka, O. Razskazovskaya, H. Fattahi, M. Jobst, W. Schweinberger, V. Shirvanyan, V. S. Yakovlev, R. Kienberger, K. Yabana, N. Karpowicz, M. Schultze, and F. Krausz, “Attosecond

- nonlinear polarization and light-matter energy transfer in solids,” *Nature*, vol. 534, no. 7605, pp. 86–90, 2016.
- [112] H. Kogelnik and T. Li, “Laser beams and resonators,” *Applied optics*, vol. 5, no. 10, pp. 1550–1567, 1966.
- [113] W. B. Joyce and B. C. DeLoach, “Alignment of Gaussian beams,” *Applied optics*, vol. 23, no. 23, pp. 4187–4196, 1984.
- [114] T. W. Hänsch and B. Couillaud, “Laser frequency stabilization by polarization spectroscopy of a reflecting reference cavity,” *Optics Communications*, vol. 35, no. 3, pp. 441–444, 1980.
- [115] I. E. Gordon, L. S. Rothman, C. Hill, R. V. Kochanov, Y. Tan, P. F. Bernath, M. Birk, V. Boudon, A. Campargue, K. V. Chance, B. J. Drouin, J.-M. Flaud, R. R. Gamache, J. T. Hodges, D. Jacquemart, V. I. Perevalov, A. Perrin, K. P. Shine, M.-A. Smith, J. Tennyson, G. C. Toon, H. Tran, V. G. Tyuterev, A. Barbe, A. G. Császár, V. M. Devi, T. Furtenbacher, J. J. Harrison, J.-M. Hartmann, A. Jolly, T. J. Johnson, T. Karman, I. Kleiner, A. A. Kyuberis, J. Loos, O. M. Lyulin, S. T. Massie, S. N. Mikhailenko, N. Moazzen-Ahmadi, H. Müller, O. V. Naumenko, A. V. Nikitin, O. L. Polyansky, M. Rey, M. Rotger, S. W. Sharpe, K. Sung, E. Starikova, S. A. Tashkun, J. V. Auwera, G. Wagner, J. Wilzewski, P. Wcisło, S. Yu, and E. J. Zak, “The HITRAN2016 molecular spectroscopic database,” *Journal of Quantitative Spectroscopy and Radiative Transfer*, vol. 203, pp. 3–69, 2017.
- [116] S. Mukamel, *Principles of nonlinear optical spectroscopy*, vol. 6 of *Oxford series in optical and imaging sciences*. New York and Oxford: Oxford University Press, 1995.
- [117] W. Demtröder, *Laser Spectroscopy*. Berlin, Heidelberg: Springer Berlin Heidelberg, 2003.
- [118] A. Pedone, M. Biczysko, and V. Barone, “Environmental effects in computational spectroscopy: accuracy and interpretation,” *ChemPhysChem*, vol. 11, no. 9, pp. 1812–1832, 2010.
- [119] J. Rothenberg, “Self-induced heterodyne: The interaction of a frequency-swept pulse with a resonant system,” *IEEE Journal of Quantum Electronics*, vol. 22, no. 1, pp. 174–181, 1986.
- [120] S. Zamith, J. Degert, S. Stock, B. de Beauvoir, V. Blanchet, M. Aziz Bouchene, and B. Girard, “Observation of coherent transients in ultrashort chirped excitation of an undamped two-level system,” *Physical review letters*, vol. 87, no. 3, p. 033001, 2001.
- [121] A. Monmayrant, B. Chatel, and B. Girard, “Quantum state measurement using coherent transients,” *Physical review letters*, vol. 96, no. 10, p. 103002, 2006.

- [122] J. E. Rothenberg and D. Grischkowsky, "Subpicosecond transient excitation of atomic vapor and the measurement of optical phase," *Journal of the Optical Society of America B*, vol. 3, no. 10, p. 1235, 1986.

# Acknowledgement

In the end, I would like to thank everyone who contributed to this PhD thesis and supported me during the last four years. First of all, this PhD project would not have been possible without Ferenc, who provided the unique laboratory infrastructure at MPQ and LEX, and the funding, and - above all - holds together such a great team of very smart people.

The next person to mention is Ioachim. His most remarkable characteristic as supervisor was certainly his unbreakable enthusiasm for science and for new ideas. In some moments, this attitude was demanding but mostly it was very motivating and impressive. Also, I have to thank him for his patience and support to always believe in me even when I had lost confidence.

I enjoyed the long and educational discussions with Regina and Martin, our collaborators at the chemistry department, who patiently explained to us quantum chemistry for dummies. Especially, I am grateful to Regina for finding the time to be my secondary referee.

All the members of our closer team deserve a big thank you: My office mate Christina was always there for me to answer my questions, listen to my complains, help out in the lab, and join any kind of social event. Maxi solved programming issues and provided theory expertise. Daniel supported me with his incredible optimism and readiness to help. Wolfgang solved Labview-related problems and together with Ali shared their long-year lab experience on Infrsamplers with me. Marinus, Cristina, and Lucy helped me with sample preparation and handling. And last but not least, Alex and Philip took over my laser system and made great progress towards a rapid scanning Infrsampler.

I also want to thank Kilian for leaving me with such a well-engineered laser frontend, Gaia and Sebastian for discussions and advice on multipass broadening cells, Tatiana and Vladimir for designing and coating MIR optics, and Markus for support with any kind of oscillator issues.

Furthermore, I am grateful to every member of the Krausz group for always having an open ear and a helping hand for me. The personal interaction with all of you inside the institute and during numerous fun activities helped me to overcome disappointments in the lab and enriched my PhD life.

The biggest thank you goes to Stephan, without whom I would never have finished this thesis. I am very grateful for all your support and understanding during the last four years. Finally I want to thank my parents for believing in me, for giving me freedom to choose my way, and for being there for me.